A Numerical Model for Simulating the Dynamic Response of an Inertial Confinement Fusion Cavity Gas to a Target Explosion

Thomas J. McCarville

December 1982

UWFDM-634

Ph.D. thesis.

FUSION TECHNOLOGY INSTITUTE

UNIVERSITY OF WISCONSIN

MADISON WISCONSIN

A Numerical Model for Simulating the Dynamic Response of an Inertial Confinement Fusion Cavity Gas to a Target Explosion

Thomas J. McCarville

Fusion Technology Institute
University of Wisconsin
1500 Engineering Drive
Madison, WI 53706

http://fti.neep.wisc.edu

December 1982

UWFDM-634

Ph.D. thesis.

A NUMERICAL MODEL FOR SIMULATING THE DYNAMIC RESPONSE OF AN INERTIAL CONFINEMENT FUSION CAVITY GAS TO A TARGET EXPLOSION

BY

THOMAS J. MCCARVILLE

A thesis submitted in partial fulfillment of the
requirements for the degree of

DOCTOR OF PHILOSOPHY

(Nuclear Engineering)

at the

UNIVERSITY OF WISCONSIN-MADISON

1982

A NUMERICAL MODEL FOR SIMULATING THE DYNAMIC RESPONSE OF AN INERTIAL CONFINEMENT FUSION CAVITY GAS TO A TARGET EXPLOSION

Thomas J. McCarville

Under the Supervision of Professor Gerald L. Kulcinski

One of the methods suggested for protecting the first wall of an inertial confinement fusion cavity from the x-rays and ions emitted by an exploding target is to fill the cavity with a buffer gas. A computer code package is developed in this thesis for studying the radiative and hydrodynamic response of the gas to an exploding target.

The x-rays emitted by the target are one of the major energy sources that influence the gas response. This work shows that the x-ray deposition can be accurately modeled using the point source model in most instances. The intense x-ray flux ionizes the gas surrounding the target and reduces the photoelectric attenuation coefficient. To account for this reduction a method of computing the photoelectric attenuation coefficient as a function of ionization was developed.

The internal energy and momentum deposited by target ions also influences the gas response. In the model developed here, the energy and momentum deposition rates from target ions are computed using the results of a time independent ion transport code that gives the spatial distribution of ions as a function of energy. Knowing the energy dependence of the spatial distribution, the time dependent

energy and momentum deposition rates are then computed in an approximate fashion.

The x-ray and debris deposition models that were developed in this thesis have been added to the equations solved by the FIRE radiation hydrodynamics code. In addition, the method of computing the radiation temperature used in the two temperature nonequilibrium radiation transport model has been improved. The improved method was inspired by modeling the spectral radiation energy density as a dilute Planckian function.

A number of examples using the FIRE code are presented that illustrate how the response of a cavity gas varies for different gas densities, gas types, target yields, and Lagrangian zoning schemes. One of the surprising observations was that a cooling wave was never observed in the simulations of the cavity gas response. By developing a new analytical analysis of energy transport at a cooling wave front, it was shown why a cooling wave will not occur for yields on the order of those anticipated from ICF targets.

APPROVED:

Date

Gerald L. Kulcinski
Professor, Nuclear Engineering

ACKNOWLEDGMENTS

I would like to express gratitude to my advisor, Dr. Gerald Kulcinski, not only for the positive influence he has had on developing my scientific skills, but also for serving as an example in leadership that is worth emulating. I am also greatly indebted to Dr. Gregory Moses, whose work in radiation hydrodynamics made this thesis possible.

I am grateful to Dr. Robert Peterson for providing some indispensible technical information, as well as for many useful discussions. A special thanks goes to Dr. Thurmon Frank, who helped make the resources of Los Alamos Laboratory available to me, and to Dr. Ihor Bohachevsky, who spent generous amounts of time helping me to understand some difficult concepts. I would also like to thank Dr. Thomas Hunter for his influence during the early stages of this thesis.

A warm thanks goes to my colleague and friend throughout graduate school, Dr. Ahmed Hassanein, who was cooperative in a number of studies. The invaluable assistance of Dennis Bruggink in preparing publications is also greatly appreciated, as well as his supportive friendship. My dependable typist, Beth Brown, is also acknowledged.

The most personally felt thanks go to my fiancé, Marceline, and also to my family, for their enduring faith in my ability to complete this work successfully.

Partial support for this work was provided by Sandia Laboratories, U.S. Department of Energy.

TABLE OF CONTENTS

LIST OF TABLES

LIST OF FIGURES

CHAPTER I

INTRODUCTION

The inertial confinement fusion (ICF) reactor design studies that have been conducted over the last decade have succeeded in identifying many of the technological challenges that must be addressed before a commercial reactor will be feasible. The first wall of a reactor cavity has been of particular interest because an unprotected first wall will be subjected to an intense flux of target x-rays and ions. As a result of the erosion induced by this flux, an unprotected first wall probably cannot be designed to last the lifetime of a commercial power plant and still be acceptable from both an economic and engineering standpoint. To resolve this problem, two options have been explored: either replace the unprotected first wall periodically, or provide a method of protecting it. This study concentrates on the latter option.

A review of the first wall protection concepts that have appeared in the literature is given in Chapter II. This thesis focuses on the gas protection concept, where the energy of the x-rays and ions is attenuated by a cavity gas. The deposited energy produces a thermodynamic state in the gas that is similar to that produced by very high temperature explosions (i.e. nuclear explosions) in standard density air. The radiation hydrodynamic response of standard density air to a high temperature explosion is reviewed in Chapter III. The response of a cavity gas to the energy released by an ICF target will differ from what is described in Chapter III for

several reasons. One reason is that the characteristic dimension of an ICF buffer gas is on the order of meters instead of hundreds of meters. Another reason is that the density and composition of the gas in an ICF reactor will most certainly be unlike that of the atmosphere. Because of these differences, simulating the radiation hydrodynamic response of an ICF buffer gas is a unique and interesting challenge.

The objective of the work presented here is to provide an improved computer model for simulating the response of a buffer gas to the energy released by an ICF target. The FIRE code[1] has been substantially modified during the course of this effort. Chapters IV and V describe in detail the principle improvements that this author has contributed to the code. These modifications include:

- the introduction of a new model for computing the nonequilibrium radiation spectra;
- the introduction of driving terms into the radiation hydrodynamic equations to simulate the interaction of the target debris with the gas;
- the introduction of a new model for computing the deposition of the target x-rays into the gas.

The model for computing the nonequilibrium radiation spectra that is introduced assumes that the frequency spectra of thermal radiation remains Planckian during its transport. With this assumption the frequency dependence can be integrated out of the radiation transport equation and a radiation temperature is defined

in a natural way. The details of this model are presented in Chapter IV.

The model used to compute the attenuation of target x-rays is presented in Chapter V. Exponential attenuation is assumed, and a simple method for computing the reduction in the photoelectric attenuation coefficient due to "electron bleaching" is introduced. Without inclusion of the bleaching effect, the x-ray energy deposition near the target would be over-estimated.

A model for computing the interaction of the target debris with the gas is also presented in Chapter V. To compute this interaction in its full detail, a time dependent ion transport calculation is required. The model developed here saves considerable effort and expense by using some simplifying assumptions and a few input parameters from the output of a relatively inexpensive time independent ion transport code.

Finally, some applications of the FIRE code are presented in Chapter VI. Although some of these calculations have already appeared in publications, others appear here for the first time. A list of the publications eminating from this work is given in Table I-1.

Table I-1. Publications

REFERENCE	DATE	AUTHORS	TITLE
10	November 1978[a]	T.J. McCarville A.M. Hassanein G.L. Kulcinski	The Response of Stainless Steel to the Pellet Debris in a Laser Fusion Reactor (University of Wisconsin Fusion Engineering Report, UWFDM-282)
88	January 1981	T.J. McCarville G.L. Kulcinski G.A. Moses	An Analytical Model for the Motion and Radiative Response of a Low Density Inertial Confinement Fusion Buffer Gas (University of Wisconsin Fusion Engineering Report, UWFDM-405)
89	April 1981	T.J. McCarville G.A. Moses G.L. Kulcinski	A Model for Depositing Inertial Confinement Fusion X-rays and Pellet Debris Into a Cavity Gas (University of Wisconsin Fusion Engineering Report, UWFDM-406)
80	June 1981	T.J. McCarville R.R. Peterson G.A. Moses	Improvements in the FIRE Code for Simulating the Response of a Cavity Gas to Inertial Confinement Fusion Target Explosions (University of Wisconsin Fusion Engineering Report, UWFDM-407)
87	August 1981[b]	A.M. Hassanein T.J. McCarville G.L. Kulcinski	First Wall Evaporation in Inertial Confinement Fusion Reactors Utilizing Gas Protection (University of Wisconsin Fusion Engineering Report, UWFDM-423)

[a]Presented at the 5th International Conference on Structural Mechanics in Reactor Technology, Berlin, August 1979.

[b]Presented at the Second Topical Meeting on Fusion Reactor Materials, Seattle, August 1981.

CHAPTER II

TYPICAL FEATURES OF THE ENVIRONMENT IN AN INERTIAL CONFINEMENT FUSION REACTOR

The physics of inertial confinement fusion is briefly reviewed in Section A of this chapter in order to provide some insight into how the target yield is partitioned among photons, target ions, and neutrons. The response of an unprotected first wall to the radiation emitted by the target is then described in Section B, where it is shown that an unprotected first wall will erode by a variety of mechanisms. Finally, a concise review of the first wall protection schemes that have appeared in the literature is given in Section C.

A. The Target Spectra

Although target physics is still in an early stage of research and development, some general characteristics of the radiation emitted by the target can be identified from the current state of the art. Figure II-1 shows a series of targets designed to be driven by laser beams. The surface of the outer shell ablates outward as the laser energy is absorbed, carrying with it about half of the deposited energy.[2] In reaction to the ablation process, a shock wave converges on the fuel and creates the conditions necessary for a sustained fusion reaction. It was found during the course of experiments with CO_2 and neodymium glass lasers that energetic electrons from the plasma layer stream through the fuel and heat it before the shock arrives. This preheating is undesirable because a stronger shock is required to compress the fuel along a higher adiabat. One

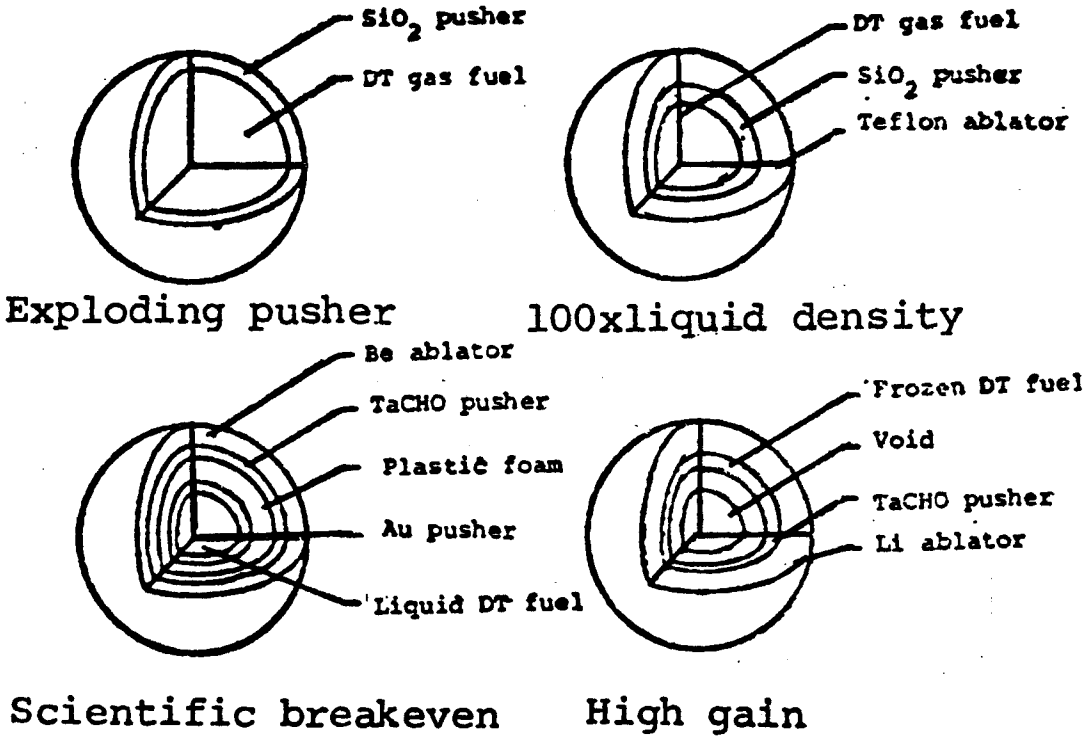

Figure II-1. Examples of laser driven targets (Ref. 5).

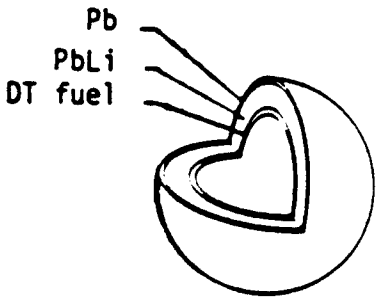

Figure II-2. An example of a high gain ion driven target (Ref. 6).

function of the pusher layer is to attenuate these energetic electrons. The pusher can also be designed to improve the implosion, efficiency, and reduces the need to tailor the beam power.(3)

At the present time, the commercial applications of laser driven fusion are a long way from being economically feasible. This is partly because the efficiency of the lasers within current technology is only a few percent, and partly because 20% or more of the beam on target is reflected from the plasma surface by Brilloin scattering. These conditions dictate target gains ranging from 200 to 1000 for commercial feasibility, which puts demands on target design technology that have not yet been met.

The difficulties in designing laser driven targets have prompted an interest in driving targets with ion beams. Figure II-2 is a schematic of a high gain, ion driven target. The ions pass through the lead tamper and deposit their energy in the lead-lithium pusher. With the aid of the tamper's inertia, the pusher then compresses the fuel to ignition conditions. One of the advantages of using an ion driver is that hot electrons are not generated during beam deposition. Another advantage is that nearly 100% of the beam energy is absorbed by the target. But the main advantage of using ion driven targets for commercial applications of inertial confinement fusion is that the efficiency of ion accelerators appears to be much higher than that obtainable by lasers. The efficiency of a light ion or a heavy ion accelerator is typically between twenty and twenty-five percent.

The principles governing ignition and burn propagation in the fuel are independent of the type of driver used. The driver deposits energy into the target on a time scale much shorter than the hydrodynamic relief time, so a shock wave with a pressure gradient on the order of 10 TPa (10^8 atm.) is launched toward the fuel. The fuel is compressed to a thousand times solid density at the center of shock convergence, where a Lawson number (fuel density x confinement time) of about 10^{14} s/cm^3 must be attained before the burn can begin. As the hydrodynamic energy of the shock is converted to internal energy at the point of convergence, temperatures on the order of 10^8 °K are reached and ignition begins. In a successful burn, ignition conditions then propagate outward as alpha particles and thermal radiation heat the surrounding fuel. The radius of the compressed fuel times the density (ρr) should be between 1 to 5 gm/cm^2 to sustain the burn propagation. The burn lasts about 10^{-10} seconds, and terminates as increasing pressure expands the fuel.

Without interactions between the fusion reaction products and the pellet structure, 20% of the fusion energy from each deuterium-tritium reaction would be in a 3.5 MeV alpha particles and 80% in 14.1 MeV neutrons. However, the alphas collisionally transfer energy to lower temperature particles, so the spectra of each ion species emitted from the target has a distribution of energies. The neutron spectra also has a distribution of energies because the mean free path of 14 MeV neutrons in a target with ρr between 1 and 5 gm/cm^2 is on the order of the target radius.[4] The x-ray spectra consists of

a high energy component (≈ 100 keV) emitted from the fuel during the burn, and lower energy x-rays emitted from the shells surrounding the fuel. Table II-1 lists some nominal characteristics of the radiation emitted by the target.

Table II-1. Nominal Characteristics of ICF Targets

	Laser Driven	Ion Driven
Minimum Desirable Gain for Driver Efficiency x Gain = 20	200-1000	80-100
Reflected Beam Energy (% of Driver Energy)	10-20	---
Ablated Ions (% of Driver Energy)	50	50
X-rays (% of Yield)	1	2-25
Neutrons (% of Yield)	75-80	70
Ions (% of Yield)	20-25	5-28

B. The Response of An Unprotected Surface to the Target Spectra

B.1. The Transient Thermal Response

Studies of the response of an unprotected first wall to the pulsed radiation emitted by the target abound in the literature.[7-10] One of the computer models developed during the course of these studies is the T*DAMEN code,[11] which computes the thermal response from laser light, x-ray, and ion deposition. The method used by T*DAMEN to solve for the temperature is unique in that

Green's function techniques and some approximate expressions for the energy deposition functions allow the temperature equation to be solved semi-analytically. Figures II-3 and II-4 show the thermal response of a stainless steel first wall computed using T*DAMEN. The radiation spectra used is listed in Figure II-3. The heating rate from neutrons was neglected in these calculations because it is less than a few degrees Celcius. The code neglects to take into account the phase change that occurs at about 1430°C. The erosion rate from evaporation and sputtering was estimated at a few microns per shot for this spectra.

Hassanein[12] has shown that there are some subtleties in using Green's functions that were overlooked in developing T*DAMEN. A finite difference code has since been written for first wall analysis that incorporates temperature dependent thermal properties, phase changes, and a moving surface boundary condition.[13] The versatility that can be gained by using finite difference methods instead of Green's function methods is often worth the increase in cost.

Behrisch[14] conducted an interesting study that shows when it is appropriate to use a surface deposition approximation rather than a volumetric deposition function for computing the temperature. The difference in temperature was found to depend on the penetration depth of the source, δ, and the duration of the pulse, τ. If the first wall is a metal that can be modeled as a conductive, free electron plasma, then the penetration depth of low energy photons ($\approx$ 1 eV) is related to the wavelength, λ, by[15]

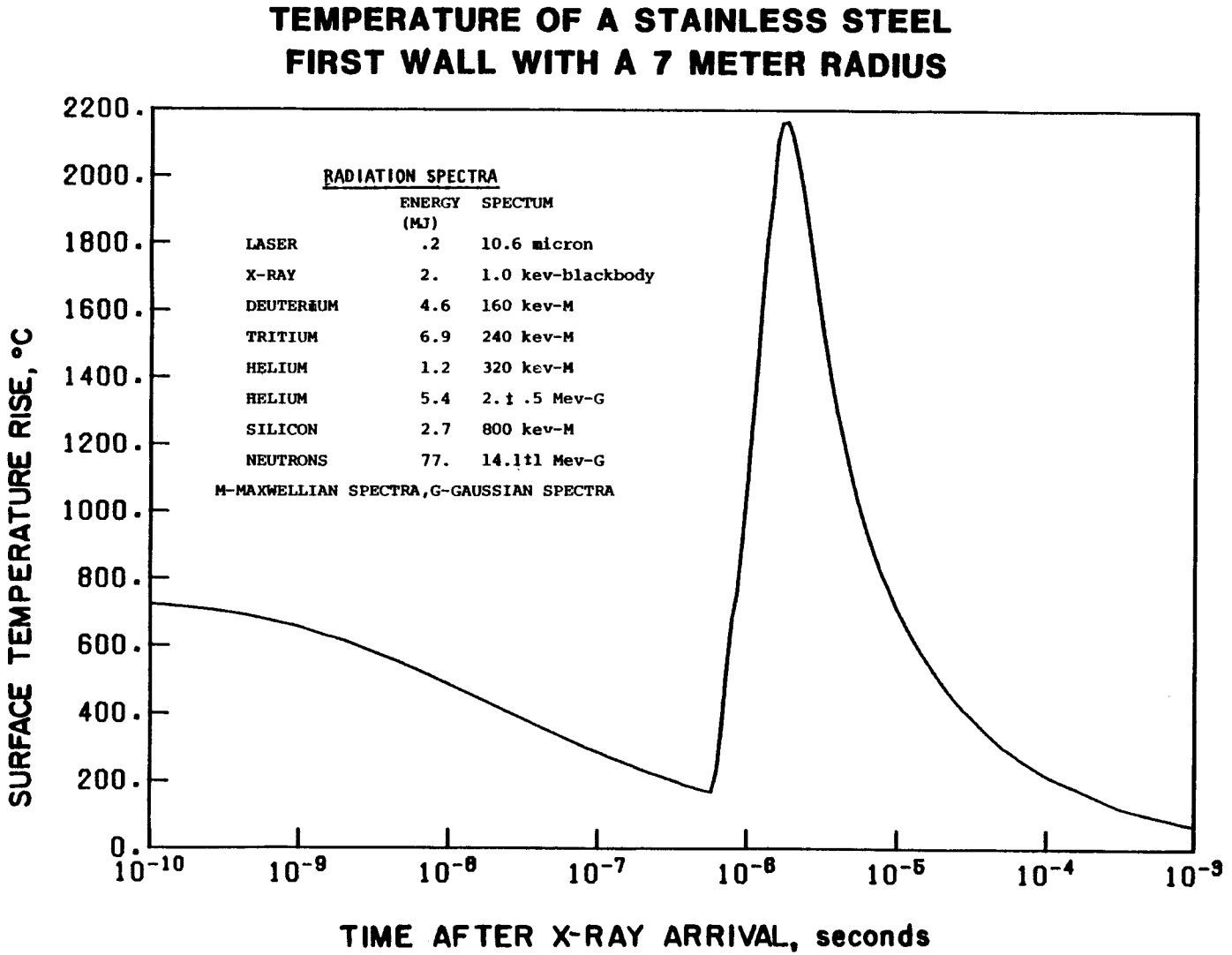

Figure II-3. The surface temperature as a function of time for the example spectra (Ref. 10).

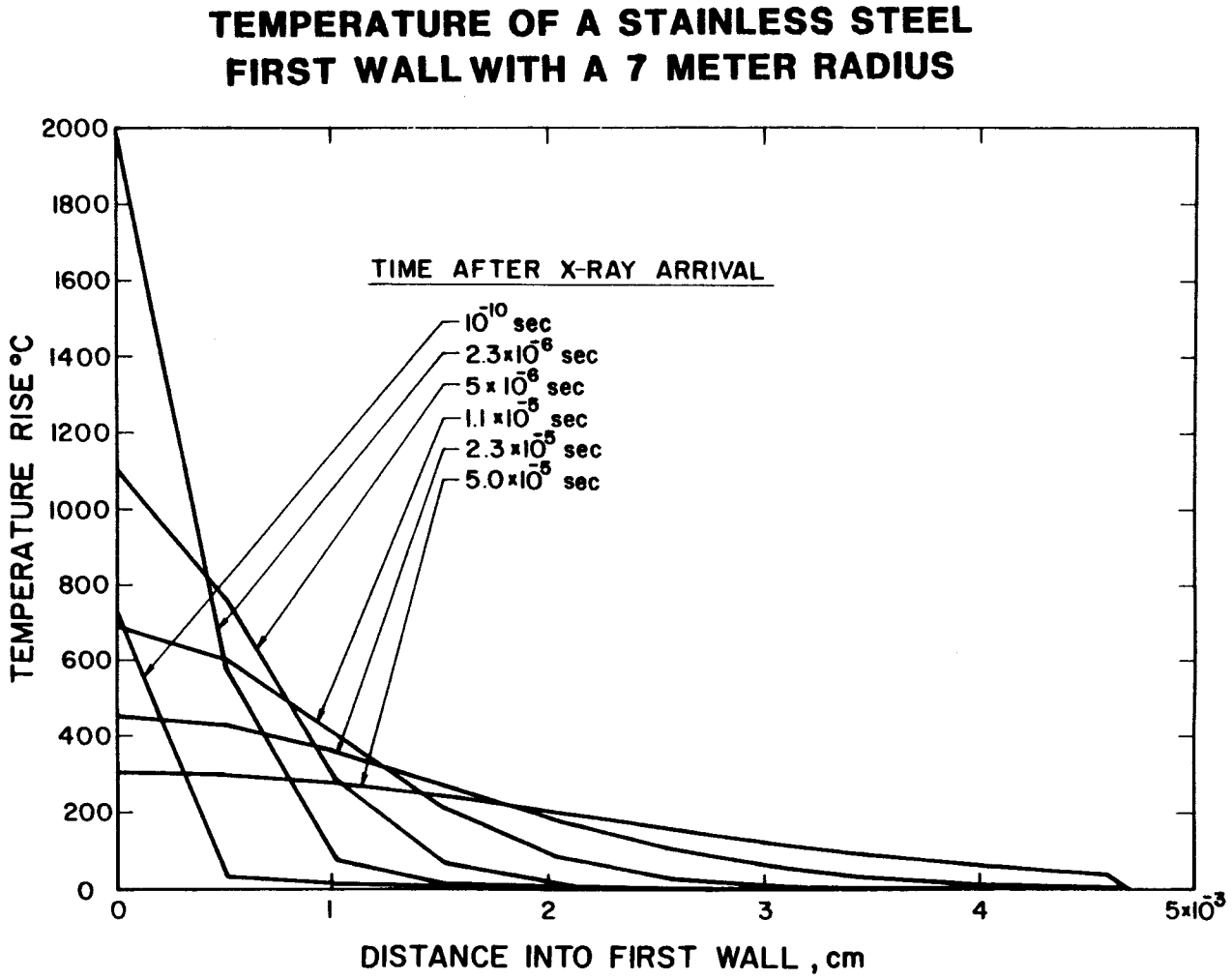

Figure II-4. The surface temperature as a function of space for the example spectra (Ref. 10).

$$\delta = \frac{\lambda}{8\pi} \quad . \tag{1}$$

The difference in the surface temperature computed using each deposition model is shown in Figure II-5 for a value of δ equal to 0.25 μm. The difference begins to become significant for a pulse width shorter than about 10^{-5} seconds. The pulse width from reflected laser light is shorter than this, so a volumetric deposition profile should be used to compute the thermal response. (These findings are also of interest when choosing a deposition model to compute the temperature rise of the wall from thermal radiation emitted by a gas-filled cavity.)

B.2. Impulse Stress and Evaporative Recoil

As the pellet debris decelerates in the first wall, the transferred momentum will manifest itself as a pressure normal to the surface. The rate of momentum transfer is given by particle slowing down models, and the pressure imparted to a surface can be expressed as

$$p_m = \frac{N_o}{S} \frac{dE}{dx} \quad , \tag{2}$$

where: p_m is the pressure from momentum transfer,

N_o is the number of debris particles,

S is the surface area,

$\frac{dE}{dx}$ is the energy change per unit distance per pellet particle.

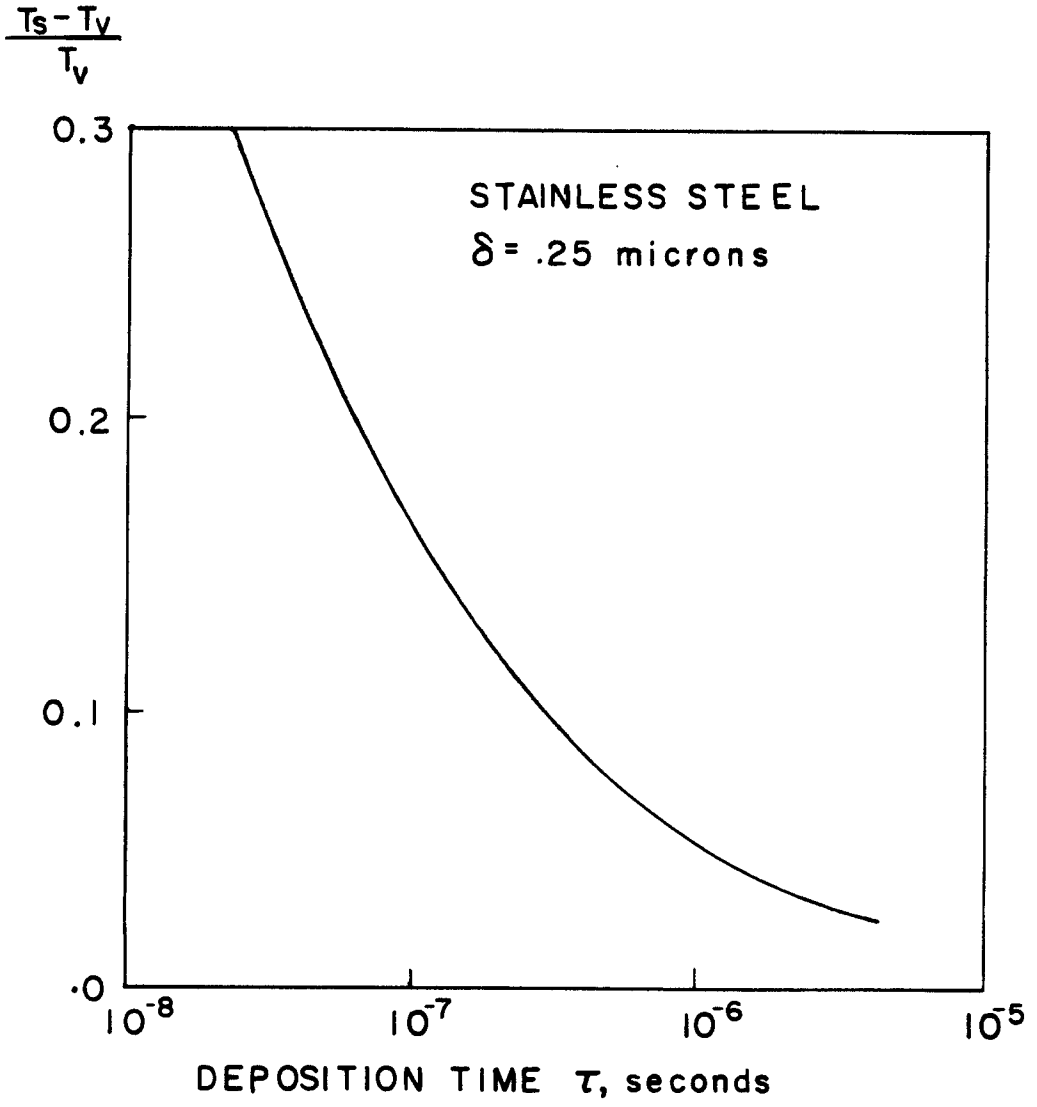

Figure II-5. The fractional difference in the surface temperature of stainless steel when computed using a surface deposition function (T_S) and a volumetric deposition function (T_V).

For a complex spectra of debris particles, the total pressure is the sum of the contributions from each debris species.

The impulse pressure from the debris spectra listed in Figure II-3 is shown in Figure II-6. The dip in the pressure is due to a time lapse between the arrival of fast alpha particles and the other debris. The resulting hoop stress is given by

$$\sigma_h = \frac{p_m R}{\Delta R} \quad , \tag{3}$$

where R is the cavity radius and ΔR is the first wall thickness. One can show that the hoop stress from the impulse pressure is not more than a few ksi if ΔR is on the order of centimeters.

An additional contribution to the surface pressure occurs from evaporative recoil. The pressure from evaporative recoil can be estimated from

$$p_e = \dot{m} v \quad , \tag{4}$$

where $\dot{m}$ is the evaporated mass flux and v is the speed that the evaporated mass leaves the surface. A reasonable estimate of v is the speed of a perfect gas expanding into a vacuum.[16]

$$v = \sqrt{\frac{2\gamma}{1+\gamma} \frac{R}{A} T} \quad , \tag{5}$$

where: γ is the ratio of specific heats, C_p/C_v,

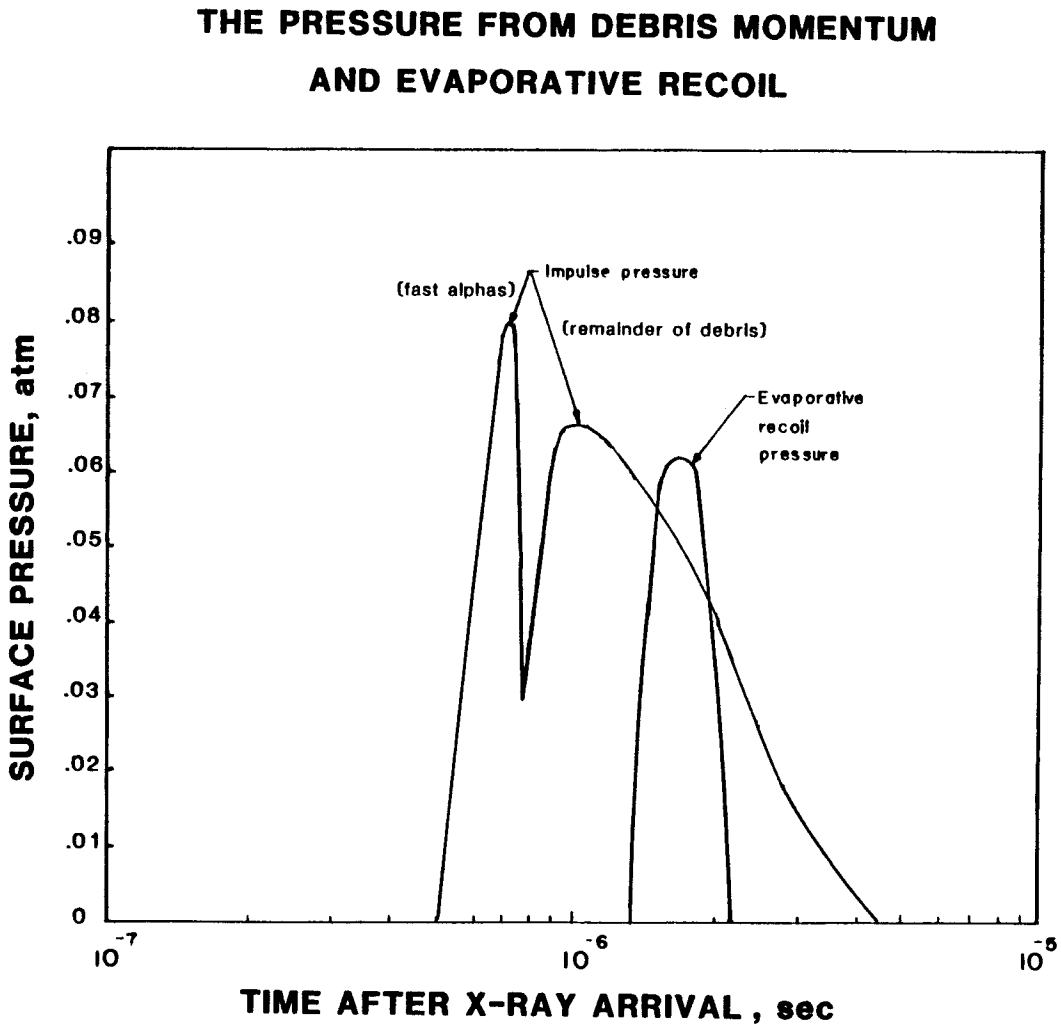

Figure II-6. Impulse and evaporative recoil pressure from the spectra in Figure III-3.

R is the universal gas constant,

A is the atomic mass of the wall material,

T is the surface temperature.

The pressure from evaporative recoil is shown in Figure II-6 for the spectra listed in Figure II-3.

B.3. The Thermoelastic Response

The three characteristic times that are of interest when considering the thermal and elastic response of the first wall to a pellet spectra are: the thermal conduction time τ_t, the mechanical response time τ_m, and the energy deposition time τ. The mechanical response time and the thermal conduction time are related to the deposition depth of each component of the spectra, δ, by

$$\tau_m = \frac{\delta}{c} \tag{6}$$

and

$$\tau_t = \frac{\delta^2}{\alpha} \tag{7}$$

respectively, where α is the thermal diffusivity of the material and c is the sound speed. Hovingh[7] has examined the thermoelastic response of a carbon first wall to each component of the radiation emitted by a laser driven target. Table II-2 shows the characteristic times, the energy fluence, and the thermoelastic response from each energy source.

The deposition time of the neutrons, laser light, and x-rays listed in Table II-2 is much smaller than the conduction times, so

Table II-2. First Wall Energy Deposition and Response for 10 MJ Incident on a First Wall With a 3.5 Meter Radius (Ref. 7)

SOURCE	τ ** seconds	τ_m seconds	τ_t seconds	FLUENCE kJ/cm^2	DEPOSITION kJ/cm^3	SURFACE TEMPERATURE RISE °C	PEAK TENSILE STRESS* MPa
REFLECTED LASER LIGHT	2×10^{-9}	10^{-11}	10^{-11}	1.0	64.3	2900	>100
X-RAYS	$<10^{-9}$	10^{-9}-10^{-8}	10^{-7}-10^{-5}	0.65	0.013	2.0	0.2
14 Mev NEUTRONS	10^{-7}	10^{-4}-10^{-3}	10^{3} -10^{5}	50.0	2×10^{-4}	.26	$<10^{-4}$
HIGH ENERGY ALPHAS	10^{-6}	10^{-9}-10^{-8}	10^{-7}-10^{-5}	4.5	0.09	200.	<0.1
OTHER PELLET DEBRIS	1.2×10^{-6}	10^{-9}-10^{-8}	10^{-7}-10^{-5}	12.	10.6	950.	<0.1

*1MPa = 7600 torr = 920 psi

** Some values in Hovingh's paper are corrected by the author to reflect current knowledge.

the temperature rise can be approximated as

$$\Delta T \simeq \frac{\alpha q'''(x)}{K} \quad , \tag{8}$$

where ΔT is the temperature rise at position x, q''' is the volumetric energy deposition at x, and K is the thermal conductivity. Fourier's law must be used to compute the temperature rise from the high energy alphas and other target debris, because $\tau_t \approx \tau$ for these components.

The mechanical response to the x-rays, neutrons, and target debris is much faster than the thermal conduction time, so a quasi-static model can be used to compute the elastic thermal stress:

$$\sigma_t = - \frac{\psi E \Delta T}{(1 - \nu)} \quad , \tag{9}$$

where: σ_t is the thermal stress,

ψ is the thermal expansion coefficient,

E is the elastic modulus,

ν is Poisson's ratio.

The neutrons deposit their energy in a large enough volume that their contribution to the thermal stress can be ignored. However, the target debris deposit their energy in a layer that is a few to tens of microns thick, and the stress in this layer is well above the elastic limit. Upon cooling, residual tensile stress may encourage crack growth in the region of plastic deformation. Whether these

cracks continue to grow into the load carrying volume or are arrested in the region of plastic deformation is a question yet to be resolved. The synergism between thermal creep, fatigue, crack growth, and radiation effects should be studied in a comprehensive lifetime analysis.

The material with the highest figure of merit for thermal stress, f, should be used if it is necessary to minimize thermal stress. The figure of merit is defined as[17]

$$F \equiv \frac{\sigma_y K(1 - \nu)}{E\psi \sqrt{\alpha}} \quad , \tag{10}$$

where σ_y is the yield stress. Table II-3 lists the figure of merit for some materials.

The thermal response time to reflected laser light is on the same order of magnitude as the mechanical response time, so the expression for a static stress is inappropriate for this component of the spectra. The equation for the time dependent elastic stress normal to the surface is

$$\frac{\partial^2 \sigma}{\partial x^2} - \frac{1}{c^2} \frac{\partial^2 \sigma}{\partial t^2} = \frac{3\alpha K}{c^2} \frac{\partial^2 T}{\partial t^2} \quad . \tag{11}$$

Both Hovingh[7] and Hunter[19] have found that reflected laser light can launch a shock into the first wall, and concluded that the tensile stress that follows the shock is capable of producing surface spallation.

Table II.3. Figure of Merit for Some Construction Materials (Ref. 18)

Material	f	Preference
SiC	18.7	1
Graphite	18.2	2
Zircaloy	14.2	3
Stainless Steel	0.6	4

C. A Review of First Wall Protection Designs

The various first wall protection designs that have appeared in the literature are reviewed below. Each design can be classified as a dry wall, liquid wall, or gaseous protection concept. Table II-4 lists some characteristics of each concept.

C.1. Dry Wall Designs

The dry wall concept consists of an easily replaceable, solid liner that protects the permanent first wall from target x-rays and debris. The two designs that have been considered are a roll of movable carbon cloth[20] and mounted ceramic or metal plates.[21] Both designs are applicable to reactors driven by laser or ion beams.

The dry wall concept is suitable for cavities with a very low gas density, where it is possible to directly convert the energy of the debris ions to electricity. An analysis of direct conversion in an ICF cavity has shown that MHD conversion may be more suitable than

Table II-4. Characteristics of First Wall Protection Concepts

CONCEPT	POSSIBLE MATERIALS	APPLICABLE DRIVERS	RADIATION AFFECTED	FINAL OPTICS PROTECTION	OBSERVATIONS
DRY WALL	• GRAPHITE PLATES • GRAPHITE CLOTH • CERAMIC PLATES, (BeO,SiC) • METALS, (Nb)	LASER * HEAVY IONS * LIGHT IONS	PHOTONS IONS	FROM IONS IF MAGNETIC FIELDS ARE USED	PROS •LOW CAVITY PUMPING •TOLERABLE IMPACT AND EVAPORATIVE RECOIL STRESS •LESS DEVELOPMENT REQUIRED CONS •LARGER CAVITY TO SUPPRESS EROSION •EXTERNAL BLANKET REQUIRED
LIQUID WALLS					
THIN WALL	Li,PbLi	LASER HEAVY IONS	PHOTONS IONS	---	PROS •NO SURFACE HEAT FLUX OR EROSION OF SOLID WALL CONS •FLOW LIMITED REPETITION RATE •LARGE CAVITY TO SUPPRESS ABLATION STRESS •EXTERNAL BLANKET REQUIRED •DEBRIS EXTRACTION DEVELOPMENT REQUIRED
THICK WALL	Li,PbLi	LASER HEAVY IONS	PHOTONS IONS NEUTRONS	---	PROS •MINIMAL RADIATION DAMAGE TO SOLID WALL •NO EXTERNAL BLANKET REQUIRED •NO SURFACE HEAT FLUX OR EROSION CONS •MODERATE OVERPRESSURES DURING FALL DISASSEMBLY •FLOW LIMITED REPETITION RATE •DEBRIS EXTRACTION REQUIRED
GAS	NOBLE GASES POSSIBLY OTHERS	LASER LIGHT IONS	PHOTONS IONS	PHOTONS IONS	PROS •NO DEBRIS IMPACT AT SOLID WALL •REDUCES SURFACE HEAT FLUX TO SOLID WALL •OPTICAL PROTECTION CONS •MODERATE OVERPRESSURES(LIB ONLY) •EXTERNAL BLANKET REQUIRED •DEBRIS EXTRACTION REQUIRED •PELLET HEATING

*MAY NOT BE APPLICABLE IF MAGNETIC FIELDS ARE USED

the use of electrodes,[22] but the efficacy of using any type of direct conversion remains to be shown.

Magnetic guidance of the debris to either heat sinks or direct conversion units has also been considered in conjunction with the dry wall concept.[23] The main advantage of magnetic guidance is that the replacement time of the sacrificial components will be increased. The disadvantages are that the blanket modules are less accessible, and that liquid metal coolants will require more pumping power to overcome the magnetic fields.

C.2. Liquid Wall Designs

The first liquid wall protection scheme was the Blascon design.[24] The idea was to produce a swirling, bubble filled flow of lithium with a stable vortex through the center. The target would be injected down the vortex, where it is ignited by a laser beam as it reached the center. The entire target spectra would be absorbed in the thick layer of lithium, except what traversed along the axis of the vortex. A shock wave is transmitted through the lithium as a result of the energy deposition, and the purpose of bubble injection is to reduce the shock strength.[25] Despite the bubble injection, the stress induced in the cavity structure by the shock would still be formidable.

A porous, paraboloidal structure covered with a thin layer of liquid lithium was proposed in an attempt to satisfy the need to irradiate the target uniformly.[26] Multiple beams of laser light reflecting off the lithium surface were to arrive at the focal point

of the paraboloid simultaneously with the pellet. The non-neutronic components of the pellet spectra would evaporate the lithium layer, so it must be replaced after each shot by extrusion through the structure. The efficacy of this design remains to be shown, in particular the ability of the lithium layer to serve as a laser mirror.

The notion of extruding a thin lithium layer through a porous, spherical first wall was applied by Booth et al.[27] in an early conceptual reactor design, and was later chosen as the first wall protection scheme for a Westinghouse laser fusion study.[28] A spherical first wall enables the target to be irradiated uniformly by passing the beams through holes in the cavity. Booth et al. showed that hundreds of grams of lithium evaporate per shot, and the accompanying ablation can produce pressures on the first wall up to 100 atmospheres. Fatigue failure was estimated to occur after just 100 to 1000 days of operation, even if radiation effects are neglected. It has been suggested that lithium ablation can be suppressed by increasing the surface area,[29] but questions concerning the complete wetability of a porous structure have yet to be answered.

The use of a thick, cylindrical, free falling curtain of liquid lithium (or PbLi alloy) that is detached from the first wall eradicates the need for a porous structure. However, deposition of the pellet energy into the curtain produces pressure waves that launch high velocity, spalled projectiles and slugs of slower fluid toward the wall.[30] The erosion and impact fatigue that result can limit

the first wall lifetime. In the HYLIFE[31] design of a laser fusion reactor it was suggested that these problems could be circumvented by subdividing the curtain into many columnar falls, which has the same effect as the bubbles in the Blascon design. The increased entropy of the design reduces preferential flow because momentum becomes disorganized among the jets. One of the disadvantages of the HYLIFE design is that it is difficult to control the temperature rise of the coolant because it is only subjected to one target explosion. As a result, some control over the thermodynamic efficiency of the plant is lost.

In the HIBALL[6] design of a heavy ion driven reactor it was suggested that the coolant flow could be more closely controlled by directing the jets through tubes of porous silicon carbide fabric. The temperature rise of the coolant can then be optimized while still maintaining the other advantages of the HYLIFE design. The porosity of the weave enables the SiC surfaces facing the target to be wetted enough that the x-rays and ions are attenuated in a thin layer of coolant rather than the tube material. The porosity also allows the coolant to extrude through the tubes after it is shock-heated by neutrons, which reduces the hoop stress on the tube. Despite the attractiveness of the HIBALL first wall protection design, uncertainties about the fatigue lifetime of woven SiC tubes and the compatibility of SiC with the coolant have yet to be resolved.

C.3. Gaseous Protection

A gas in the cavity of an ICF reactor will help to protect the first wall from target x-rays and debris. The gas acts as a thermal capacitor by storing the energy it absorbs and radiating it to the first wall at a slower rate than it would otherwise reach the wall. The degree of protection is dependent upon the density and the atomic weight of the gas, which in turn is dependent upon the driver beam propagation requirements. At present, it seems the gas density should be less than about 3.5×10^{12} atoms/cm^3 for targets driven by heavy ion beams.[32] A gas at this density will allow the debris and x-rays to reach the wall virtually unimpeded, so the gas protection concept does not apply when heavy ion beam drivers are used. Laser beams may be transmittable through gas densities as high as 3.5×10^{16} atoms/cm^3 without significant defocusing,[5] which is high enough to attenuate the target debris but not all of the x-rays. The density of a cavity gas used to assist in the propagation of light ions may be between 1.7×10^{17} atoms/cm^3 to 1.7×10^{18} atoms/cm^3,[33] which is high enough to absorb virtually all of the non-neutronic energy emitted by the target.

The SOLASE[34] and SOLASE-H[18] laser fusion reactor designs utilized the gas protection concept. A six meter cavity filled with 1 torr (0°C) of xenon gas was examined in the SOLASE-H study. Estimates of the heat flux radiated by the gas indicated that the temperature of the first wall would be low enough to avoid evaporation, and the pressure from hydrodynamic motion of the gas could easily be

tolerated. It was concluded that under these conditions the zircaloy first wall of the SOLASE-H reactor would last the lifetime of the plant.

There are many questions concerning the radiation hydrodynamic response of the gas that went unanswered in the SOLASE and SOLASE-H studies. Since those studies three important improvements have been made in the methods used at the University of Wisconsin to analyze the gas. The improved areas are:

- the equations of state and opacity data of the gas,
- the method of computing the transport of nonequilibrium radiation in the gas,
- the models for computing the x-ray and debris deposition in the gas.

The first of these improvements is due to the work of Peterson,[35] who has written a code for computing the opacities and equations of state that is more economical than comparable codes. The second and third improvements are the result of this author's efforts, and are the subject of the following chapters.

CHAPTER III

THE RADIATION HYDRODYNAMIC RESPONSE OF A GAS TO A HIGH TEMPERATURE EXPLOSION

One of the features that distinguishes a nuclear explosion from a chemical explosion is that a nuclear explosion heats the surrounding medium to higher temperatures. The influence of radiation transport is more prominent at higher temperatures, so the response to a nuclear explosion can be quite dependent upon the optical properties of the medium. The response of standard density air to a nuclear explosion is discussed in great detail in the literature, and a brief review of that work is presented in Section A of this chapter. The review provides some necessary background for understanding how an ICF cavity gas will respond to a target explosion.

The theory of blast waves can be useful in ICF reactor design if the fusion energy is strongly coupled to hydrodynamic motion of the gas. The literature on blast waves is briefly reviewed in Section B. However, the theory of blast waves does not apply if the gas density is low enough to decouple the fusion energy from hydrodynamic motion. An analysis that is applicable to explosions in a low density gas is presented in Section C.

A. The Response of Standard Density Air to a High Temperature Explosion

Standard density air responds to the energy released by a nuclear explosion in the four stages shown in Figure III-1.[36-38] The radiation emitted from the device is absorbed in the surrounding

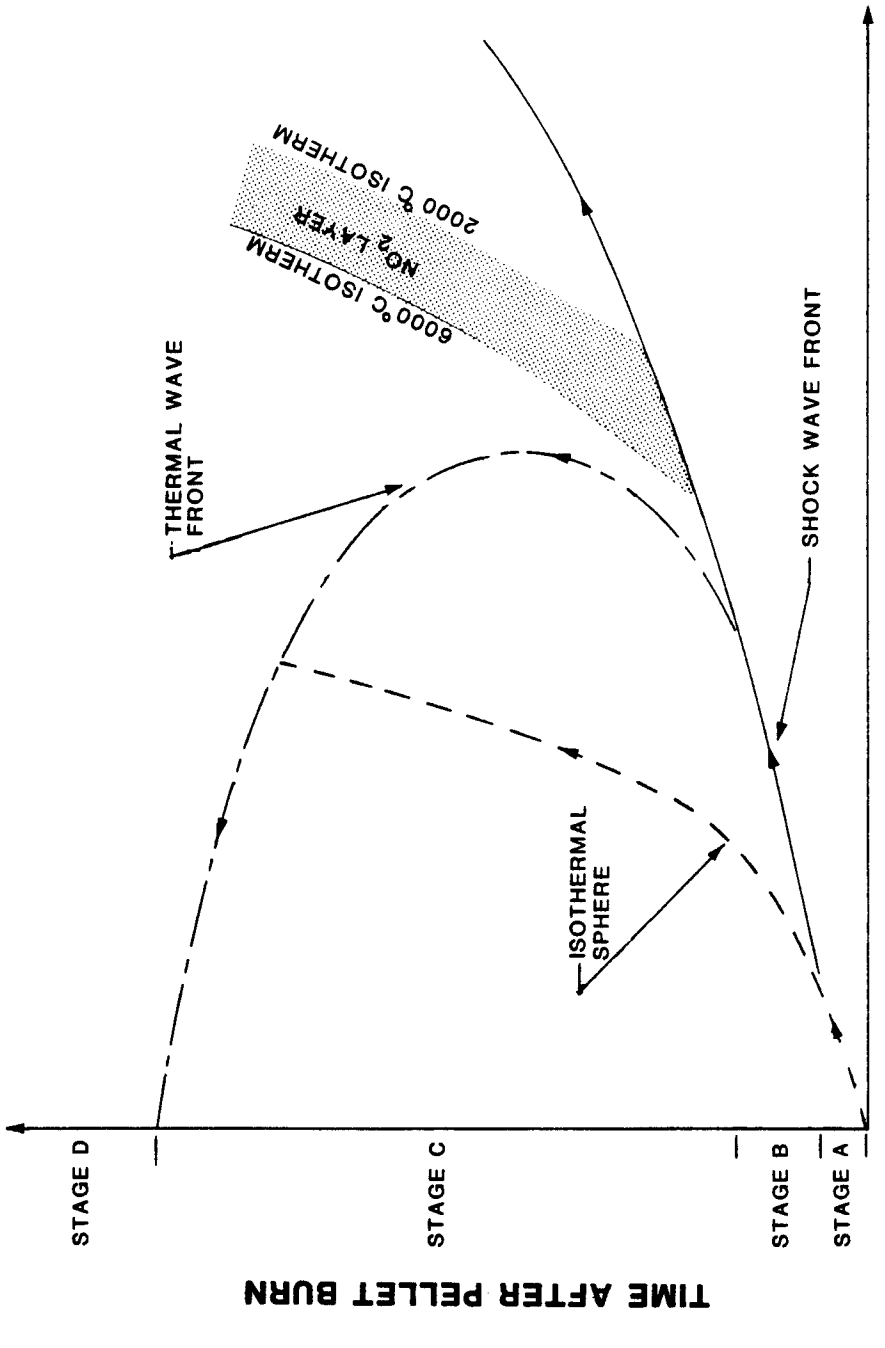

Figure III-1. The four stages of the response of standard density air to a nuclear explosion.

air and heats it to temperatures that can exceed tens of electron volts. The air becomes highly ionized and radiates a high intensity, Planckian spectrum of radiation. At these temperatures the radiating plasma is transparent to its own radiation because of a lack of bound electrons with binding energies suitable for photoabsorption. But the radiation is strongly absorbed in the surrounding cooler air. A thermal wave propagates outward as emission and reabsorption continues in this way. The air heated to these temperatures is referred to as an isothermal sphere because gradients in temperature are quickly relaxed.

The propagation speed of the isothermal sphere eventually becomes less than the sound speed as it continues to engulf more air mass. A shock wave can then form at the thermal wave front as the energy released becomes coupled to the hydrodynamic motion of the gas. Stage B begins when the shock is launched ahead of the isothermal sphere. The shock is strong enough to heat the ambient air to temperatures between a few to tens of electron volts. These temperatures are high enough for the shock heated air to radiate at a moderately high intensity, so the thermal wave front and the shock front are coincident during stage B. The shock heated gas is opaque during stage B, because at these temperatures the bound electrons have the right binding energies for a strong photoabsorption interaction. The only radiation that can propagate ahead of the shock is emitted within a thin layer extending a few mean free paths into the

shock. As a result, only about 1% of the yield is radiated ahead of the shock during stage B.

The radiation emission rate decreases rapidly below a cut off temperature of about one electron volt. Stage C begins when the thermal wave falls behind the shock front because the shock is too weak to heat the ambient air above the cut off temperature. Because of thermal expansion, the thermal wave front continues to propagate outward for awhile after stage C has begun. But then the thermal wave front is observed to reverse its direction and propagate inward. After it reverses directions it is referred to as a cooling wave.[38-40] The reversal in direction can be understood by examining the temperature profile during stage C simultaneously with the radiation mean free path, as shown in Figure III-2. The radiation mean free path of the air enclosed by the cooling wave is short, so the emitted radiation is all reabsorbed except within the layer a few mean free paths thick at the boundary of the opaque region. Some of the energy emitted in this layer escapes into the cooler, transparent air. The energy that escapes from this layer is not replenished by energy from deeper within the opaque region because radiation diffusion is a slow energy transport mechanism when the volume of the opaque region is this large compared to the mean free path. As a result, a cooling wave propagates inward and cools the opaque gas to transparency.

When the cooling wave reaches the center and all of the air has been cooled below the radiation cut off temperature, stage D begins.

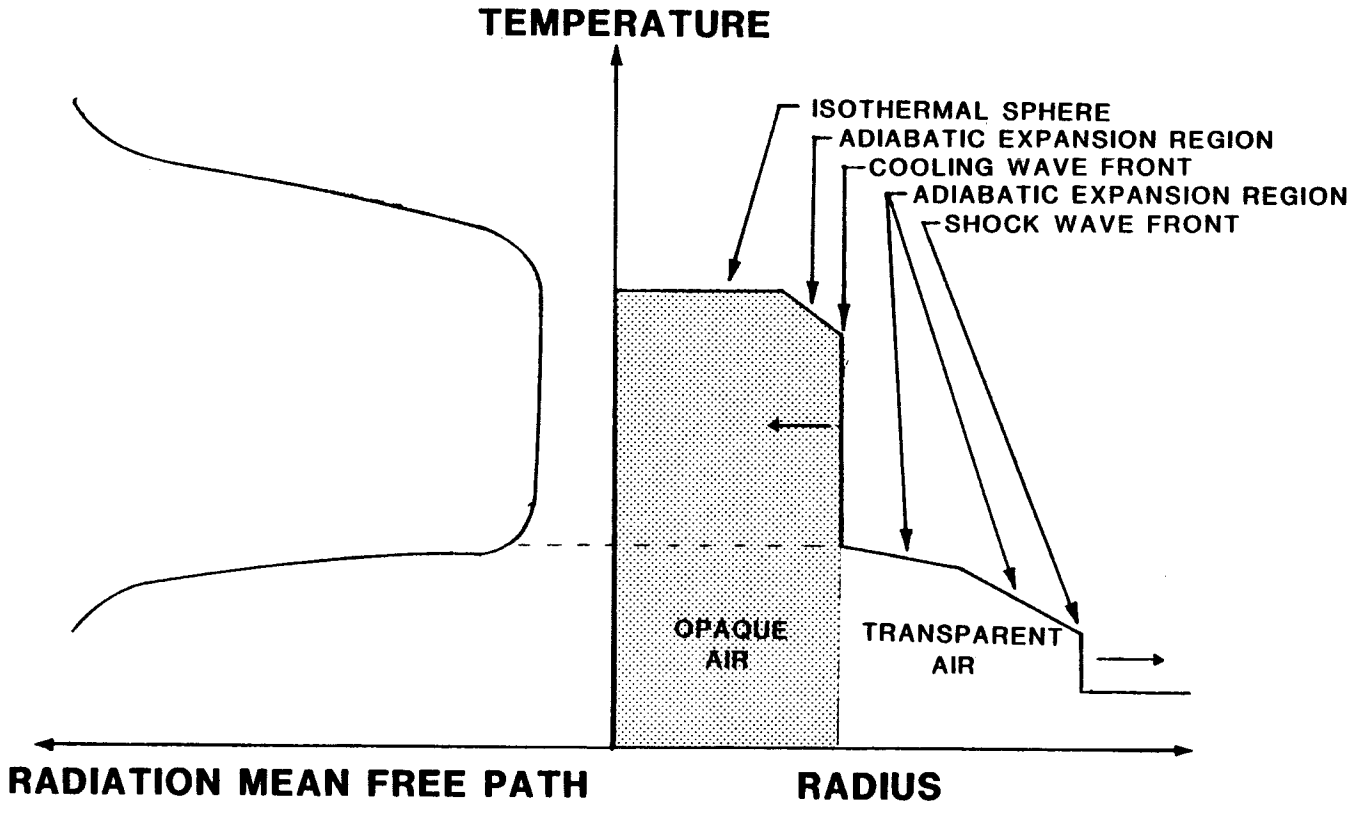

Figure III-2. The temperature profile during stage C of the response of standard density air to a nuclear explosion.

During stage D the air cools mostly by convection as buoyancy forces push the air upward.

A description of what a distant observer will see during a nuclear explosion in standard density air is given in the review by Glasstone,[36] and explanations for the observed phenomena are given by Raizer.[41] The emission rate of light from the thermal front is at a maximum during stage B. The ultraviolet component of the Planckian spectra emitted from the thermal front is strongly absorbed in the ambient temperature air ahead of the shock. But the ambient air is transparent to the visible component, so an observer sees a bright ball of fire. The light intensity that reaches an observer drops sharply soon after the thermal wave falls behind the shock. The reason for the sharp drop in intensity is that a layer of NO_2 forms between the air bounded by the 2000°C and 6000°C isotherm, as shown in Figure III-1. The NO_2 layer absorbs the visible light emitted from the thermal wave front, so the light that reaches a distant observer is radiated from the air at 2000°C. The NO_2 layer decomposes before the cooling wave reaches the center. The light intensity seen by a distant observer increases again as the NO_2 layer decomposes and the thermal wave front becomes visible again.

B. The Hydrodynamics of Blast Waves

The analysis of strong shocks has been of interest since the mid-1940's, when it became desirable to predict the effects of blast waves from nuclear explosions. A strong shock is characterized by a sudden pressure rise an order of magnitude or more above the ambient

pressure. The solution to the hydrodynamics equations can be shown to be self-similar for a strong shock in a perfect, thermally and radiatively nonconducting gas with constant specific heats. Self-similarity means the functions that describe the thermodynamic variables retain their shape, although not their magnitude, with time. This enables the three partial differential equations of hydrodynamics to be condensed into a single, ordinary differential equation for a variable that is a unitless combination of the space and time variables. The solution of this equation provides the position of the shock as a function of time. The thermodynamic variables can then be solved for from a set of ordinary differential equations that are simpler in form than the original equations of hydrodynamics.

Taylor used similarity methods to numerically solve the hydrodynamic equations for a strong blast wave,[42] and solutions for cylindrical and planar shocks[43] have since followed. A compilation of some of the results of these efforts is reproduced in Table III-1. Sedov[45] later used similarity methods to analytically solve the hydrodynamic equations for all three goemetries. Some of Sedov's results are reproduced in Figure III-3 to illustrate the behavior of the thermodynamic variables.

The assumption of constant specific heats is not valid for shocks that ionize or disassociate the propagation medium. This can be seen by writing the ratio of specific heats as

Table III-1. Shock Wave Equations Based on Self-Similar Solutions (Ref. 44)

	SPHERICAL		CYLINDRICAL		PLANE	
	MONATOMIC	DIATOMIC	MONATOMIC	DIATOMIC	MONATOMIC	DIATOMIC
γ	$\frac{5}{3}$	$\frac{7}{5}$	$\frac{5}{3}$	$\frac{7}{5}$	$\frac{5}{3}$	$\frac{7}{5}$
B	3.08	5.33	2.26	3.94	.678	1.22
t	$\frac{2}{5}\left(\frac{E}{B\rho_o}\right)^{-\frac{1}{2}} R^{\frac{5}{2}}$		$\frac{1}{2}\left(\frac{E}{B\rho_o}\right)^{-\frac{1}{2}} R^{2}$		$\frac{2}{3}\left(\frac{E}{B\rho_o}\right)^{-\frac{1}{2}} R^{\frac{3}{2}}$	
U	$\left(\frac{E}{B\rho_o}\right)^{\frac{1}{2}} R^{-\frac{3}{2}}$		$\left(\frac{E}{B\rho_o}\right)^{\frac{1}{2}} R^{-1}$		$\left(\frac{E}{B\rho_o}\right)^{\frac{1}{2}} R^{-\frac{1}{2}}$	
u_1	$\frac{3}{4}U$	$\frac{5}{6}U$	$\frac{3}{4}U$	$\frac{5}{6}U$	$\frac{3}{4}U$	$\frac{5}{6}U$
P_1	$\frac{5}{4} R^{-3} \frac{E}{\gamma B}$	$\frac{7}{6} R^{-3} \frac{E}{\gamma B}$	$\frac{5}{4} R^{-2} \frac{E}{\gamma B}$	$\frac{7}{6} R^{-2} \frac{E}{\gamma B}$	$\frac{5}{4} R^{-1} \frac{E}{\gamma B}$	$\frac{7}{6} R^{-1} \frac{E}{\gamma B}$
T_1	$\frac{1}{4}\frac{P_1 T_o}{P_o}$	$\frac{1}{6}\frac{P_1 T_o}{P_o}$	$\frac{1}{4}\frac{P_1 T_o}{P_o}$	$\frac{1}{6}\frac{P_1 T_o}{P_o}$	$\frac{1}{4}\frac{P_1 T_o}{P_o}$	$\frac{1}{6}\frac{P_1 T_o}{P_o}$

The energy released is E, the shock position is R, t is the time, u is the velocity of individual particles, U is the shock speed, P is the pressure, and T is the temperature. The subscript "o" denotes ambient conditions, and "1" denotes conditions at the shock front.

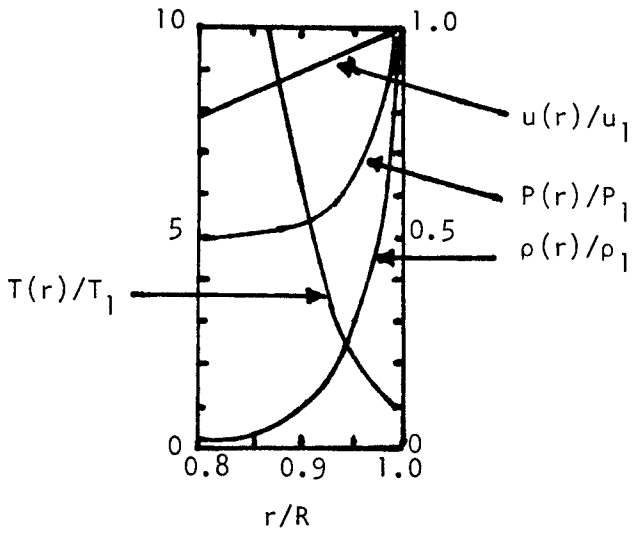

Figure III-3. Pressure, density, velocity, and temperature distribution for a point explosion with $\gamma = 1.23$ (Ref. 45).

$$\gamma = 1 + \frac{P}{\rho e} \quad , \tag{12}$$

where e is the specific internal energy. Equation (12) shows that γ approaches unity as the internal energy increases from ionization and disassociation. The values listed in Table III-1 are only appropriate if the translational component of the internal energy is dominant. However, γ is a slowly varying function, and the similarity solutions are still very accurate if the proper value of γ is used.

The value of the constant, B, also differs from that listed in Table III-1 when ionization and disassociation decrease the value of γ. Fortunately, an approximate expression for B as a function of γ

can be derived. Chernyi[46] derived such an expression by assuming all of the gas swept over by the shock is concentrated in a thin layer at the shock front. That this is a reasonable assumption for a strong shock can be seen by examining Figure III-3. Chernyi's expression is

$$B = G \frac{(3\gamma - 1)}{(\gamma - 1)(\gamma + 1)^2} , \qquad (13)$$

where: $G = \frac{4\pi}{3}$ for spherical geometry,

$= 4\pi$ for cylindrical geometry,

$= 1$ for planar geometry.

There have been attempts to adapt the theory of strong blast waves to circumstances more general than those for which it was developed. For instance, Freiwald and Axeford[47] attempted to provide an analysis for explosions in low density gases by modifying shock theory to include the source mass. But as discussed in the next section of this chapter, the effects of radiation transport cannot be neglected for a low density gas, so their theory has few practical applications.

A more useful extension of shock wave theory was offered by Jones.[48] Jones combined theory with experiment to produce an expression for the pressure increase from a shock of any strength. The expression is

$$P_1 = P_o \frac{2\gamma}{\gamma + 1} \left(\frac{2}{\delta + 2}\right)^2 \frac{1}{c\left[(1 + hx^{\delta})^{(2\delta-1)/2\delta^2} - 1\right]} + P_o , \qquad (14)$$

where $x \equiv R\left[\left(\frac{\delta + 2}{2}\right)^2 \frac{E}{B\gamma P_o}\right]^{-1/\delta}$,

and $c = 0.611$ $h = 5.89$ $\delta = 3$ for spherical geometry,

$c = 0.555$ $h = 4.80$ $\delta = 2$ for cylindrical geometry,

$c = 0.500$ $h = 4.00$ $\delta = 1$ for planar geometry.

Equation (14) extends the ability for predicting the pressure rise at a shock front to distances two orders of magnitude beyond that of strong shock theory.

The pressure exterted on an obstacle during shock reflection is greater than the pressure rise at the shock front. The Hugoniot equations, which describe how the thermodynamic variables change across a shock front, can be used to derive an expression for the pressure exerted by a reflecting shock. Figure III-4 shows how two colliding shocks of equal strength can be used to model a shock reflecting from a wall, and Figure III-5 illustrates the pressure-velocity Hugoniot during shock reflection. The pressure during shock reflection can be shown to be

$$P_w = P_1 \frac{(3\gamma - 1)P_1 - (\gamma - 1)P_o}{(\gamma - 1)P_1 + (\gamma + 1)P_o} \quad , \tag{15}$$

where the subscript "w" denotes conditions at the wall. Equation (15) is valid for shocks of any strength. It is misprinted in some of the standard reference texts,[90] so to insure its correctness a derivation is provided in Appendix A.

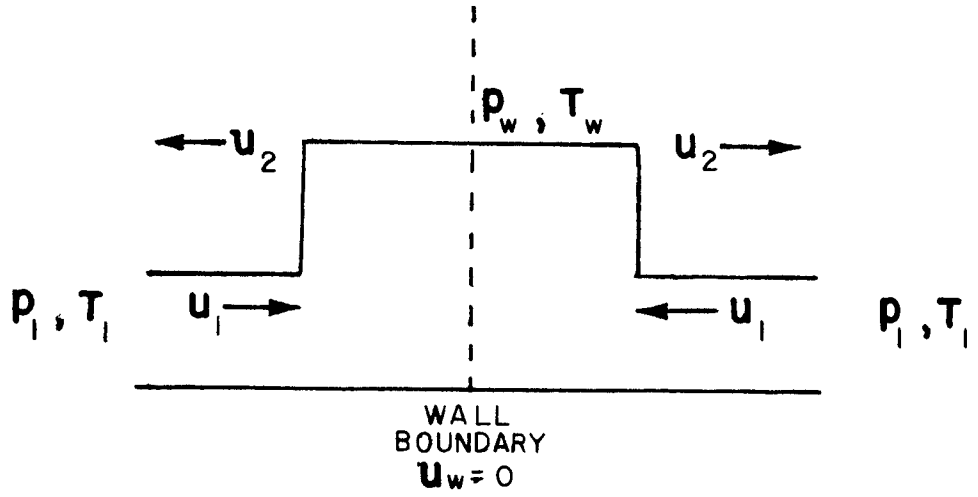

Figure III-4. Pressure and temperature profile of a shock reflecting off a wall boundary.

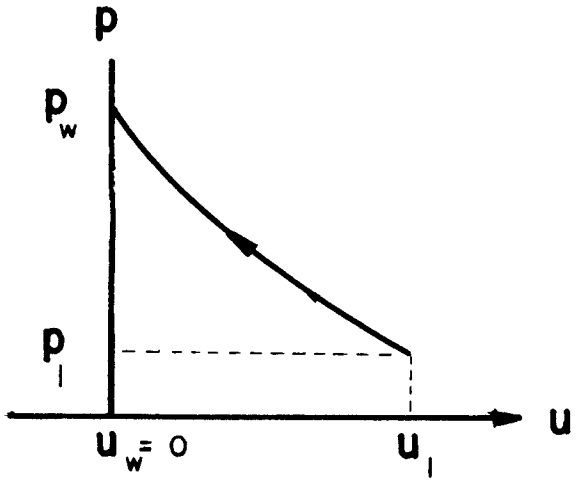

Figure III-5. Pressure-velocity Hugoniot curve at a wall boundary.

C. The Radiation Hydrodynamics of a Debris Driven Shock

C.1. The Hydrodynamic Motion of a Debris Driven Shock

If the density of an ICF cavity gas is low enough that the gas mass is comparable to the target mass, then the gas response is sensitive to how the target debris deposits its energy in the gas. The target debris can act as a spherically expanding piston that drives a shock wave through the gas, or it can simply stream through the gas without inducing hydrodynamic motion. The partitioning of the debris energy into kinetic and internal energy of the gas is analyzed by considering conservation of energy and momentum;

$$\frac{1}{2} m_d u_{do}^2 = \frac{1}{2} m_d u_d^2 + \Delta KE_g + \Delta INT_g \quad , \tag{16}$$

$$m_d u_{do} = m_d u_d + m_g u_g \quad , \tag{17}$$

where: ΔKE_g is the kinetic energy imparted to the gas,

ΔINT_g is the internal energy imparted to the gas,

m_d is the mass of the debris,

m_g is the mass of gas accelerated by the debris,

u_{do} is the initial speed of the debris,

u_d is the instantaneous speed of the debris,

u_g is the speed of the gas accelerated by the debris.

Equations (16) and (17) can be combined to write

$$\frac{\Delta INT_g}{\Delta KE_g} = \frac{m_g (u_{do}^2 - u_d^2)}{m_d (u_{do} - u_d)^2} - 1 \quad . \tag{18}$$

This ratio will have a value near zero if there is a debris driven shock, and values around one or greater if the debris streams through the gas. The mass of gas through which the debris will traverse, m_d, can be computed from the final range of the pellet ions in the gas, r^*. At the end of range, $u_d = 0$, and Equation (18) can be written as

$$\frac{\Delta INT_g}{\Delta KE_g} = \frac{4\pi\rho_o r^{*3}}{3m_d} - 1 \quad . \tag{19}$$

Thus the pellet mass, gas density, and projected range of the debris can be used to predict whether or not a debris driven shock will occur. The value of the range, r^*, used in Equation (19) should be that of a projectile slowing down in a stationary gas. If the ratio on the right-hand side of Equation (19) is much less than unity or negative (negative values imply outward radial deformation of the gas has extended the range beyond the value chosen), then a debris driven shock can be expected.

Figure III-6 is an illustration of a debris driven shock. The position of the shock, R, will be expressed as a function of time. This is done by first assuming that the debris does not penetrate very far into the compressed gas, so the speed of the compressed gas layer, u_g, is nearly equal to that of the debris. Hence,

$$u_g = u_d = \dot{r} \quad , \tag{20}$$

where $\dot{r}$ is the speed of the debris-compressed gas interface. The

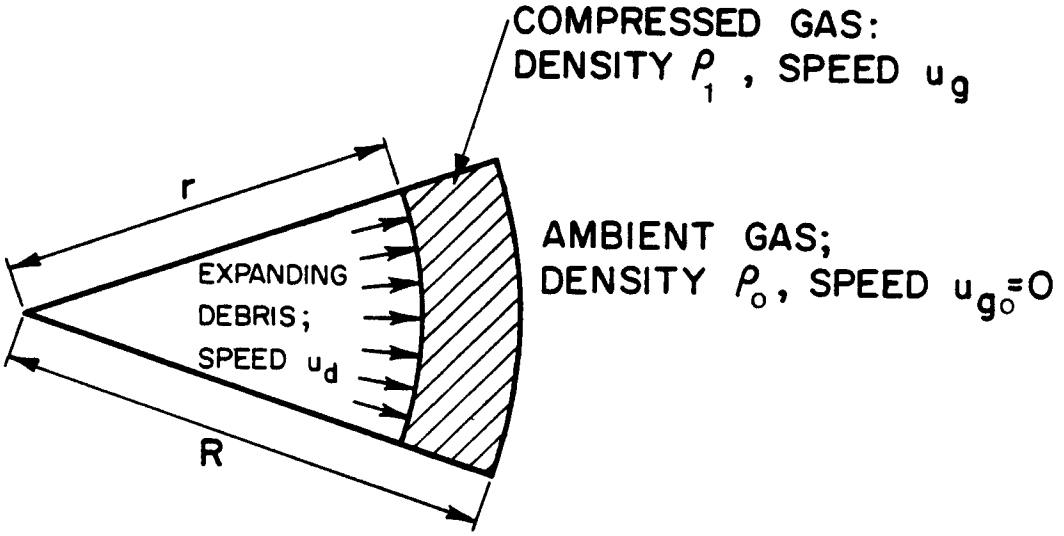

Figure III-6. A cross section of the ambient gas, compressed gas, and expanding debris.

shock at R is strong as long as the shock speed, $\dot{R}$, is much greater than the sound speed. The Hugoniot equation for a strong shock in a perfect gas with constant specific heats relates the gas densities across the shock;

$$\frac{\rho_1}{\rho_o} = \frac{\gamma + 1}{\gamma - 1} \quad . \tag{21}$$

Writing conservation of mass flux across the shock as

$$\rho_o \dot{R} = \rho_1 (\dot{R} - \dot{r}) \quad , \tag{22}$$

and combining this with Equation (21), the speed of the debris-compressed gas interface can be related to the shock speed by

$$\dot{r} = \frac{2}{\gamma + 1} \dot{R} \quad . \tag{23}$$

The relation between the mass of the compressed gas zone, m_g, and the shock position will also be required;

$$m_g = \frac{4}{3} \pi R^3 \rho_o \quad . \tag{24}$$

Combining Equations (17), (20), (23), and (24), an expression for the shock speed as a function of its position is found;

$$\frac{2}{\gamma + 1} \dot{R} [m_d + \frac{4}{3} \pi R^3 \rho_o] = m_d u_{do} \quad . \tag{25}$$

The position of the debris driven shock can then be expressed as a function of time by integrating Equation (25), which gives

$$\frac{2}{\gamma + 1} \frac{R}{u_{do}} [1 + \frac{\pi}{3} R^3 \frac{\rho_o}{m_d}] = t \quad . \tag{26}$$

As the debris sweeps out an increasing mass of gas, the pressure increase across the shock front eventually becomes less than a factor of ten, and Equation (21) will become invalid. As a result, Equation (25) incorrectly predicts that $\dot{R}$ will become less than the speed of sound when the shock is of weak or intermediate strength. The equations derived here should only be used when the debris driven shock is strong.

C.2. The Radiation Emitted from a Debris Driven Shock

An expression for the heat flux emitted from a debris driven shock, $\dot{q}$, can be derived by conserving energy in the volume element shown in Figure III-7. The element is fixed to the shock front. The rate of change of the shock speed is small compared to the acceleration of the gas atoms passing through the shock, so the element is in a quasi-steady state. Conservation of energy requires that

$$\dot{q} = (e_o + \frac{P_o}{\rho_o} + \frac{1}{2}\dot{R}^2)\rho_o\dot{R} - (e_1 + \frac{P_1}{\rho_1} + \frac{1}{2}(\dot{R} - \dot{r})^2)\rho_1(\dot{R} - \dot{r}). \qquad (27)$$

Equations (21) and (23) can be used to rewrite Equation (27) as

$$\dot{q} = [\frac{2}{(\gamma + 1)^2}\dot{R}^2 + e_o + \frac{P_o}{\rho_o} - e_1 - \frac{P_1}{\rho_1}]\rho_o\dot{R} \quad . \qquad (28)$$

If the energy radiated ahead of the shock is very small, then Equation (28) relates the enthalpy jump at the shock to the shock speed. Figure III-8(a) illustrates the temperature profile for this case. The shock is said to be subcritical. The blast wave theory described in Section B of this chapter is applicable to a subcritical shock. If, on the other hand, some energy is radiated ahead of the shock, then the temperature profile may acquire the characteristics of a critical shock. Just enough energy is radiated ahead of a critical shock to equalize the temperatures on both sides of the shock. If the shock is supercritical, as illustrated in Figure III-8(c), then radiation transport drives a thermal wave ahead of the

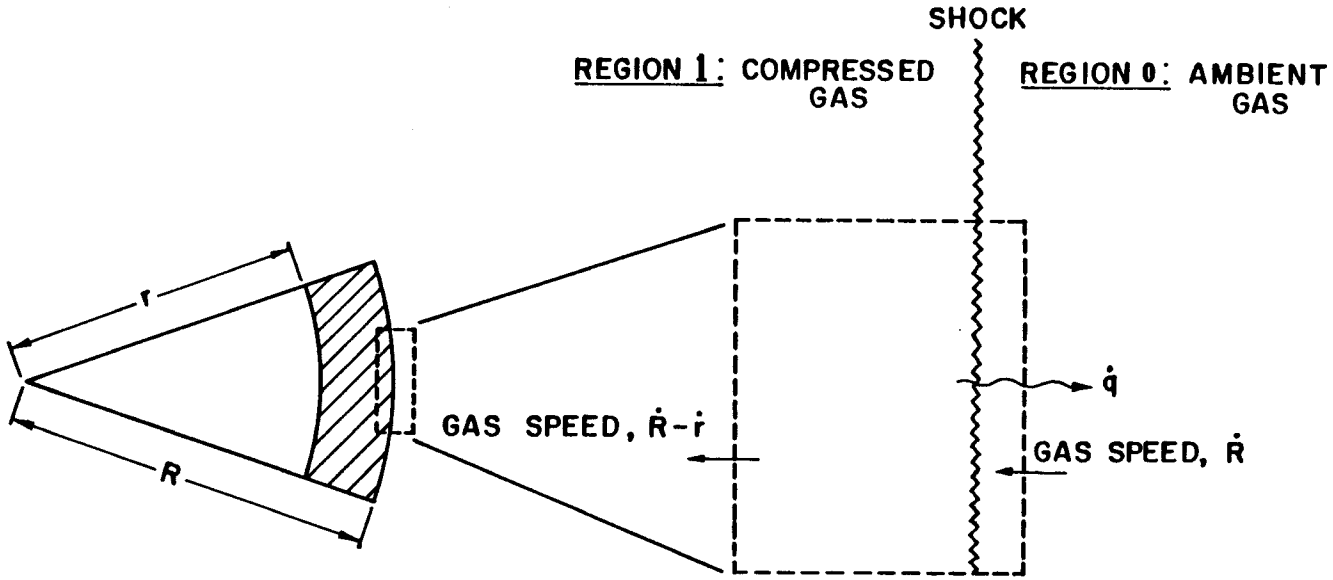

Figure III-7. The volume element used for the energy analysis. The element is fixed to the shock front.

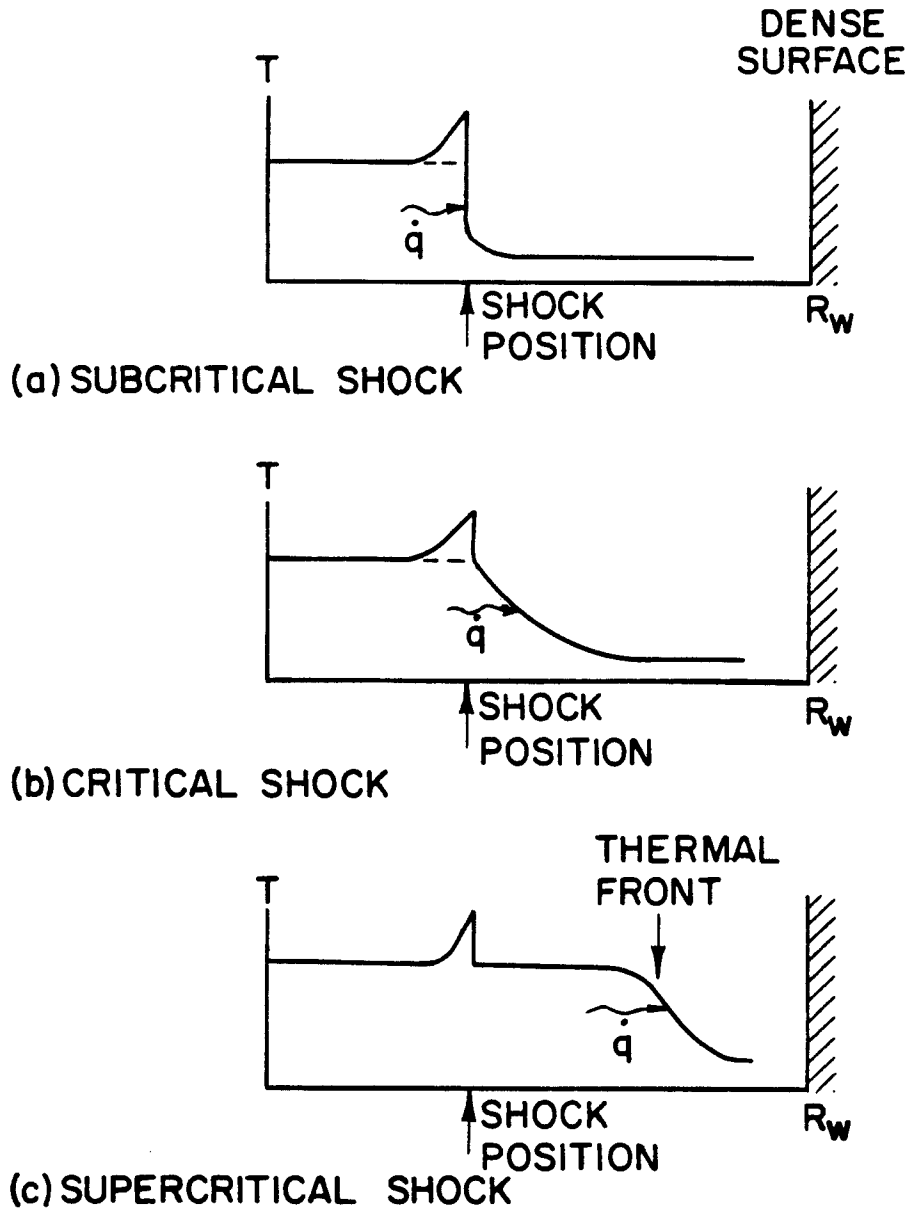

Figure III-8. Temperature profiles for a: (a) subcritical, (b) critical, (c) supercritical shock wave. These profiles illustrate the trend of radiation transport in a high density, intermediate density, and low density gas, respectively.

shock front. This is analogous to Stage A of the response of the atmosphere to a nuclear explosion. Stage A might be the only stage that occurs if the gas density is low enough. For a supercritical shock, the enthalpy difference between the gas on each side of the shock can be neglected to write Equation (28) as

$$\dot{q} \approx \frac{2}{(\gamma + 1)^2} \rho_o \dot{R}^3 \quad , \tag{29}$$

Once the thermal wave has reached the wall at R_w, the radiation flux emitted from the debris driven shock to the wall is

$$\dot{q} = \frac{2}{(\gamma + 1)^2} \rho_o \dot{R}^3 \left(\frac{R}{R_w}\right)^2 \quad . \tag{30}$$

C.3. An Example of a Debris Driven Shock in a Low Density Gas

The expressions that have been derived in this section are compared here to a numerical solution of the radiation hydrodynamic equations. The numerical solution includes the effects of the debris-gas interaction. Other details of the numerical model are given in the chapters that follow. Argon gas mixed with two volume percent sodium was chosen for the example presented here. The density of the mixture is 10^{15} atoms/cm^3 (2.8×10^{-2} torr at standard temperature), and the radius of the spherical cavity containing the gas is 4 meters. A total of 15 MJ of 0.3 keV blackbody x-rays were assumed to be emitted from an ICF target at the center of the cavity. An x-ray deposition calculation shows that only 2.5 MJ of the x-rays

are absorbed by the gas. One gram of iron with 15 MJ of the yield was assumed for the pellet debris. The range of the iron ions is about 71 cm in a stationary gas with this composition and density. Equation (19) is negative for this gas density, target mass, and debris range, so the debris will drive a shock rather than stream through the gas.

The shock position as a function of time as computed by Equation (26) is compared to the numerical solution of the radiation hydrodynamic equations in Figure III-9. The value of γ used in the analytic equations was 1.1. Equation (26) initially predicts a swifter shock than the numerical solution because its derivation assumes all the debris energy goes directly into kinetic energy of the gas, whereas the numerical solution accounts for the fraction that goes into increasing the enthalpy of the gas. At later times, when the shock is of intermediate strength, the numerical solution predicts a larger shock speed than the analytic equation. The reason for this discrepancy is that the ambient pressure was neglected in deriving Equation (26). As a result, Equation (26) overestimates the time to reach the wall by about 20%.

For the low density gas in this example, the thermal front moves much faster than the debris driven shock. The numerical solution shows the thermal front reaches the wall about 10^{-7} seconds after the pellet begins to expand. Any subsequent radiation emitted by the shock is absorbed by the wall. Figure III-10 compares the heat flux at the wall computed by Equation (30) with that from the numerical

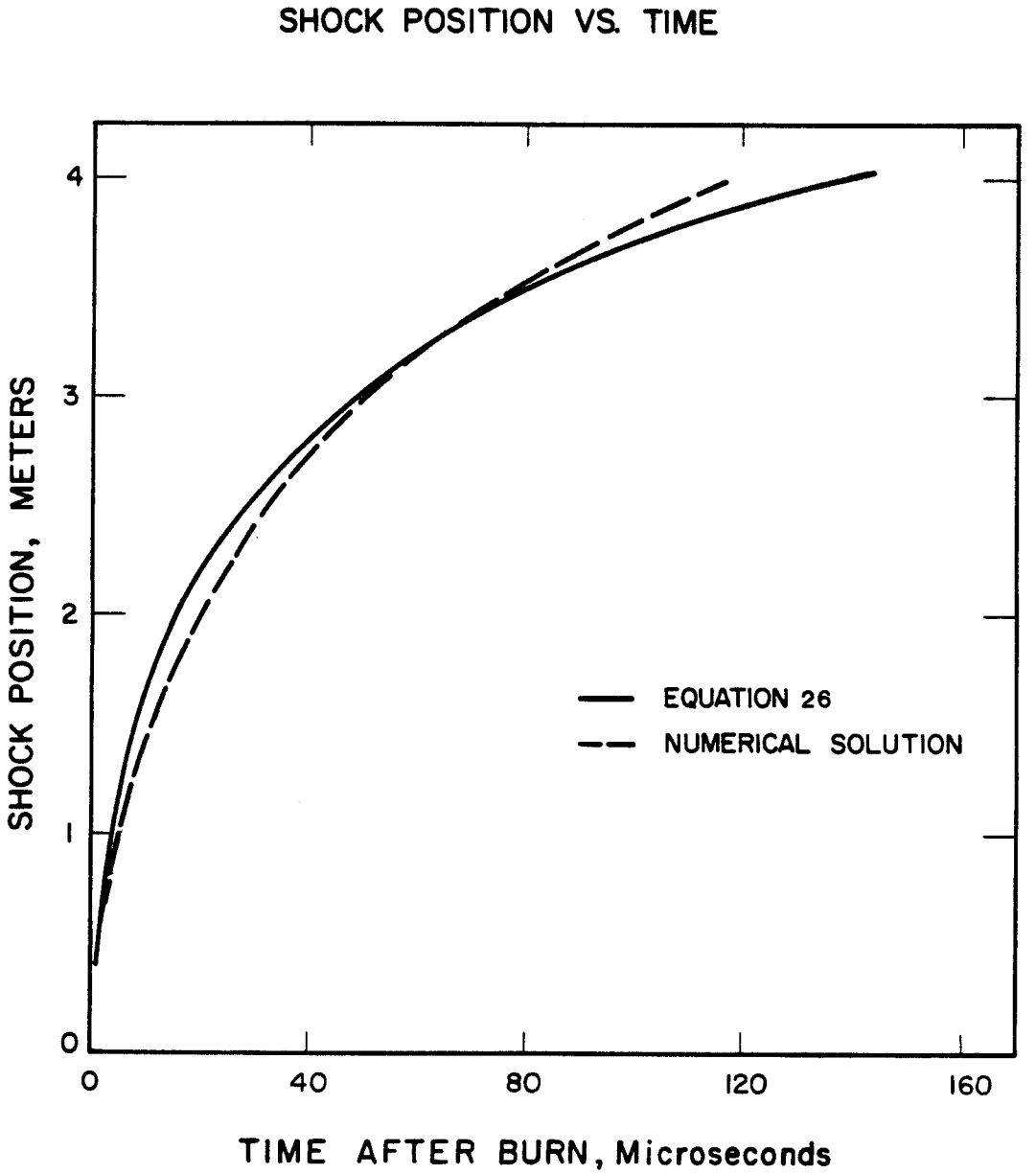

Figure III-9. The shock position as a function of time for the analytic equation and the numerical solution of the radiation hydrodynamic equations.

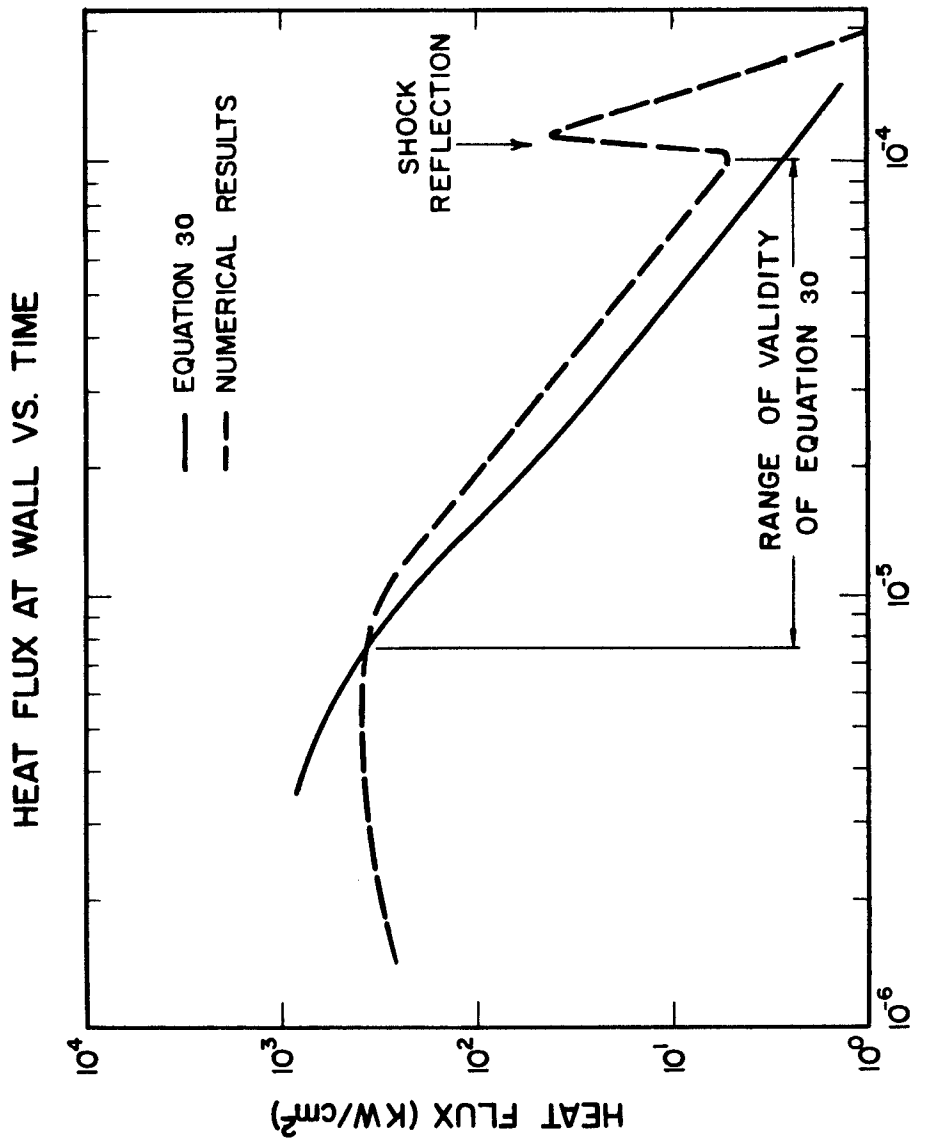

Figure III-10. The heat flux at the wall as a function of time.

solution. At small times the assumption that the enthalpy of the shock heated gas is negligible breaks down, so Equation (30) overestimates the heat flux. But for the times between 7×10^{-6} s to 1×10^{-4} s the two heat flux curves show the same general behavior. This corresponds to the time it takes the debris driven shock to traverse from one meter in radius to the wall. Equation (30) underestimates the heat flux emitted to the wall during this period because the energy emitted by the gas behind the shock has been neglected.

CHAPTER IV

A TRANSPORT MODEL FOR NONEQUILIBRIUM RADIATION

Nonequilibrium radiation is defined in this thesis as thermal radiation that is emitted by a region at one temperature and transported into a region that is at a different temperature. A two temperature model for nonequilibrium radiation transport is described in Section A of this chapter. In the two temperature model, one temperature describes the thermodynamic state of the radiating medium, and the other, the radiation temperature, describes the frequency spectra of the radiation field. One of the contributions of this thesis is that a reasonable method of computing the radiation temperature is arrived at by deriving the two temperature model from general equations of radiation transport. The conditions required for applicability of the model become clear during the derivation. The motion of the medium and thermal conduction are neglected in Section A, so as to emphasize the details of the model.

The two temperature model is applied in Section B to a uniform medium in which a spherical volume is heated to a very high temperature. The equations are used to follow the development of the heated volume through four stages, each stage illustrating how the temperature dependence of the opacity affects radiation transport. A new analysis of a cooling wave was developed to study one of the stages. The new analysis can be applied to determine whether a cooling wave will or will not occur for any particular explosion, and some

examples are discussed. As in Section A, the motion of the medium and thermal conduction are neglected.

A. The Two Temperature Model

The radiation energy density at a point of interest can be computed by accounting for the radiation transported, scattered, absorbed, and emitted throughout the medium. The transport equation used to compute the radiation energy density is similar in form to the transport equation used in other fields, such as neutronics. But unlike these other fields, some of the terms in the radiation transport equation are strongly influenced by, as well as strongly influence, the temperature of the medium. Because of this interdependence, the radiation transport equation must often be solved simultaneously with the temperature equation of the medium.

The ions and electrons that comprise the medium are assumed to be perfect gases in equilibrium with each other. Hence, the temperature and one other thermodynamic variable is enough to specify the thermodynamic state. The temperatures of interest in computing the response of an ICF cavity gas range from a fraction of an electron volt to about 100 eV. At these temperatures, the Thompson scattering cross section is much smaller than the photoelectric cross section, so the scattering term can be omitted from the transport equation. In order to focus attention on the radiation transport model, the terms that account for the motion of the medium and thermal conduction will not be introduced until Chapter V. In one dimension, the spectral energy density and temperature are described by

$$\frac{\partial U_\nu(r,t)}{\partial t} + \nabla\cdot\bar{s}_\nu(r,t) = \text{emission rate} - \text{absorption rate} \ , \qquad (31.a)$$

$$\rho(r)C_v(r,t)\frac{\partial T(r,t)}{\partial t} = - \text{emission rate} + \text{absorption rate} \ , \qquad (31.b)$$

where U_ν is the spectral energy density, and $\bar{s}_\nu$ is the spectral radiation flux. The subscript "ν" denotes the frequency dependence. The divergence of the flux has been left in vector notation because it depends on whether planar, cylindrical, or spherical geometry is being considered.

An expression for the absorption rate follows from the definition of the radiation mean free path, $\ell_\nu(T)$:

$$\text{absorption rate} = \frac{cU_\nu(r,t)}{\ell_\nu(T)} \ , \qquad (32)$$

where c is the speed of light. When solving the radiation transport equations, values for the mean free path are obtained from models of the interaction of radiation with matter.[49,50]

An expression for the emission rate is obtained by first considering emission in an infinite medium with a uniform temperature. The spectral radiation energy density in such a medium is given by the Planck function,

$$U_{\nu P}(T) = \frac{8\pi h\nu^3}{c^3}\frac{1}{\exp\left(\frac{h\nu}{kT}\right) - 1} \ , \qquad (33)$$

where h is Planck's constant and k is Boltzmann's constant. Kirchoff's law states that emission exactly balances absorption in such a body, so

$$\text{emission rate} = \frac{cU_{\nu P}(T)}{\ell_{\nu}(T)} \quad . \tag{34}$$

If thermodynamic equilibrium between the electrons and ions of the medium is dominated by collisional processes, then equilibrium is independent of the radiation field, and the medium is said to be in local thermodynamic equilibrium (LTE).[50] The concept of LTE is very important, because it allows the emission rate to be computed from Equation (34) even when the spectral radiation energy density is not given by the Planck function. In this thesis, the radiating medium is always assumed to be in LTE. If the assumption of LTE is not valid, then the emission rate must be computed by solving rate equations that describe the various electron transitions, which can add substantially to the cost of solving the radiation transport equations.

Before Equations (31.a) and (31.b) can be solved, the radiation transport term must be expressed as a function of the spectral energy density. Let r_o represent the characteristic dimension of a radiating medium that is surrounded by a vacuum. If $r_o/\ell_{\nu} \gg 1$ within the body, then the emitted radiation is all reabsorbed except near the edges, where some escapes. Thermal radiation is emitted isotropically, so the spectral radiation intensity within the body will also be

isotropic, except near the edges. It has been shown that radiation transport is diffusive under these conditions, so the flux is related to the spectral energy density by[49-51]

$$(\overline{s}_\nu(r,t))_{diff} = -\frac{c\ell_\nu(T)}{3} \nabla U_\nu(r,t) \quad . \tag{35}$$

Radiation can escape from the layer that extends a few mean free paths into the medium, and be emitted into the surrounding vacuum. The assumption of an isotropic radiation intensity does not apply to this layer, and Equation (35) may give values of the flux that exceed physical limitations. The maximum flux possible is

$$(\overline{s}_\nu(r,t))_{slip} = \overline{f} c U_\nu(r,t) \quad , \tag{36}$$

where $\overline{f}$ is a measure of the isotropy of the radiation intensity. The magnitude of $\overline{f}$ lies between 1 and 1/4, corresponding to a completely anisotropic and completely isotropic intensity, respectively. The direction of $\overline{f}$ is opposite to the direction of the gradient in radiation energy density. Methods of evaluating $\overline{f}$ in single[52] and multidimensional[53] configurations have been discussed in the literature. However, for computational convenience, the magnitude of $\overline{f}$ will always be taken as unity in this thesis.

Having established the limiting expression for the flux in the diffusive and the free streaming (or radiation slip) limit, a more general expression for the flux will be presented. For planar geome-

tries, Probstein[54] suggested the expression

$$\bar{s}_\nu(r,t) = \frac{(\bar{s}_\nu)_{diff}}{1 + \frac{|(\bar{s}_\nu)_{diff}|}{|(\bar{s}_\nu)_{slip}|}} \quad . \tag{37}$$

Deissler[55] and Kershaw[56] have since derived Equation (37) from the general equations of radiation transport. Deissler[55] also derived similar expressions for cylindrical and spherical geometries, and compared the accuracy of these approximate expressions to Monte Carlo solutions of the transport equations. It was found that Equation (37) differs by only a few percent from the Monte Carlo results. Equation (37) is the expression for the flux that is used in this thesis. The justification for using Equation (37) in cylindrical and spherical geometries is that these geometries can always be divided into approximately planar cells when the problem is one-dimensional.

The effect of stimulated emission on a medium in LTE can be accounted for by dividing the mean free path by the factor $(1 - \exp(h\nu/kT))$.[50] When averaged over frequency, this factor is close to unity for a medium in LTE. But under special conditions, such as in lasers, stimulated emission can be the dominant emission mechanism. The radiation transport model presented here is only applicable if the contribution from stimulated emission is small, because otherwise the assumption of LTE will be violated. For brevity

in writing the equations that follow, the stimulated emission factor will be omitted. However, stimulated emission will be included when the two temperature equations are written in their final form.

Substituting the above expressions for radiation transport, absorption, and emission into Equations (31.a) and (31.b), the transport equations become

$$\frac{\partial U_\nu(r,t)}{\partial t} + \nabla\cdot\frac{(\bar{s}_\nu(r,t))_{diff}}{1 + \dfrac{|(\bar{s}_\nu(r,t))_{diff}|}{|(\bar{s}_\nu(r,t))_{slip}|}} = \frac{cU_{\nu P}(T)}{\ell_\nu(T)} - \frac{cU_\nu(r,t)}{\ell_\nu(T)} , \tag{38.a}$$

$$\rho(r)\, C_v(r,t)\, \frac{\partial T(r,t)}{\partial T} = -\frac{cU_{\nu P}(T)}{\ell_\nu(T)} + \frac{cU_\nu(r,t)}{\ell_\nu(T)} . \tag{38.b}$$

The independent variables in these equations are time, space, and frequency. If the frequency dependence of the radiation energy density is not of interest, then it is desirable to eliminate the frequency variable by integrating each term over frequency. The emission term can be integrated easily because the frequency dependence of both $U_{\nu P}(T)$ and $\ell_\nu(T)$ is known. But in general, the remaining terms cannot be integrated because the frequency dependence of U_ν is not known before the equations are solved.

Some special circumstances that allow the remaining terms to be integrated are now investigated. By considering these circumstances it becomes clear how the two temperature model can be derived from more general radiation transport equations. If a medium is composed

of only very opaque and very transparent regions, or if the radiation mean free path in a medium is independent of frequency (a grey body), then the radiation spectra emitted from any point retains its Planckian shape as it is transported to other regions. Under these conditions, it may be reasonable to approximate the spectral energy density at any point by what will be referred to as a dilute Planckian function:

$$U_\nu(r,t) = \varepsilon(r,t)\,\frac{8\pi h\nu^3}{c^3}\,\frac{1}{\exp\left(\frac{h\nu}{kT_r}\right) - 1} \quad . \tag{39}$$

The radiation temperature, T_r, specifies the frequency distribution of the spectral energy density, and should be assigned a value that reflects the temperature of the point that created the radiation. In most instances, the radiation that arrives at a point of interest has originated from surrounding points with a variety of temperatures, so a suitable average value of T_r must be defined. The amount of radiation energy that reaches the point of interest from each of the surrounding points is a suitable averaging factor. Hence, the radiation temperature is evaluated by following the flow of radiation energy. The dilution factor, $\varepsilon(r,t)$, specifies the magnitude of the spectral energy density. Deviation of the dilution factor from unit reflects convergence, divergence, and absorption of the photons during transport. Note that in the limiting case of a blackbody, $T_r = T$ and $\varepsilon = 1$, so Equation (39) reverts back to the equilibrium Planck function.

Using the dilute Planckian function to integrate Equations (38.a) and (38.b) over frequency results in

$$\frac{\partial U(r,t)}{\partial t} + \bar{\nabla}\cdot\frac{\bar{s}_{diff}(r,t)}{1 + \dfrac{|\bar{s}_{diff}(r,t)|}{|\bar{s}_{slip}(r,t)|}} = \frac{cU_P(T)}{\ell_P(T)} - \frac{cU(r,t)}{\ell_P(T,T_r)} \quad , \tag{40.a}$$

$$\rho(r)\, C_v(r,t)\, \frac{\partial T(r,t)}{\partial t} = -\frac{cU_P(T)}{\ell_P(T)} + \frac{cU(r,t)}{\ell_P(T,T_r)} \quad , \tag{40.b}$$

where $U_P(T) = 4\sigma T^4/c$,

and $U(r,t)$ is the radiation energy density.

The equilibrium Planck mean free path appears in the emission term, and is defined (including induced emission) as

$$\frac{1}{\ell_P(T)} = \int_0^\infty \frac{G_1(u(T))}{\ell_\nu(T)}\, du \quad , \tag{41}$$

where $$G_1(u) \equiv \frac{15}{\pi^4}\frac{u^3}{\exp(u) - 1} \quad ,$$

and $$u \equiv \frac{h\nu}{kT} \, .$$

The equilibrium Planck mean free path is the frequency averaged distance that photons will travel in a blackbody at temperature T. The nonequilibrium Planck mean free path appears in the absorption term, and is defined by

$$\frac{1}{\ell_p(T,T_r)} = \int_0^\infty \frac{G_1(u(T_r))}{\ell_\nu(T)}\, du \quad , \tag{42}$$

where $$u(T_r) \equiv \left(\frac{h\nu}{kT_r}\right) .$$

The nonequilibrium Planck mean free path is the frequency averaged distance that photons characterized by the radiation temperature, T_r, will travel in a medium at temperature T.

Integrating the flux term over frequency in both the diffusion and the free streaming limit gives

$$\bar{s}_{diff}(r,t) = \frac{c\ell_R(T,T_r)}{3} \bar{\nabla}U(r,t) \quad , \tag{43}$$

and

$$\bar{s}_{slip}(r,t) = \bar{f}cU(r,t) \quad . \tag{44}$$

The nonequilibrium Rosseland mean free path appears in Equation (43), and is defined as (including induced emission)

$$\ell_R(T,T_r) = \int_0^\infty \ell_\nu(T) G(u(T_r))\, du \quad , \tag{45}$$

where $$G(u) \equiv \frac{15}{4\pi^4} \frac{u^4 \exp(-u)}{(1 - \exp(-u))^2} .$$

The nonequilibrium Rosseland mean free path is part of the frequency averaged diffusion coefficient, $c\ell_R(T,T_r)/3$, and should not be confused with the frequency averaged mean free path, $\ell_p(T,T_r)$. These

two mean free paths are not equal unless ℓ_ν is independent of frequency. When radiation is free streaming, the Rosseland mean free path is a useless number, whereas the Planck mean free path is still useful.

Figure IV-1 illustrates the equilibrium Planck and Rosseland mean free paths for both air and argon at standard density. Air is completely disassociated at temperatures greater than a fraction of an electron volt, so above this temperature the differences between the mean free paths of air and argon are solely due to differences in the atomic structure of the constituent atoms. The "well" shape of these curves is characteristic of all gases at these temperatures. For the Planck mean free path the depth of the well is determined by the strength of the photoelectric interaction, whereas for the Rosseland mean free path the depth is sensitive to both photoelectric and line absorption. The steep gradients at the edges of the well indicate that there are cases where a medium will be composed of very opaque and very transparent regions. The two temperature model just discussed is applicable to such cases.

In special instances, Equations (40.a) and (40.b) can sometimes be simplified further to arrive at the radiation heat conduction model[49,50] (sometimes referred to as the equilibrium diffusion model). If the radiation mean free path in a medium is much smaller than the temperature gradient, then the radiation energy density at any point is given by the expression for a blackbody, $U_p(T)$. The only unknown left is the temperature distribution, so Equation (40.a)

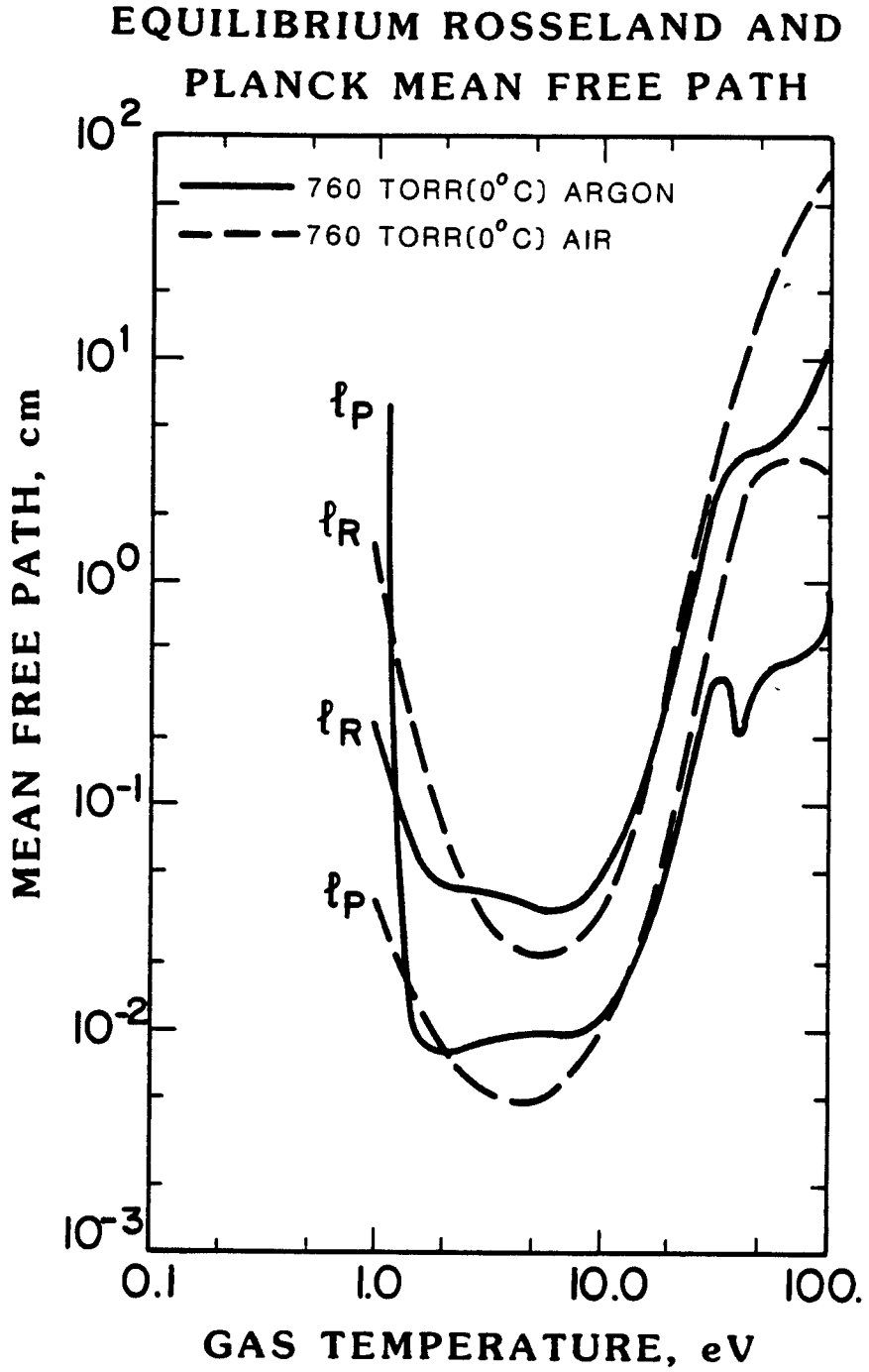

Figure IV-1. The equilibrium Planck and Rosseland mean free paths for air and argon at standard density. These curves were produced for the author by the Theoretical Physics Group, T-4, at Los Alamos National Laboratory, and are the result of theoretical calculations.

and (40.b) can be combined to write the equation for radiation heat conduction;

$$\rho(r)\, C_v(r,t)\, \frac{\partial T(r,t)}{\partial t} + \frac{\partial U_P(r,t)}{\partial t} + \bar{\nabla}\cdot \frac{\bar{s}_{diff}(r,t)}{1 + \dfrac{|\bar{s}_{diff}(r,t)|}{|\bar{s}_{slip}(r,t)|}} = 0 \quad , \tag{46}$$

where $\bar{s}_{diff}$ and $\bar{s}_{slip}$ are defined in terms of $U_P(T)$. Some radiation transport codes[57] use the radiation heat conduction model instead of a nonequilibrium radiation model. However, the radiation conduction model does not apply to many of the cases of interest in this thesis, so Equations (40.a) and (40.b) will be used for the numerical solutions.

B. Radiation Transport in a Sphere Heated to a High Temperature

Radiation transport in a sphere of gas heated initially to a temperature T_o, with radius r_o, will be considered in this section. Figure IV-2 shows the initial temperature profile of the heated volume. The ambient temperature outside of the heated sphere is T_{amb}. The temperature at the center is denoted by T' as the sphere cools, and the radius of the heated volume by r'. The equilibrium Planck and Rosseland mean free paths are also shown in Figure IV-2 as a function of temperature. The temperatures T_1, T_2, T_3, and T_4 denote transition temperatures where the Planck or Rosseland mean free path changes rapidly with temperature. As the temperature of the sphere falls below each transition temperature, the character of

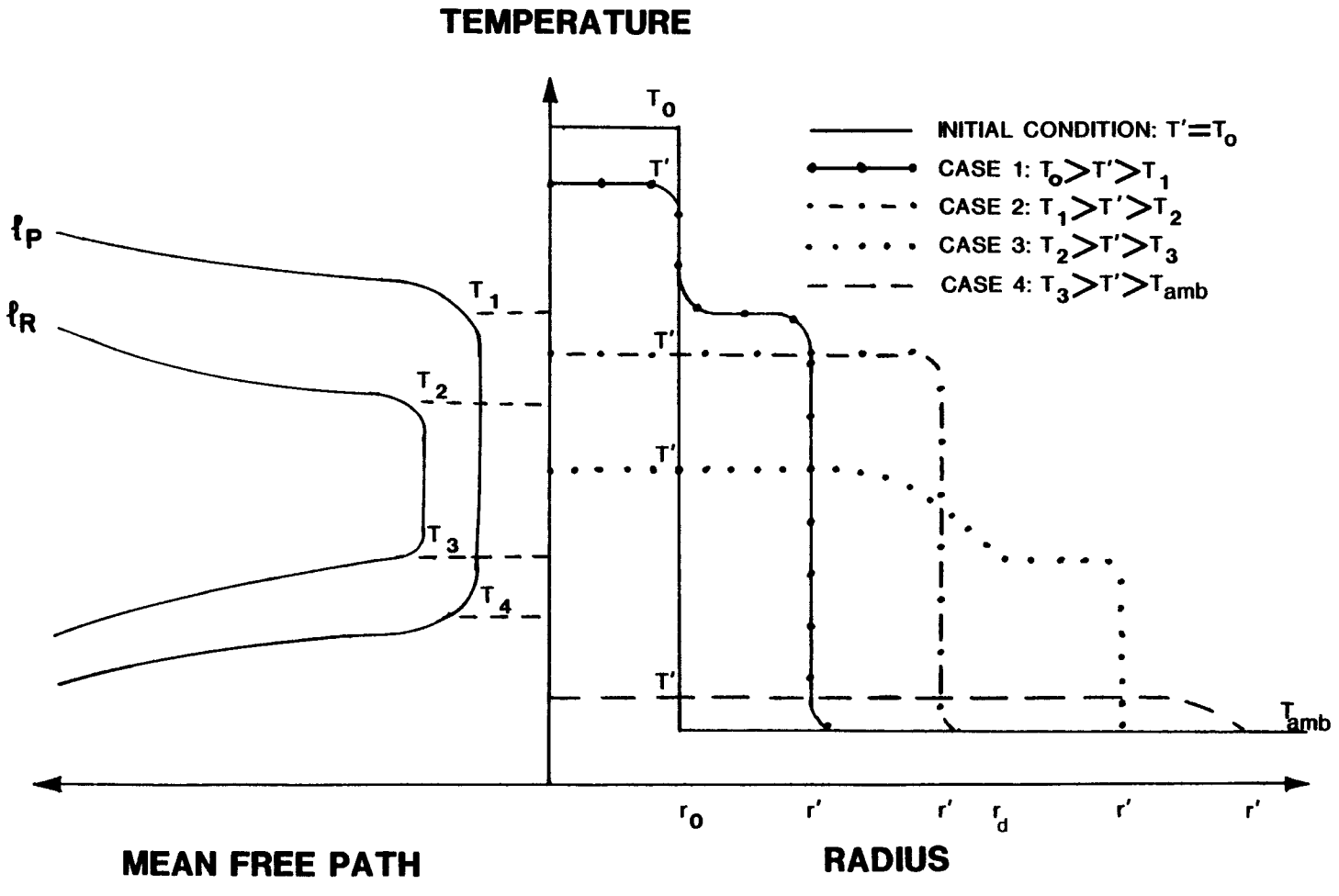

Figure IV-2. Four stages in the development of a sphere of heated gas.

radiation transport can change dramatically. The four cases indicated in Figure IV-2 will now be considered.

B.1. Case 1: $T_o > T' > T_1$

Case 1 is analogous to Stage A of the atmosphere's response to a nuclear explosion. As illustrated in Figure IV-2, the temperature of the gas within r_o is above the upper transparency temperature, T_1. Hence, the gas there is transparent to its own radiation. The radiation emitted from the gas within r_o is transported out to r', where it is absorbed as nonequilibrium radiation. The thermal wave at r' propagates outward as the absorbed radiation heats the cooler gas to transparency.

Because the gas within r_o is transparent, the absorption term in the transport equations can be neglected, and the flux is given by the free streaming limit. In many instances it is also reasonable to assume the radiation energy density within the sphere is in a quasi-steady state, because the time for changes in the radiation energy density is usually much greater than the time for radiation transport (r_o/c). Applying the above assumptions to Equation (40.a) results in

$$\frac{1}{r^2}\frac{d}{dr}\left(r^2 U(r,t)\right) = \frac{U_P(T')}{\ell_P(T')} \quad . \tag{46}$$

The transparent sphere remains isothermal as it cools because it loses energy uniformly. Then the Planck mean free path is constant within the sphere, and Equation (46) can be solved for the flux out of the sphere:

$$\dot{c}U(r_o,t) = \dot{c}U_p(T') \frac{r_o}{3\ell_p(T')} = \sigma T'^4 \frac{4r_o}{3\ell_p(T')} \quad . \qquad (47)$$

This flux is much less than that of a blackbody because $r_o/\ell_p << 1$.

The temperature equation can be applied to the transparent sphere to evaluate the time dependence of T'. Neglecting the absorption term in Equation (40.b) results in

$$\rho C_v(T') \frac{dT'}{dt} = \frac{cU_p(T')}{\ell_p(T')} \quad . \qquad (48)$$

Once the temperature dependence of the specific heat and Planck mean free path is specified, Equation (48) can be solved for T'(t).

The propagation speed of the thermal wave front at r' is denoted by $\dot{r}'$. It can be evaluated by equating the energy absorbed at r' to the increase in enthalpy there. In the reference frame fixed to r', this equality is

$$4\pi r_o^2 \dot{c}U(r_o,t) = 4\pi r'^2 \rho C_{vl}(T_1 - T_{amb})\dot{r}' \quad , \qquad (49)$$

where C_{vl} is the specific heat averaged between T_1 and T_{amb}. Once the time dependence of T' is known, the time dependence of r' can be found by integrating Equation (49).

B.2. Case 2: $T_1 > T' > T_2$

Case 2 begins as the gas within r' cools below the upper transparency temperature, T_1. The Planck mean free path then becomes

small enough that the absorption term in the transport equations can no longer be neglected. The Rosseland mean free path is still very large, so radiation transport is still flux limited. A thermal wave continues to propagate outward as the radiation transported to r' is absorbed as nonequilibrium radiation.

Assuming the radiation energy density within r' is quasi-steady, Equation (40.a) can be written as

$$\frac{1}{r^2}\frac{d}{dr}\left(r^2 U(r,t)\right) = \frac{U_P(T')}{\ell_P(T')} - \frac{U(T')}{\ell_P(T')} \quad . \tag{50}$$

The gas within r' is assumed to be isothermal because flux limited radiation transport is fast enough to relax any gradients in temperature. Hence, the Planck mean free path is constant within the sphere, and Equation (50) can be solved by the methods applicable to ordinary differential equations. The solution for the flux at r' is

$$cU(r',t) = cU_P(T')\left[1 - \frac{2\ell_P(T')}{r'} + \frac{2\ell_P^2(T')}{r'^2}\left(1 - \exp\left(-\frac{r'}{\ell_P(T')}\right)\right)\right]. \tag{51}$$

The maximum flux, $cU_P(T')$, is that of a blackbody, and occurs when $\ell_P(T') \ll r'$. The minimum flux occurs when $\ell_P(T') \gg r'$, and can be found by expanding the exponential and canceling the appropriate terms. The result is identical to Equation (47), but with r_o replaced by r'.

The time dependence of the temperature T' is found by solving Equation (40.b), which in Case 2 is

$$\rho C_v(T') \frac{\partial T'}{\partial t} = \dot{c} \frac{U(T') - U_P(T')}{\ell_P(T')} \quad . \tag{52}$$

The function $U(T')$ is given by Equation (51). Given the temperature dependence of the specific heat and Planck mean free path, Equation (52) can be solved for $T'(t)$.

The propagation speed of the thermal wave front, $\dot{r}'$, is found in a manner similar to Case 1. The appropriate equation is

$$4\pi r'^2 cU(r',t) = 4\pi r'^2 \rho C_{v2}(T' - T_{amb})\dot{r}' \quad , \tag{53}$$

where C_{v2} is the specific heat averaged between T' and T_{amb}. The time dependence of r' is determined by integrating Equation (53) after $T'(t)$ is known.

B.3. Case 3: $T_2 > T' > T_3$

There are two thermal waves to be considered in Case 3. Radiation transport is diffusive in the region with temperatures between T_2 and T_3, which is between $r = 0$ and r_d in Figure IV-2. The energy radiated in this volume is all reabsorbed except near the edges, where the radiated flux is about σT_3^4. Radiation is transported more rapidly in the region between r_d and r', so the radiation escaping from the diffusive volume is transported to r' and absorbed there as nonequilibrium radiation. Thus, a thermal wave develops at the edge of the diffusive region, where energy is being emitted, and at r', where the energy is being absorbed.

In Case 3, the temperature profile can develop in one of two ways. If energy is radiated at r_d faster than it is replenished by energy diffusing from deeper within the diffusive region, then a cooling wave will sweep inward. On the other hand, if energy diffuses to r_d faster than it is radiated away, then a diffusion wave will propagate outward. To determine which of these possibilities will occur, an energy balance at r_d is considered. Figure IV-3 shows two control surfaces moving with r_d. The net enthalpy flux across these surfaces is balanced by the radiation diffusion flux in from the left, and the free streaming radiation flux out from the right. The speed of energy transport by diffusion is denoted by $\dot{r}_{diff}$. Using the energy balance to solve for the speed of the thermal wave at r_d,

$$\dot{r}_d = \frac{\dot{r}_{diff}\rho C_v(T')T' - \sigma T_3^4}{\rho C_v(T')T' - \rho C_v(T_{amb})T_{amb}} \quad . \tag{54}$$

Equation (54) can have positive and negative values, corresponding to a diffusion wave and a cooling wave, respectively.

To utilize Equation (54) in a practical way, the speed that energy is transported by radiation diffusion, $\dot{r}_{diff}$, must be evaluated. This can be done by solving the radiation heat conduction equation for a completely opaque gas (i.e., no free streaming). Equation (46) applies to such a gas, and neglecting the radiation energy density, can be written as

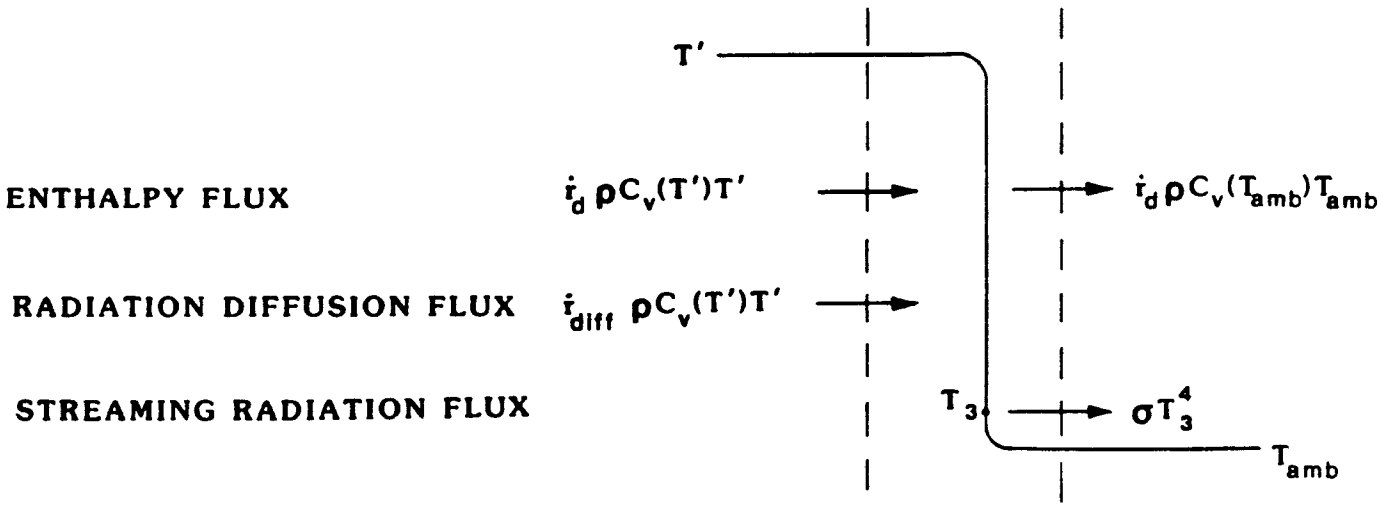

Figure IV-3. The energy balance at a thermal wave front.

$$\rho C_v(T') \frac{\partial T'}{\partial t} - \frac{1}{r^2} \frac{\partial}{\partial r} \left(r^2 \frac{16\ \sigma \ell_R(T')}{3} T'^3 \frac{\partial T'}{\partial t} \right) = 0 \quad . \qquad (55)$$

Barenblatt[58] used similarity methods to analytically solve Equation (55) for an instantaneous point explosion in a medium with a temperature independent specific heat and $\ell_R(T') = AT'^m$. Using that solution, the radiation diffusion speed can be approximated as

$$\dot{r}_{diff} \approx \frac{\xi^{3n+2}}{3n+2} \left(\frac{4\pi}{3}\right)^{(3n+1)/3} \frac{16\ \sigma A}{3\rho C_v} \left(\frac{\rho C_v}{E}\right)^{1/3} T'^{(3n+1)/3} \quad , \qquad (56)$$

where $\xi = \left[\frac{3n+2}{2^{n-1} n\pi}\right]^{1/(3n+2)} \left[\frac{\Gamma(\frac{5}{2} + \frac{1}{n})}{\Gamma(1 + \frac{1}{n})\Gamma(\frac{3}{2})}\right]^{n/(3n+2)}$,

Γ = the gamma function,

and $n = m + 3$.

Equation (56) shows the radiation diffusion speed decreases inversely with the cube root of the deposited energy, E. Hence, the tendency for a cooling wave to occur increases as the deposited energy increases.

Equations (54) and (56) constitute a more complete analysis of the cooling wave than has been provided in the literature,[38-40] and will now be applied to an explosion in standard density air. A 30 MJ and 10^{14} MJ yield will be considered, corresponding to the nominal yield of an ICF target and a nuclear weapon, respectively. These examples illustrate how the magnitude of the deposited energy

influences the observed phenomena. In each case the explosion produces gas motion that sweeps out most of the air mass, leaving the density in the diffusive region about two orders of magnitude less than standard density. For simplicity, a constant mean free path is assumed (n = 3). The minimum Rosseland mean free path is about 2 cm at this density, and occurs at T' ≈ 5 eV. The specific heat is about 10^{12} erg/gm/eV at this temperature and density. The transparency temperature, T_3, is about 1 eV, as can be seen from Figure IV-1. Using the above information, Equations (54) and (55) indicate that a diffusion wave at r_d will propagate outward at about 3 x 10^6 cm/s for the 30 MJ yield. This is consistent with what has been found with numerical solutions to the radiation hydrodynamic equations.(59) For the 10^{14} MJ yield, a cooling wave propagates inward at about 2 x 10^4 cm/s. This result is consistent with what has been observed in weapons tests.(49)

B.4. Case 4: $T_4 > T' > T_{amb}$

Case 4 begins as the temperature of the heated gas drops below the lower transparency temperature, T_4. The sphere is transparent below this temperature, and the radiation emission rate decreases to the value given by Equation (47), but with r_o replaced by r'. After the decrease in the emission rate, the sphere cools mainly by convective mixing with the cooler surroundings.

In the design of a gas filled ICF reactor, it is useful to know the size of the sphere when it becomes transparent. If the sphere does not become transparent before it reaches the wall, the heat flux

absorbed by the wall can be much higher than otherwise. The sphere's size when it becomes transparent can be estimated by equating the energy absorbed by the gas, E, to the enthalpy increase,

$$E = \frac{4}{3} \pi r'^3 \rho C_{v4} (T_4 - T_{amb}) \quad , \tag{57}$$

where C_{v4} is the specific heat averaged between T_4 and T_{amb}. For pure argon gas, T_4 is about 1.5 eV and C_{v4} is about 4×10^4 J/eV/gm. Figure IV-4 shows the size of the sphere when it becomes transparent for various pellet yields and gas densities. In a laser fusion reactor, where the gas density is on the order of 10^{-3} atm (0°C), the size of the heated volume when it becomes transparent will be about 4 m for a 30 MJ yield. For a cavity smaller than this, a significant amount of first wall evaporation can be expected. By the same reasoning, little evaporation is expected for the first wall of a light ion driven reactor, where the cavity gas density is about 10^{-2} atm (0°C).

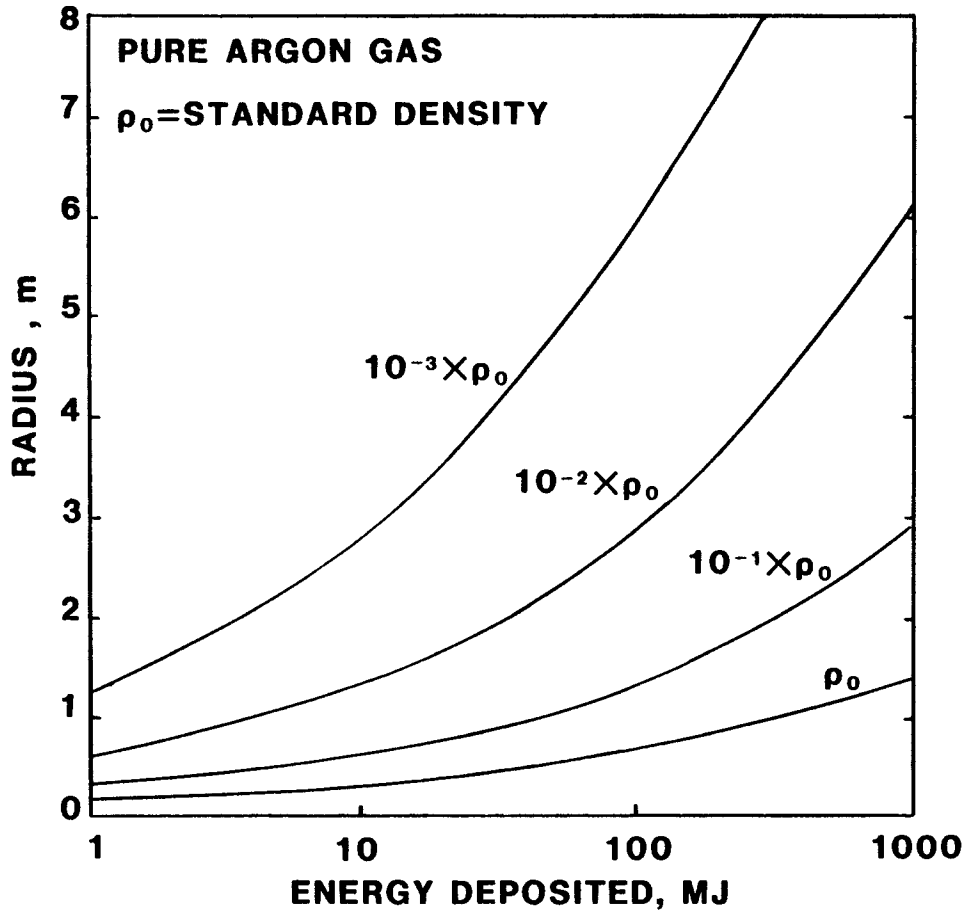

Figure IV-4. The radius of a volume of argon gas when it becomes transparent for various gas densities and target yields.

CHAPTER V

NONEQUILIBRIUM RADIATION TRANSPORT WITH HYDRODYNAMIC MOTION, THERMAL CONDUCTION, AND SOURCES OF ENERGY AND MOMENTUM

The radiation transport model described in the previous chapter is modified in Section A of this chapter to include the effects of hydrodynamic motion, thermal conduction, and sources of energy and momentum. The equations are written in the Lagrangian reference frame, which follows the motion of a point moving with the fluid.

One of the goals of this thesis is to provide a suitable method for computing the deposition of target x-rays in a cavity gas. In Section B, the justification for using an exponential attenuation model is discussed. The calculation is complicated by the fact that the attenuation coefficient decreases as the x-rays ionize the gas. A method for computing the attenuation coefficient as a function of ionization is also presented.

Another goal of this thesis is to provide a method for computing the deposition rates of internal energy and momentum from the target debris into a cavity gas. The method that has been developed is described in Section C, and requires a few parameters from the output of an ion transport code. These parameters are used to compute the energy of the debris ions as a function of time and space in the gas, from which the energy and momentum deposition rates easily follow.

A. The Equations of Radiation Hydrodynamics

A.1. The Momentum Equation

In Lagrangian coordinates, the one-dimensional equation of motion for a cavity gas is

$$\rho(r,t)\,\frac{\partial u(r,t)}{\partial t} = -\frac{\partial}{\partial r}\left(P(r,t) + P_r(r,t) + q(r,t)\right) + S_{mom}(r,t)\ , \quad (58)$$

where: P is the gas pressure,

P_r is the radiation pressure,

q is the artificial viscosity,

S_{mom} is the rate that momentum is imparted to the gas.

If the ions and electrons that constitute the gas are in equilibrium with each other, then the local gas pressure is related to the local temperature and density by the perfect gas law,[60]

$$P = n(1 + Z)\,kT\ , \quad (59)$$

where n is the number density of gas atoms, and Z is the number of free electrons per gas atom. The number density of gas atoms is computed by following the initial density profile as a function of time and space. The degree of ionization, on the other hand, is a function of the thermodynamic state of the gas, and is computed by statistical mechanical and quantum mechanical models of matter,[49] or is measured by experiment. The degree of ionization is usually given as a function of temperature and density.

An exact calculation of the radiation pressure vector, $\overline{P}_r$, requires taking the first moment of the radiation intensity over all angles. The first moment yields

$$\overline{P}_r(r,t) = \overline{f}(r,t)\, U(r,t) \quad , \tag{60}$$

where $\overline{f}$ is the Eddington factor.[50,51] The Eddington factor is a measure of the isotropy of the radiation field and ranges in magnitude from 1/3 to 1, depending on whether the radiation intensity is completely isotropic or completely anisotropic, respectively. For the range of temperatures and densities of interest in the gas protection concept, the radiation pressure is a very small component of the total pressure. Hence, the value used for the Eddington factor will not affect the accuracy of the solution. In this thesis, $|\overline{f}| = 1/3$ will be assumed, implying the radiation pressure is isotropic.

The purpose of the artificial viscosity, q, is to spread gradients in the thermodynamic variables over distances resolvable by the Lagrangian mesh chosen for the numerical solution. The first researcher to derive an expression that preserves the Hugoniot relations across the shock was von Neumann.[61] The function used in this thesis is somewhat easier to evaluate than that derived by von Newmann, and is[62]

$$q = 2(\Delta u)^2 \rho \quad , \quad \dot{\rho} > 0$$
$$= 0 \quad , \quad \dot{\rho} < 0 \tag{61}$$

where Δu is the velocity difference between adjacent Lagrangian zones, and $\dot{\rho}$ is the time rate of density change.

The momentum of the target x-rays has a negligible influence on the motion of the cavity gas. However, this may not be the case for the target debris. The momentum deposition rate of the debris is

$$S_{mom}(r,t) = -\rho_d(r,t) \frac{\partial u_{dr}(r,t)}{\partial t} \quad , \tag{62}$$

where ρ_d is the density of the debris, and $\partial u_{dr}/\partial t$ is the acceleration of the debris in the direction of gas motion. A method for evaluating the debris acceleration is described in Section C.

A.2. The Energy Equation

When the two temperature radiation transport equations are modified to include hydrodynamic motion, thermal conduction, and sources of internal energy, they appear as

$$\frac{\partial U}{\partial t} = -\nabla \cdot \bar{s} - P_r \delta \dot{V} + \frac{4\sigma T^4}{\ell_p(T)} - \frac{cU}{\ell_p(T,T_r)} \tag{63.a}$$

$$\rho C_v \frac{\partial T}{\partial t} = \frac{1}{r^{\delta-1}} \frac{\partial}{\partial r} (r^{\delta-1} K \frac{\partial T}{\partial r}) - \frac{\partial P}{\partial T} \rho \dot{V} T - q\rho\dot{V}$$
$$- \frac{4\sigma T^4}{\ell_p(T)} + \frac{cU}{\ell_p(T,T_r)} + S_{int} \tag{63.b}$$

where: K is the thermal conductivity of the gas,

$\dot{V}$ is the rate of specific volume change,

S_{int} is the internal energy deposition rate,

δ is 1, 2, and 3, for planar, cylindrical, and spherical coordinates, respectively.

In writing the temperature equation, the thermodynamic identity[62]

$$\frac{1}{\rho}\frac{\partial(\rho e)}{\partial t} + P\dot{V} = C_v \frac{\partial T}{\partial t} + \frac{\partial P}{\partial t}\dot{V}T \qquad (64)$$

has been used to express the specific internal energy, e, in terms of temperature.

Spitzer's[63] expression for the thermal conductivity of free electrons interacting with stationary ions is a suitable estimate for the thermal conductivity. The theoretically derived expression is usually modified with an experimentally determined constant to prevent it from diverging as the ionization, Z, approaches zero. The modified expression is

$$K = 122 \frac{T^{5/2}}{(Z + 4) \ln \Lambda} \qquad \frac{J}{s\text{-}cm\text{-}eV}, \qquad (65)$$

where T is in eV, and $\ln \Lambda$ is the Coulomb logarithm. For the temperatures and densities of interest in the gas protection concept, the energy transported by thermal conduction is much smaller than the energy transported by radiation. Hence, the thermal conduction term does not significantly influence the solution of the energy equations.

The target x-rays deposit their energy on a much smaller time scale than the hydrodynamic relief time of the cavity gas, so the x-ray deposition can be modeled as instantaneous. However, the energy deposited by the debris must be computed dynamically. An expression for the deposition rate of internal energy from the debris, S_{int}, follows from conservation of debris energy:

$$- \rho_d u_d \frac{\partial u_d}{\partial t} = S_{int} + \rho u \left(\frac{\partial u}{\partial t}\right)_{P=0} \quad . \tag{66}$$

The quantity in parenthesis is the acceleration of the gas due to the debris alone, that is, excluding pressure gradients. It can be evaluated from conservation of debris momentum:

$$\rho \left(\frac{\partial u}{\partial t}\right)_{P=0} = -\rho_d \frac{\partial u_{dr}}{\partial t} \quad . \tag{67}$$

Combining the above equations and solving for the source term yields

$$S_{int} = -\rho_d u_d \frac{\partial u_d}{\partial t} + \rho_d u \frac{\partial u_{dr}}{\partial t} \quad . \tag{68}$$

Once the debris acceleration, $\partial u_d/\partial t$, and the component of the debris acceleration in the direction of gas motion, $\partial u_{dr}/\partial t$, are both known as functions of time and space, then the internal energy deposition rate can be evaluated.

B. Energy Deposition from Target X-Rays

B.1. The Point Source Model

The attenuation of target x-rays in the buffer gas is particularly simple to model if secondary emission from the gas is negligible. Secondary emission occurs by scattering of the primary x-rays or fluorescence of the gas. If secondary emission is negligible, then the target can be modeled as a point source of x-rays that are attenuated exponentially. The point source model is used in this thesis to compute the x-ray energy deposition, and the conditions for applicability of the model are discussed in the following paragraphs. In instances where the point source model does not apply, more sophisticated methods of computing x-ray transport can be applied.(64)

Figure V-1 illustrates the energy dependence of the x-ray attenuation coefficient for three noble gases at 1 torr (0°C). At the lower energies ($\lesssim$ 10 to 100 keV), where the attenuation coefficient is strongly energy dependent, the photoelectric effect is the dominant interaction. At the higher energies ($\gtrsim$ 10 to 100 keV), where the energy dependence of the attenuation coefficient is weak, scattering is the dominant interaction. Hence, scattering can be neglected as long as the energy of the x-rays is less than about 10 keV. To illustrate that this condition may be satisfied, Figure V-2 shows the time integrated x-ray spectra emitted by a possible ICF target.(65) By examining Figures V-1 and V-2, it is evident that for this spectrum x-ray scattering will be negligible.

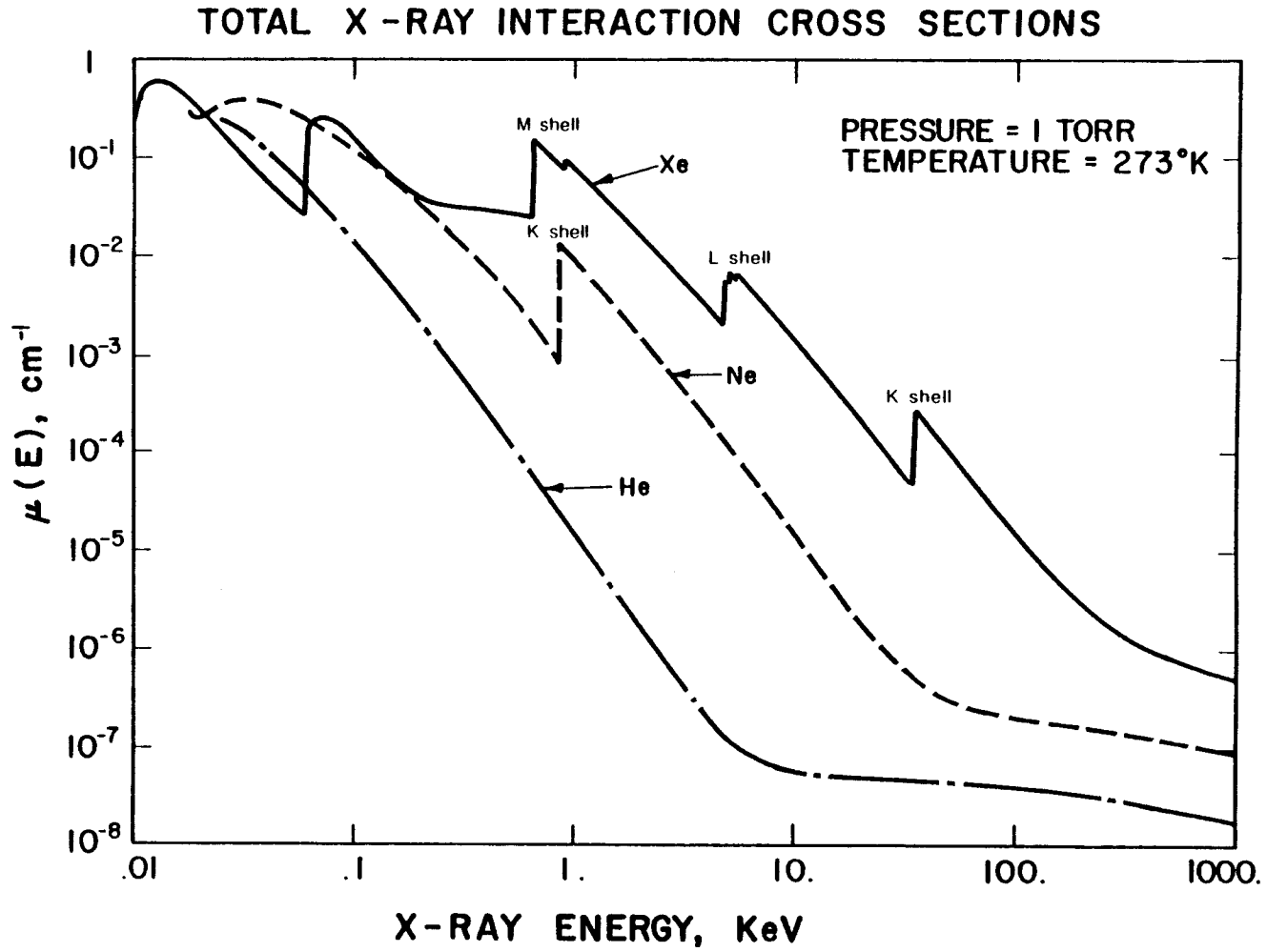

Fig. V-1. The attenuation coefficient for some noble gases. Scattering is the dominant interaction at the high energy end of the curves where the attenuation coefficients are less energy dependent (Ref. 66).

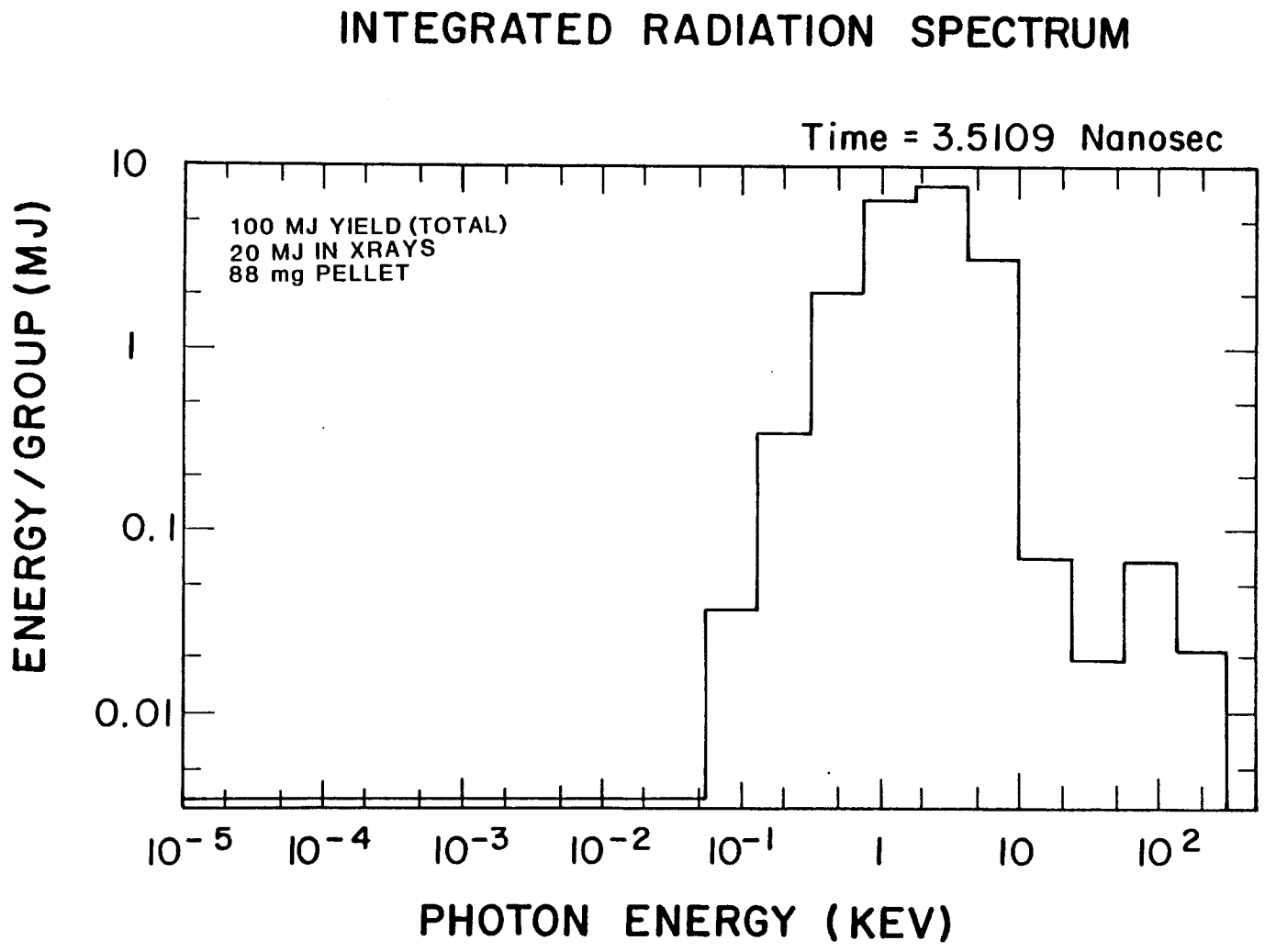

Fig. V-2. The time integrated photon spectrum emitted from an ICF pellet as computed with the PHD code (Ref. 65).

Fluorescence of the gas must also be negligible if the point source model is to be applicable. Fluorescence can occur after an atom ejects a photoelectron and is left in an excited state. The excited atom can undergo radiative electron transitions and emit fluorescent radiation. If, however, the excitation energy that would have appeared as fluorescent radiation is instead transferred to an outer shell electron, then the relaxation process is radiationless. The outer shell electron that is ejected in the radiationless process is referred to as an Auger electron.

The fluorescent yield is a measure of the probability that an excited atom will undergo radiative transitions rather than Auger transitions. The magnitude of the fluorescent yield depends on the energy of the incident x-rays, and also on the atomic number of the gas. Some experimental and theoretical data on the fluorescent yield from transitions to the K shell that was compiled by Burhop[67] is illustrated in Figure V-3. If the incident x-rays are energetic enough to be photoabsorbed by electrons in the K shell, then Figure V-3 can be used to estimate the fluorescent yield. For instance, the spectrum shown in Figure V-2 is energetic enough to interact with the K shell electrons of helium, neon, and argon. Figure V-3 shows that the fluorescent yield from transitions to the K shell will be less than 10% for these gases. The K shell of xenon has a much larger fluorescent yield than the lighter noble gases. But as seen in Figure V-1, x-ray energies on the order of 30 keV are needed to interact with the K shell electrons of xenon. If the x-ray energy is

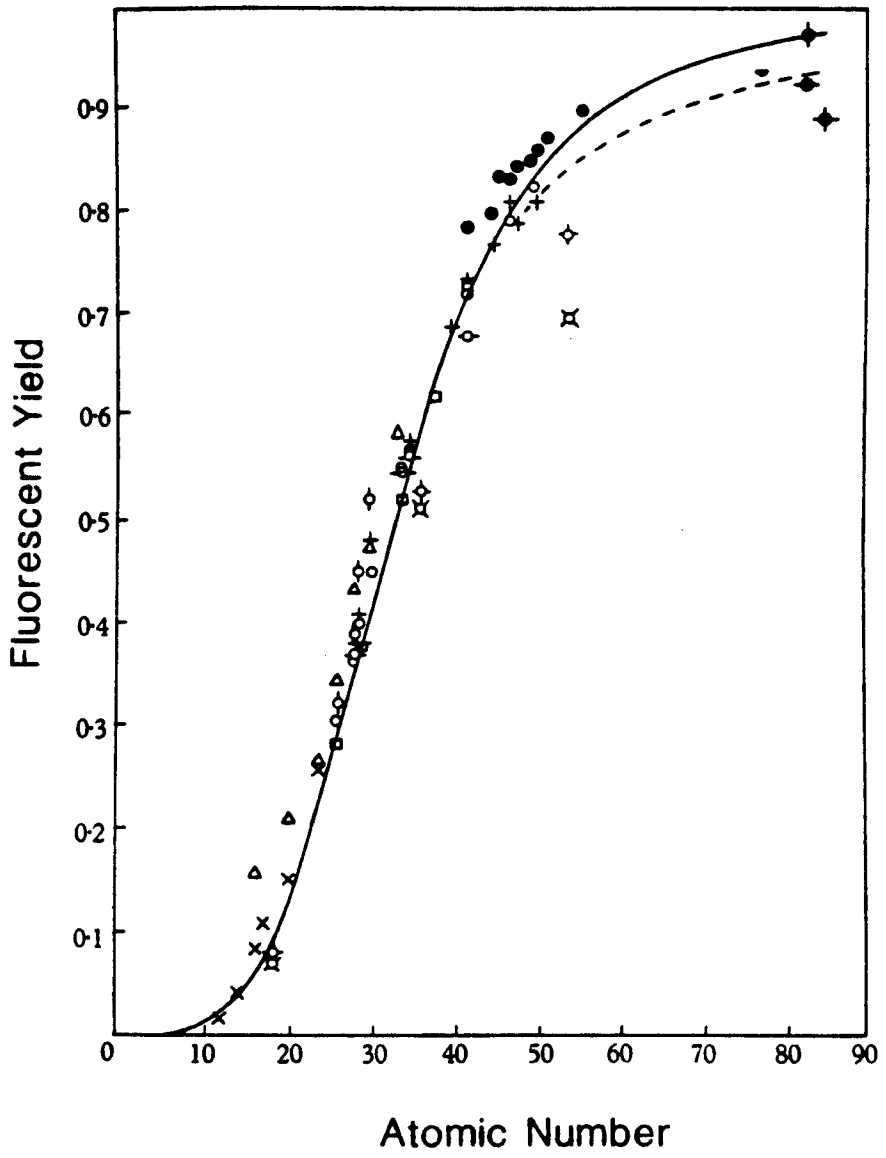

Fig. V-3. The K shell fluorescent yield as a function of atomic number (Ref. 67).
——— non-relativistic theory
----- relativistic theory

less than the K shell binding energy, then the x-rays can only interact with L or M shell electrons. The L series fluorescent yield is much smaller than the K series yield, ranging from 0.05 for krypton up to 0.40 for uranium. The M series fluorescence has not yet been measured accurately, but appears to be less than 0.05 for even the heaviest of elements. Hence, if the target x-rays have energies less than about 30 keV, fluorescence will not be too significant for any buffer gas.

B.2. The Effect of Ionization on the Photoelectric Absorption Coefficient

After a gas atom photoabsorbs a target x-ray, it emits a photoelectron, and as previously indicated, probably one or more Auger electrons. The duration of the x-ray pulse ($\approx 10^{-8}$ s) is much shorter than the time for a photoelectron to slow down and be recaptured ($\approx 10^{-6}$ s), so a deficiency of bound electrons builds up as x-rays are absorbed. The lack of bound electrons, sometimes referred to as x-ray bleaching, causes a reduction in the photoelectric attenuation coefficient that limits the number of x-rays a gas atom can absorb. Near the target, where the x-rays far outnumber the gas atoms, x-ray bleaching has a noticeable influence on the deposition profile.

To model the bleaching effect, the x-ray spectrum will be treated as if it is composed of a number of identical subpulses, with each subpulse having the same fraction of the total x-ray yield. After each subpulse passes through the gas and is exponentially attenuated,

the number of photoelectrons ejected per gas atom can be counted by assuming one electron is ejected per x-ray absorbed. This counting scheme neglects Auger emission, but is adequate for a conservative estimate of the bleaching effect. Before the next subpulse traverses the gas, new attenuation coefficients are computed at each point in space and for each energy group by assuming that each electron in a given atomic shell contributes equally to the photoelectric cross section of that shell. For instance, Figure V-4, shows the attenuation coefficient of argon gas with 0, 4, 8, 12, and 16 electrons missing from the L shell. The corresponding reductions in the attenuation coefficient of neutral argon are 0%, 25%, 50%, 75%, and 100%, respectively. With this model, computing the bleaching effect for x-rays that interact with the L shell electrons is simply a matter of keeping track of the number of electrons left in that shell after every subpulse.

A similar calculation can be made for x-rays that interact with the K shell electrons. However, a question arises as to which shell's electrons will be ejected, because an x-ray with enough energy to be absorbed by a K shell electron might also be absorbed by an L shell electron. Auger transitions occur on a time scale on the order of 10^{-15} s, so an atom that has ejected a photoelectron from the K shell will probably undergo an Auger transition before the next target x-ray is absorbed. Thus, there are never any vacant inner levels until all the outer shell electrons have been removed. After all the outer shell electrons are removed, further ionization reduces the

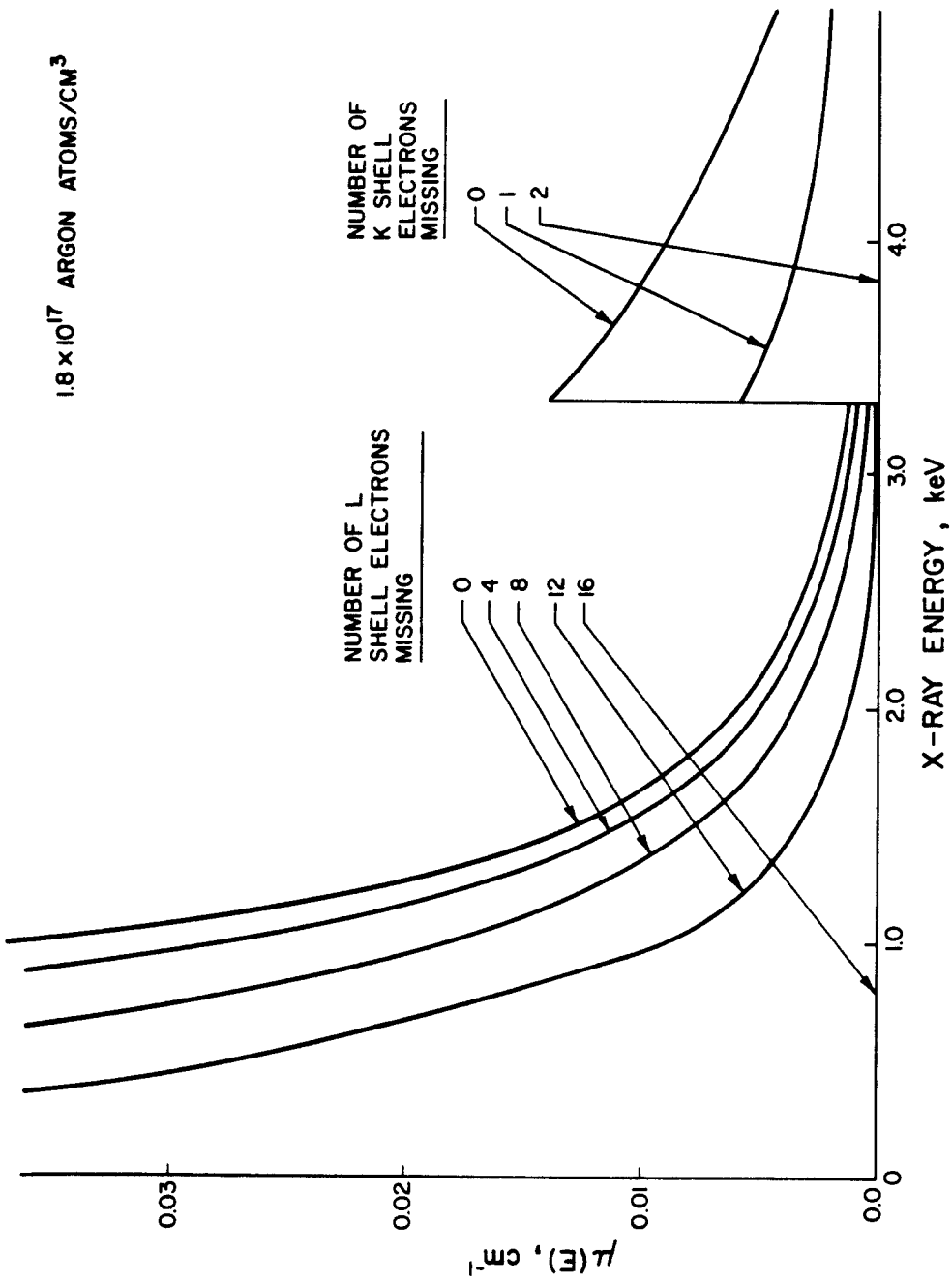

Fig. V-4. The attenuation coefficient of argon gas at various levels of ionization, as predicted by the model proposed here.

attenuation coefficient of the K shell in the manner depicted in Figure V-4.

Figure V-5 shows the specific energy profile in argon gas after 60 MJ are emitted from a 0.3 keV blackbody point source of x-rays. The two curves correspond to the specific energy computed with and without taking into account the x-ray bleaching effect, and represent the same total deposited energy. When the bleaching effect is ignored, the specific energy computed near the source decreases rapidly as the distance from the source increases. But when the reduction in the attenuation coefficient is included using the model described above, the specific energy has an almost constant value for the first 50 cm.

After the photoelectrons have thermalized with the gas ions, the gas temperature can be computed. If the transport of energy is negligible on a macroscopic scale during the equilibration period, then the x-ray energy deposition profile can be used directly to compute the gas temperature, charge state, pressure, and radiation mean free paths that are necessary to begin the radiation hydrodynamic calculation. Including the x-ray bleaching effect helps to avoid unrealistically large temperature gradients near the pellet, and thereby decreases the computer time required to solve the radiation hydrodynamics equations.

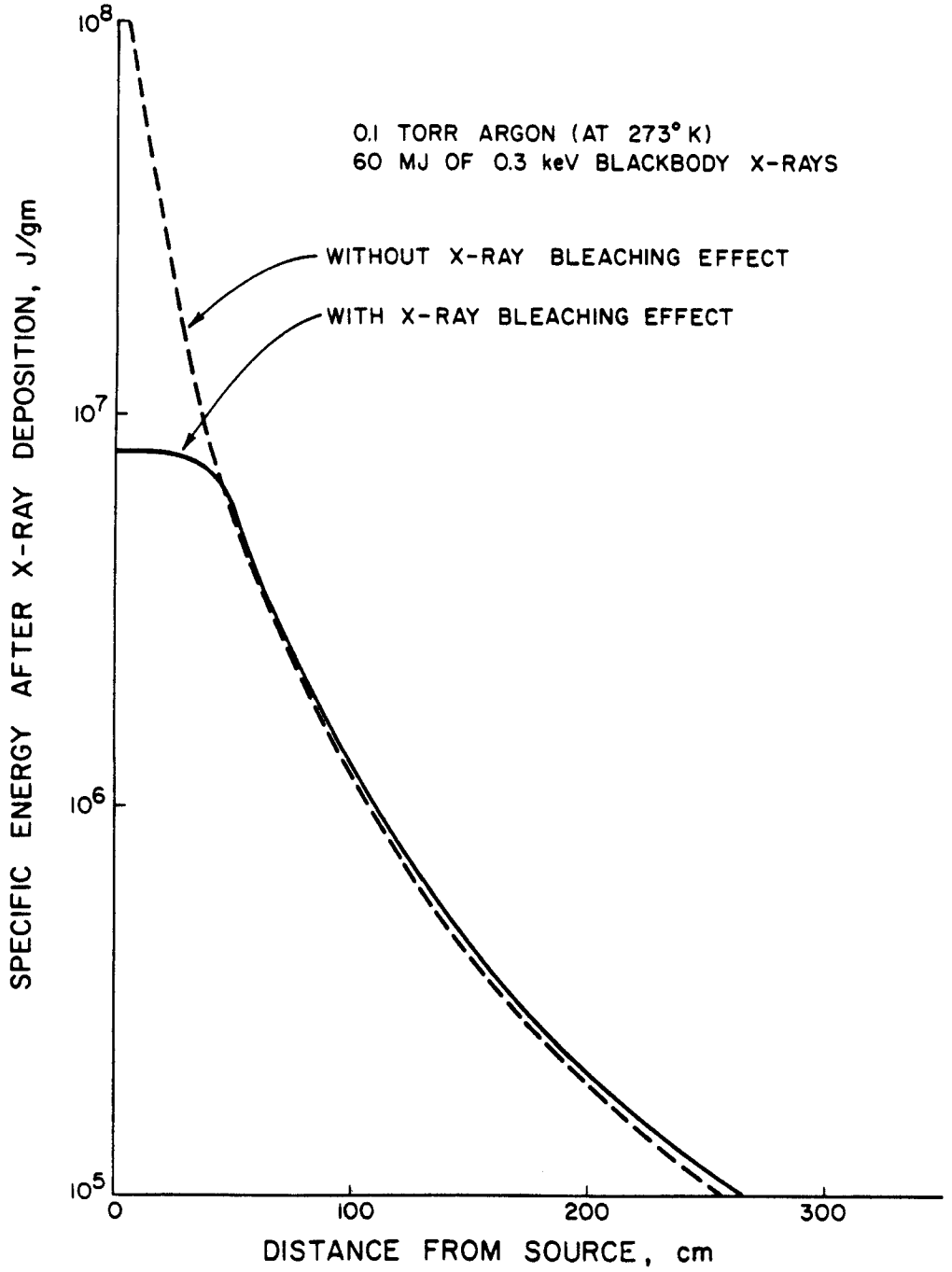

Fig. V-5. Specific energy profile after x-ray deposition in argon gas, with and without the bleaching effect.

C. The Deposition of Target Debris

C.1. The Path of Debris Ions Slowing Down in an Incompressible Gas

Figure V-6 shows two different paths that a debris ion might travel after entering an incompressible gas at point O. If the ion interacts only with electrons of the gas atoms, then it will slow down along the straight path OR_p. The path is straight because the mass of an electron is much smaller than the mass of a debris ion, so deflections of the ion are small. For a straight line trajectory, u_d is equal to u_{dr}, and the driving terms to the radiation hydrodynamic equations can be computed from slowing down models.[68] On the other hand, if an ion loses most of its energy in elastic collisions with the gas nuclei, then the trajectory will follow the path OR. The driving terms are much more difficult to compute when nuclear collisions are influential, because each ion follows a different path.

Bohr[69] has suggested that nuclear stopping is dominant if the ion speed is less than about one-tenth the speed of the electrons orbiting the ion. Using the Thomas-Fermi[70] model, the average speed of an orbiting electron, u_e, is

$$u_e = Z_1^{2/3} \frac{2\pi e^2}{h} \quad , \tag{69}$$

where: Z_1 is the atomic number of the ion,

e is the electron charge in esu,

h is Planck's constant in cgs units.

Curves corresponding to u_e and $0.1\ u_e$ are shown in Figure V-7 to

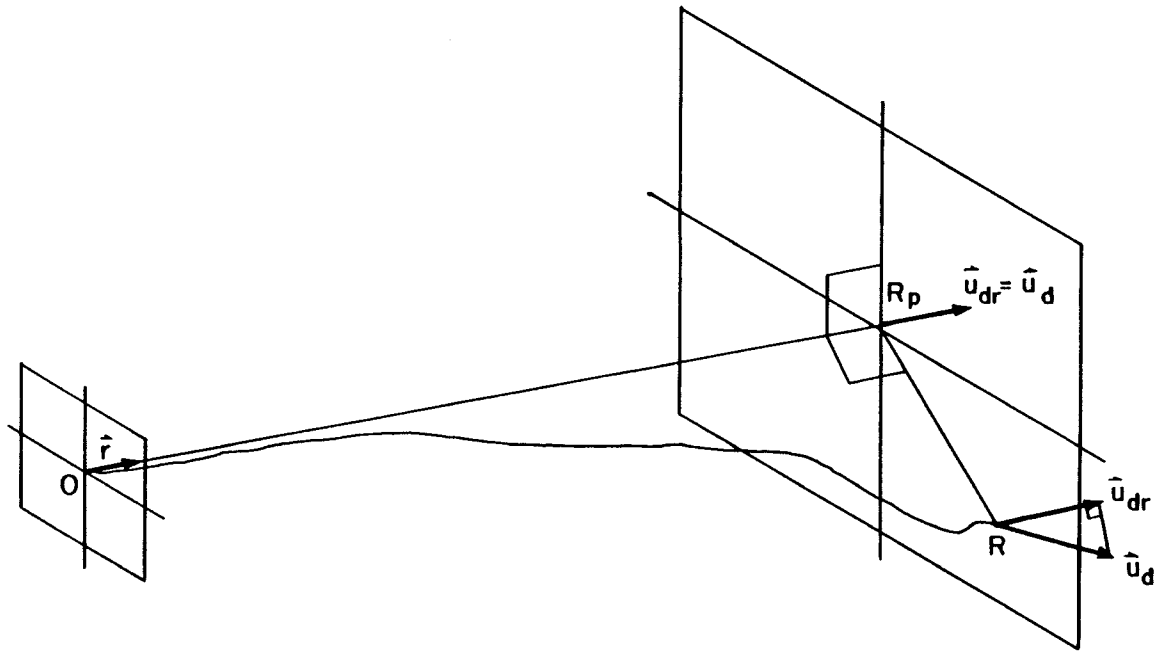

Fig. V-6. The trajectory of an ion entering an incompressible gas at point O. The curve OR is the trajectory of an ion slowing down mainly by collisions with gas nuclei. The straight line OR_p is the trajectory of an ion slowing down primarily by interactions with electrons.

illustrate the parameters where electronic or nuclear stopping will dominate. These curves are only rough guidelines, but suitable for order of magnitude estimates.

To estimate whether the dominant slowing down mechanism for target debris traversing a buffer is nuclear or electronic interactions, the kinetic energy per atomic mass unit can be assumed to be initially equal for each debris ion. Hence, all of the target ions have the same initial speed. Given this assumption, the initial speed of each ion can be computed from the fraction of the yield in debris energy and the number of debris ions. From Figure V-7 and this estimate of the initial speed, it follows that for a target constructed from materials with an average atomic number greater than about ten, the ratio of debris energy to mass must be greater than 3000 MJ/gm for electronic interactions to dominate. It is not likely that this condition will be met by ICF targets, so it is concluded that nuclear collisions will be the important slowing down mechanism. Hence, the trajectory of the ions will not be straight as they traverse the gas.

C.2. The Slowing Down of Debris Ions in an Incompressible Gas

An inexpensive method of computing u_d, u_{dr}, and the time derivative of these quantities for target debris slowing down in a cavity gas will now be described. The gas will be considered stationary while discussing the method, with the effects of compressibility added in Section C.4.

Using the Boltzmann equation, Williams[71] has developed a transport equation for the distribution function of an initially

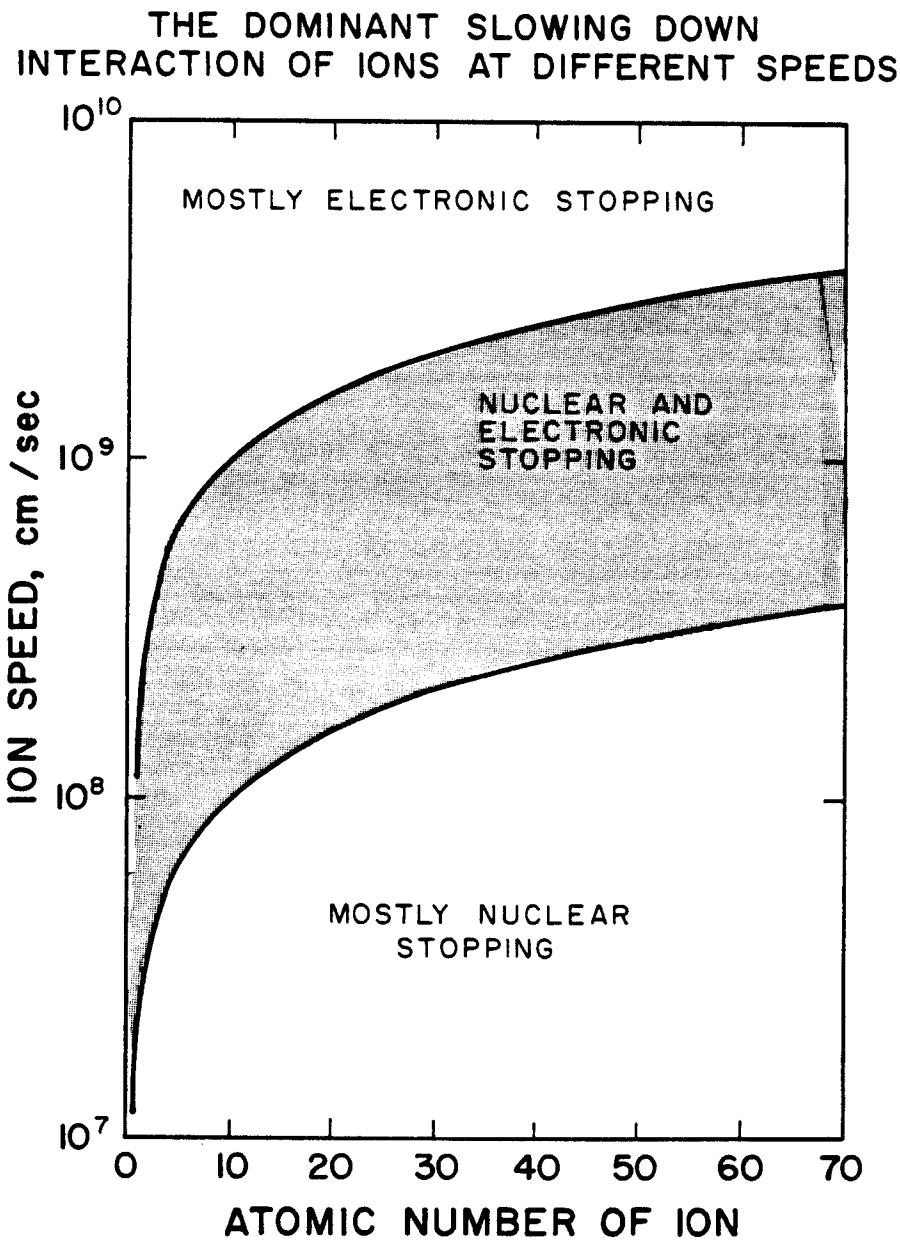

Fig. V-7. The dominant slowing down interaction of ions based on the Thomas-Fermi model.

monoenergetic ion pulse as a function of time, space, and energy in the slowing down medium. Although a few analytic solutions to the ion transport equation exist for simplified interaction potentials,[71,72] even a numerical solution is exceedingly difficult when realistic interaction potentials are used. Lindhard[73] derived a more manageable expression that describes the spatial distribution as a function of energy, with the time dependence neglected. That intergro-differential equation was developed using heuristic statistical arguments, but Williams[71] later showed how it can be derived from the adjoint of the time dependent ion transport equation. Other arguments supporting the derivation of Lindhard's equation have also been refined since it was first derived,[74] and it is still the cornerstone of ion transport calculations.

In Lindhard's classic work it was shown how the first spatial moment of the intergro-differential equation leads to a simpler integral equation for the average path length, R, as a function of energy. A second moment leads to another integral equation describing the straggling (i.e., standard deviation) in R as a function of energy. Other moments of Lindhard's equation lead to integral equations for the average projected range, R_p, and the straggling in R_p, both as functions of energy. It was also illustrated how the integral equations for R, R_p, and the straggling in these quantities can be solved by expanding the integrands as a power series, and retaining the lower order terms. Brice[75] has further developed Lindhard's expansion of the integrands, and has written the RASE4[76]

code to solve for the ranges and standard deviations. These quantities are computed by RASE4 when the initially monoenergetic ions have slowed down to the speed u_d, but no information is given about the time it takes the ions to slow down to u_d, or the standard deviation in that time. The information concerning the time has been sacrificed by taking Lindhard's approach instead of solving a time dependent ion transport equation. The approach taken here will be to add the time dependence in an approximate manner to the results computed by the RASE4 code.

The path length, R, projected range, R_p, and speeds u_d and u_{dr} are stochastic quantities that have some standard deviation associated with them at any given time. Oen and Robinson[77] used the nuclear and electronic cross sections developed by Lindhard[78] to compute the standard deviation in the slowing down time, and found that it is always less than 15% of the average slowing down time. This result indicates the ion speed is fairly precisely defined at any given time as the ions slow down. The time derivative of u_d can then be approximated with a total derivative instead of a partial derivative. If R and R_p are defined as the average path length and average projected range, respectively, then the slowing down of ions in an initially monoenergetic pulse can be defined as

$$\frac{du_d}{dt} = \frac{du_d}{dt}\frac{dR}{dR} \quad , \tag{70}$$

$$= u_d \frac{du_d}{dR} \frac{dR_p}{dR_p} \quad , \tag{71}$$

$$= u_d \frac{du_d}{dR_p} \frac{dR_p}{dR} \quad . \tag{72}$$

The motivation for writing the time derivative of u_d in the form of Equation (72) is that the three terms on the right-hand side are provided by RASE4 as a function of R_p. The ion speed at any instant is given by a time integration of Equation (72).

The average projected speed of an ion pulse, u_{dr}, is defined in a similar manner,

$$u_{dr} = \frac{dR_p}{dt} \frac{dR}{dR} \quad , \tag{73}$$

$$= u_d \frac{dR_p}{dR} \quad . \tag{74}$$

Like Equation (72), Equation (74) is exact for a single ion, but applies only in an average sense to the ions in an initially monoenergetic pulse. Differentiating Equation (74) yields another quantity required for the driving terms,

$$\frac{du_{dr}}{dt} = \frac{du_d}{dt} \frac{dR_p}{dR} + u_d \frac{d}{dt} \left(\frac{dR_p}{dR}\right) \quad . \tag{75}$$

$$= \frac{du_d}{dt} \frac{dR_p}{dR} + u_d^2 \frac{d^2R_p}{dR^2} \quad . \tag{76}$$

Each term on the right of Equation (76) can be evaluated using the RASE4 results.

To evaluate Equations (72), (74), and (76), the RASE4 results have been fit to convenient analytical functions. The functional fit for the debris speed, $u_d(R_p)$, that was developed during this research is

$$u_d(R_p) = u_{d*} \sqrt{1 - \left(\frac{R_p}{R_{p*}}\right)^{c_1}} \quad , \tag{77}$$

where R_{p*} is the final average projected range of ions that began with an initial speed u_{d*}. The constant c_1 is evaluated by substituting in an intermediate value of u_d and R_p from the RASE4 output, along with the corresponding value of u_{d*} and R_{p*}. Once the value of c_1 is known, Equation (77) can be used for each energy group of an arbitrary spectrum of debris ions. Only the initial speed and the final range of the ions in each group need be known. Figure V-8 shows how Equation (77) fits the RASE4 results for 10, 20, and 30 keV iron ions slowing down in 10^{-5} atm. of argon. The derivative, du_d/dR_p is also required in Equation (72), and is readily computed from Equation (77).

The analytic expression developed during this research for $R_p(R)$ is

$$R = R_p \exp(c_3 R_p^{c_2}) \quad . \tag{78}$$

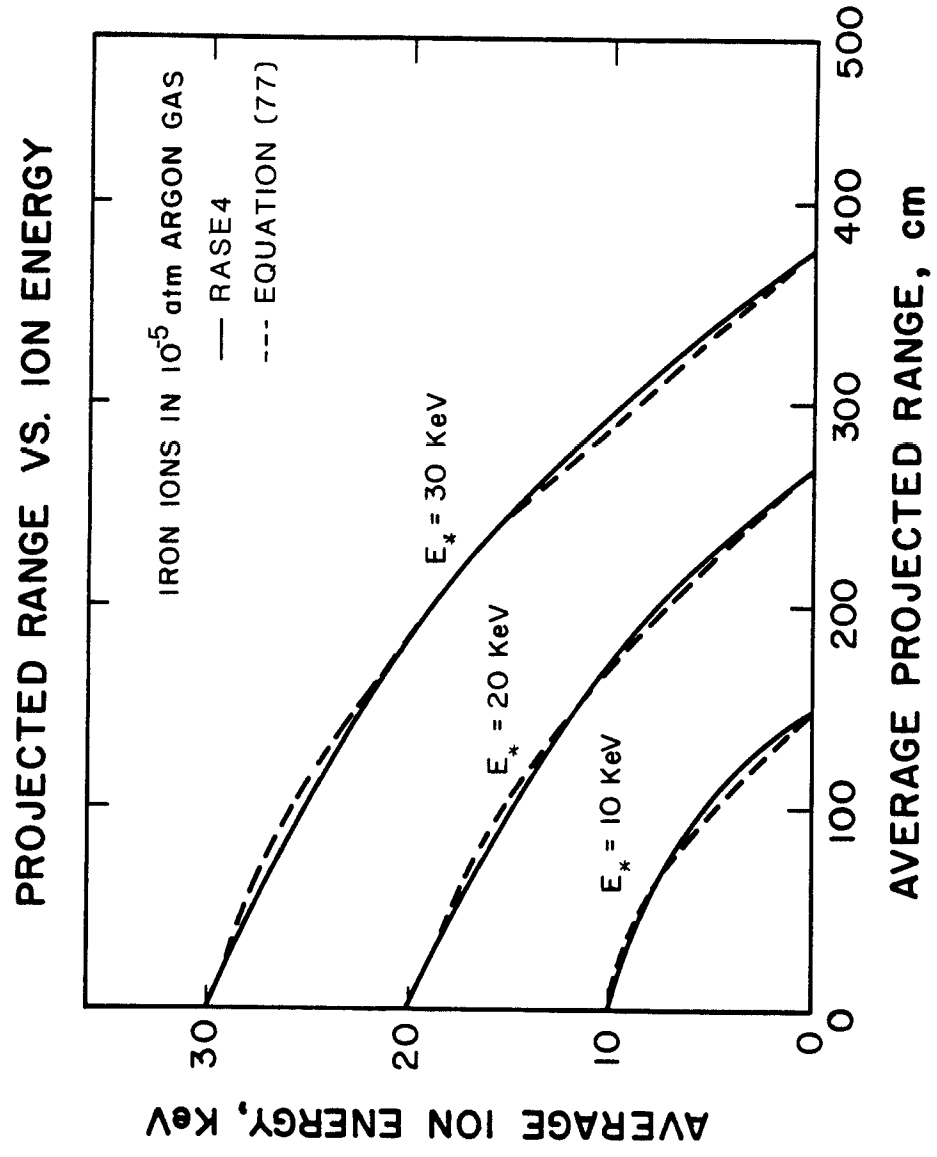

Fig. V-8. The energy of an ion pulse as a function of the average projected range for three different initial energies.

A value of the path length, R, corresponding to the intermediate speed used in evaluating $\dot{c}_1$, and a value of the final path length, R_*, from RASE4 are needed to evaluate the constants c_2 and c_3. Solving for c_2 and $\ddot{c}_3$ yields

$$\dot{c}_2 = \frac{1}{\ln \frac{R_p}{R_{p*}}} \ln \left[\frac{\ln \frac{R}{R_*}}{\ln \frac{R_*}{R_{p*}}} \right] , \tag{79}$$

and

$$\ddot{c}_3 = \frac{1}{\dot{c}_2 R_{p*}^{\dot{c}_2}} \ln \frac{R_*}{R_{p*}} . \tag{80}$$

The derivative of $R_p(R)$ is needed in the driving terms, and is obtained by differentiating Equation (78),

$$\frac{dR_p}{dR} = \frac{1}{\exp(\ddot{c}_3 R_p^{\dot{c}_2})(1 + \dot{c}_2 \ddot{c}_3 R_p^{\dot{c}_2})} \tag{81}$$

Equation (81) is compared with the RASE4 output in Figure V-9. Differentiating Equation (81) yields another quantity needed to evaluate the driving terms,

$$\frac{d^2 R_p}{dR^2} = - \frac{R_p^{\dot{c}_2 - 1} \dot{c}_2 \ddot{c}_3 (1 + \dot{c}_2 \ddot{c}_3 R_p^{\dot{c}_2} + \dot{c}_2) \exp(\ddot{c}_3 R_p^{\dot{c}_2})}{[\exp(\ddot{c}_3 R_p^{\dot{c}_2})(1 + \dot{c}_2 \ddot{c}_3 R_p^{\dot{c}_2})]^3} . \tag{82}$$

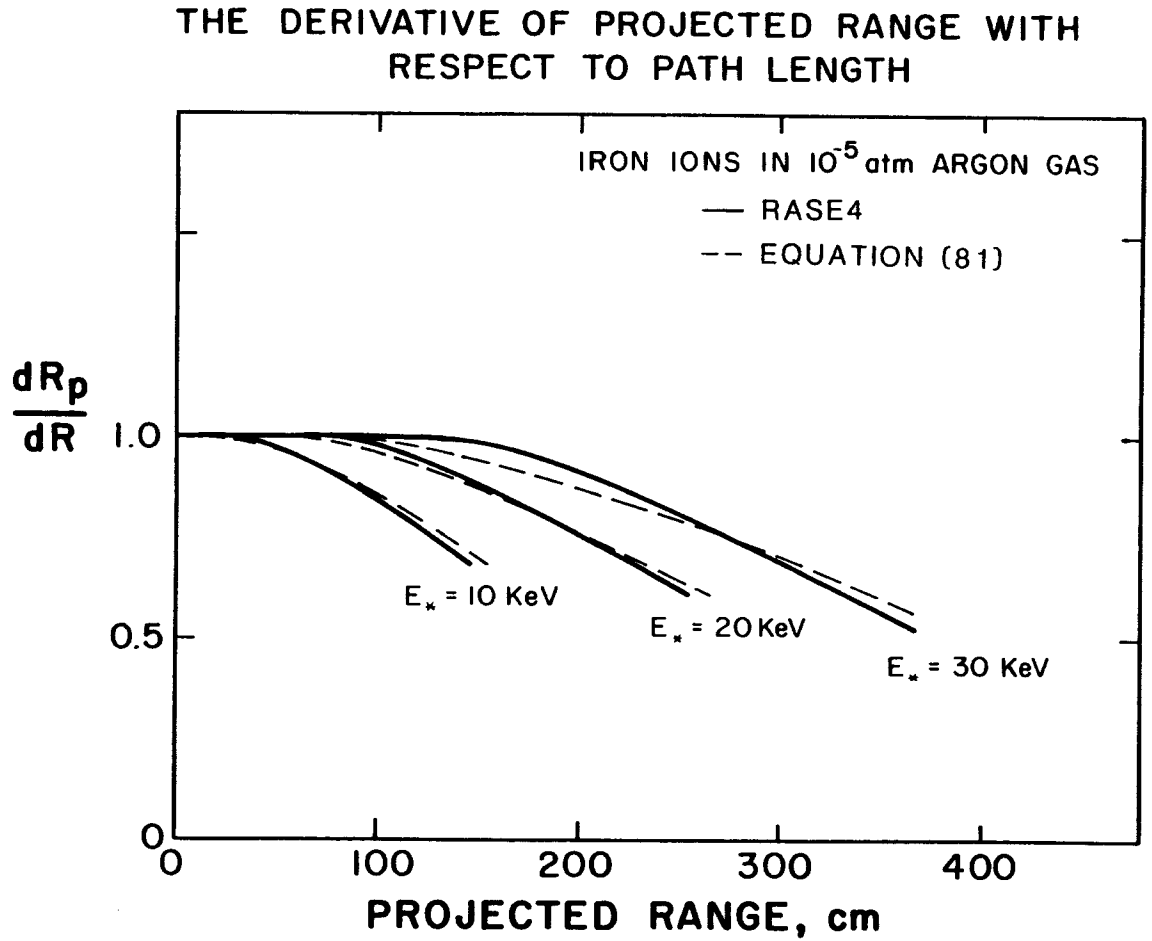

Fig. V-9. The change in projected range with respect to path length as a function of projected range for three different initial energies.

Six parameters from the RASE4 results are used in evaluating the constants, c_1, c_2, and c_3. Equation (77) also requires values of the final projected range, R_{p*}, for each energy group in a debris spectrum. However, R_{p*} can be evaluated from the initial speed, u_{d*}, using an expression suggested by Hunter[66],

$$R_{p*} = c_4 u_{d*}^{c_5} \quad . \tag{83}$$

The constants c_4 and c_5 are evaluated using another value of u_{d*} and R_{p*}, bringing the number of parameters used from the RASE4 results up to eight.

C.3. The Spatial Distribution of Ions Slowing Down in an Incompressible Gas

The linear density (gm/cm) of ions in an initially monoenergetic pulse becomes Gaussian after the ions have undergone many collisions with the gas nuclei. The volumetric debris density, ρ_d, is obtained by multiplying the linear density by a factor that accounts for divergence of the ions:

$$\rho_d(r,R_p,\sigma) = M_d \, c \exp\left(-\frac{1}{2}\left(\frac{r - R_p}{\sigma}\right)^2\right)\left[\frac{1}{Gr^{\delta-1}}\right] \quad , \tag{84}$$

where: $G = 1$ for $\delta = 1$ (cartesian),

$= 2\pi$ for $\delta = 2$ (cylindrical),

$= 4\pi$ for $\delta = 3$ (spherical).

σ is the standard deviation in the projected range R_p, and M_d is the

total mass of the debris. The normalization factor, c, is computed so as to conserve debris mass in a semi-infinite medium:

$$1 = c \int_0^\infty \exp\left(-\frac{1}{2}\left(\frac{r - R_p}{\sigma}\right)^2\right) dr \ , \tag{85}$$

or

$$c = \frac{1}{\sigma}\sqrt{\frac{2}{\pi}} \frac{1}{1 + \operatorname{erf}\left(\frac{R_p}{\sqrt{2}\sigma}\right)} \ . \tag{86}$$

The average debris density in each Lagrangian zone, $\rho_{d,j+1/2}$, is needed to evaluate the driving terms by finite difference methods. Integrating Equation (86) between zone boundaries r_j and r_{j+1}, and dividing by the factor that accounts for divergence, $VOL_{j+1/2}$, results in

$$\rho_{d,j+1/2} = \frac{M_d}{VOL_{j+1/2}} \left[\frac{\operatorname{erf}\left(\frac{r_{j+1} - R_p}{\sqrt{2}\sigma}\right) - \operatorname{erf}\left(\frac{r_j - R_p}{\sqrt{2}\sigma}\right)}{1 + \operatorname{erf}\left(\frac{R_p}{\sqrt{2}\sigma}\right)}\right] \ . \tag{87}$$

The error functions in Equation (87) can be evaluated numerically using rational approximations.[79]

The three independent variables appearing in the equation for ρ_d can be reduced to two by relating σ to R_p. The relation developed for this is

$$\sigma(R_p) = \sigma(R_{p*}) \frac{R_p \exp(c_6 R_p)}{R_{p*} \exp(c_6 R_{p*})} \cdot \tag{88}$$

The standard deviation at the end of range, $\sigma(R_{p*})$, is needed in Equation (88). It can be computed from the initial speed using a relation proposed by Hunter,[66]

$$\sigma(R_{p*}) = c_7 R_{p*} \exp(- c_8 u_{d*}) \cdot \tag{89}$$

To evaluate the constants c_7 and c_8, only one more parameter from the RASE4 results is required, and that is a value of $\sigma(R_{p*})$ corresponding to the initial speed u_{d*}. Evauating c_6 requires yet another parameter from the RASE4 results, and that is a value of the standard deviation at some intermediate position, $\sigma(R_p)$. Equations (88) and (89) were used to compute the standard deviations in Figure V-10, and are compared to the RASE4 results.

Figure V-11 illustrates the application of the ion transport model described in this section. A pulse of initially monoenergetic iron ions that have entered a slab of stationary argon gas with a density corresponding to 0.028 atmospheres at standard temperature was used in this example. The initial energy of the ions is 20 keV. The spatial distribution when the ions have slowed down to 10, 5, and 0 keV was reconstructed using Equation (72) to estimate the slowing down at time t_n from the average projected range at t_{n-1}. Integrating Equation (76) over the time step gives the radial speed, and a

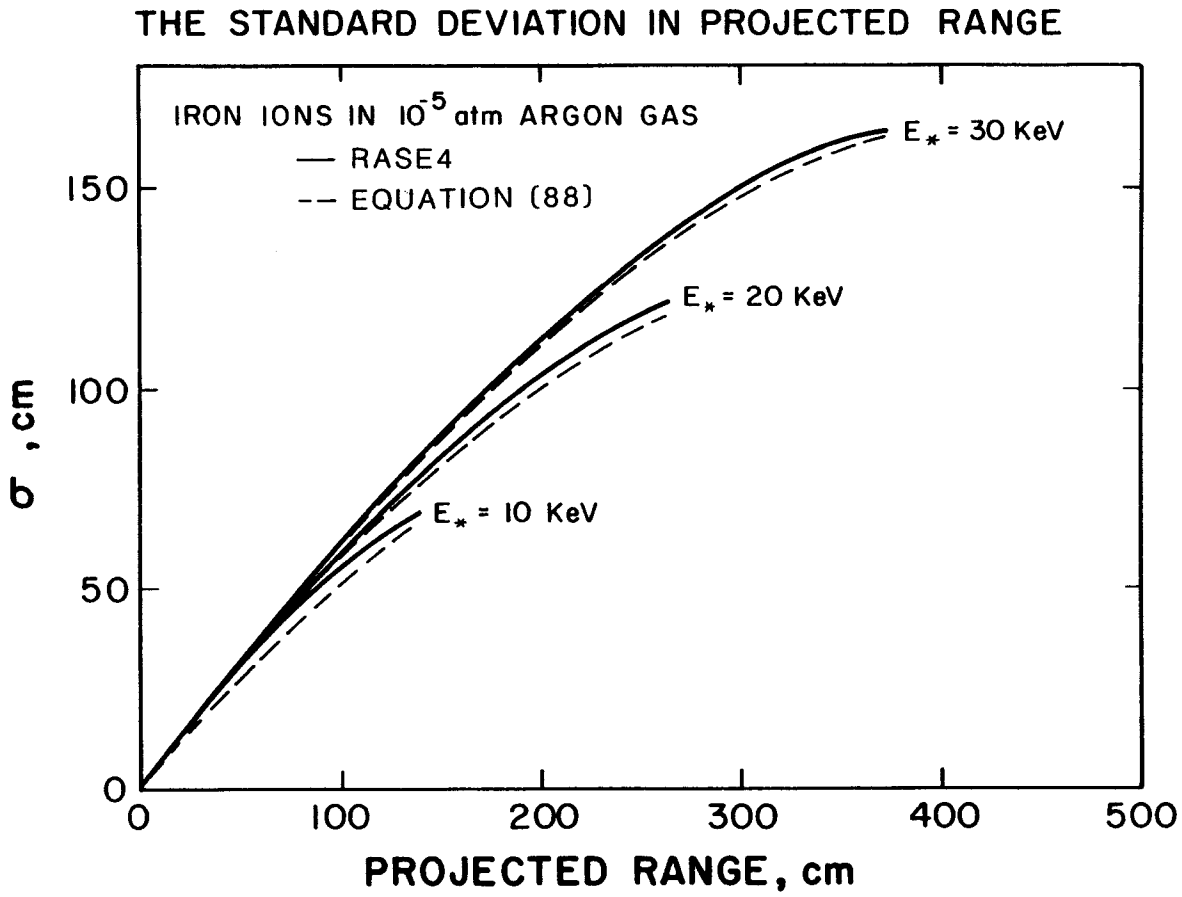

Fig. V-10. The standard deviation in projected range as a function of projected range for three different initial energies.

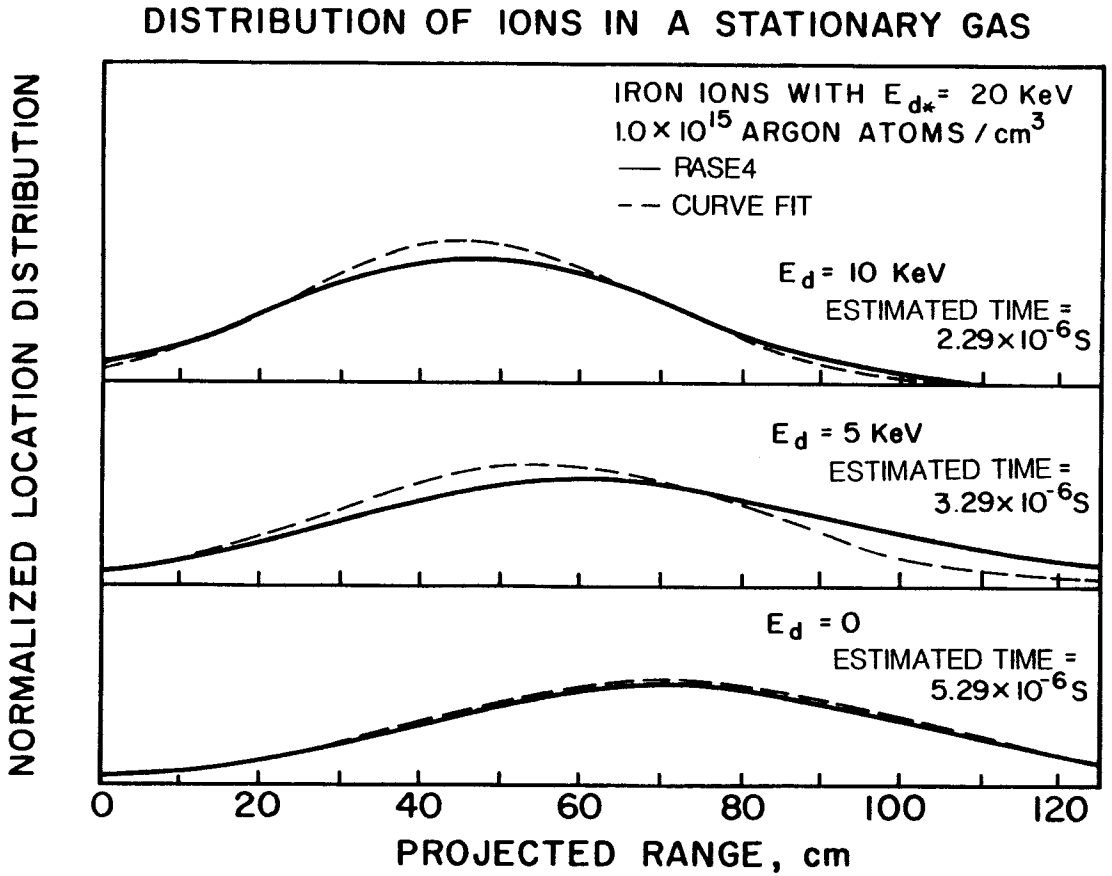

Fig. V-11. The spatial distribution of a pulse of 20 keV iron ions when the ions have slowed to 10 keV, 5 keV, and 0 keV. The gas is 0.028 torr (0°C) argon.

second integration gives the average projected range at t_n. The spatial distribution follows from Equation (87) and (88). The procedure begins anew as the average projected range at t_n is then used to compute the slowing down at t_{n+1}. The time for the ions to slow down to 10, 5, and 0 keV was recorded during the time integration, and is shown in Figure V-11.

C.4. The Energy and Momentum Deposition Model Extended to a Compressible Gas

The scheme for computing the energy and momentum deposition rates from target debris can easily be modified to account for hydrodynamic motion of the gas if it is assumed that the speed of the gas is much smaller than the speed of the debris. Given this condition, the slowing down of ions in a deforming gas is equal to that of ions slowing down in a stationary gas when the debris has traversed an equal number of gas atom layers. To apply the equations developed in Sections C.2 and C.3 to a deforming gas, the projected range of ions slowing down in a deforming gas must be related to the projected range of ions slowing down in a stationary gas when an equal number of atom layers have been traversed. Figure V-12.a shows the average projected range of an ion pulse traversing stationary Lagrangian zones, and Figure V-12.b shows the same pulse and zones when hydrodynamic motion is included. Equating the atom layers traversed, the projected ranges are related by the expression

$$R_p = r_j + (r_{j+1} - r_j) \frac{R'_p - r'_j}{r'_{j+1} - r'_j} \quad . \tag{90}$$

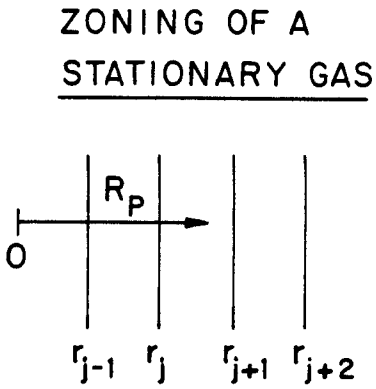

Fig. V-12.a. The average projected range of an ion pulse slowing down in a stationary gas.

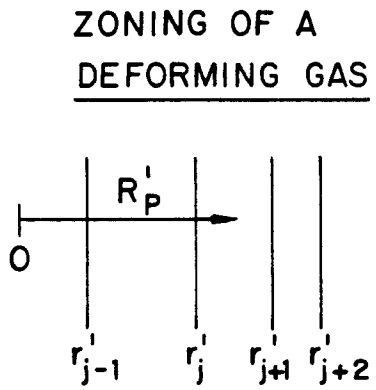

Fig. V-12.b. The average projected range of an ion pulse slowing down in a deforming gas.

The positions of the primed zone boundaries are computed from the equation of gas motion, and the positions of the stationary boundaries are known from initial conditions. The average projected range in the deforming coordinate system, R_p', follows from the equation of debris motion. To evaluate the slowing down, the value of R_p computed by Equation (90) is used in the fitting functions.

In some instances, the radial speed of the deforming gas may be comparable to that of the debris, in which case the energy and momentum deposition model described in Sections C.2 and C.3 cannot be readily extrapolated to a deforming gas. This occurs when the expanding debris pushes the gas out like a spherically expanding piston rather than streaming through. As the gas is accelerated to speeds comparable to the debris speed, the rate that internal energy and momentum are transferred approaches zero. To insure that these rates approach zero in the model used here, the accelerations computed by Equations (72) and (76) are multiplied by $(u_{dr} - u)/u_{dr}$, which approaches unity for $u_{dr} \gg u$, and zero for $u_{dr} \approx u$.

CHAPTER VI

NUMERICAL SOLUTIONS TO THE TWO TEMPERATURE EQUATIONS

The FIRE code solves the equations of radiation hydrodynamics that were described in the previous chapter. The original version of the FIRE code has been modified as part of this thesis work. The modifications include modeling the radiation field as a dilute Planckian, as described in Chapter IV, and adding the driving terms from target x-ray and debris, as described in Chapter V. Figure VI-1 indicates how the effort put forth for this thesis was part of a larger effort to analyze the response of an ICF first wall in a systematic fashion. The parameters that are input into the FIRE code to describe the target x-ray and debris spectrum are provided by a target analysis code, and the equation of state and opacity data is provided by an atomic physics code. The output of the FIRE code is used by other codes that determine the thermal response, stress history, and first wall lifetime.

A brief introduction to the code that provides the opacity and equation of state data, MIXER, is given in Section A. This data is the weakest link in the solution of the radiation hydrodynamic equations because the data is computed from theory, and usually cannot be verified by experiment. In Section A the mean free paths computed by the MIXER code are compared to those computed by another computer code, and the discrepancies between the results of the two codes are discussed.

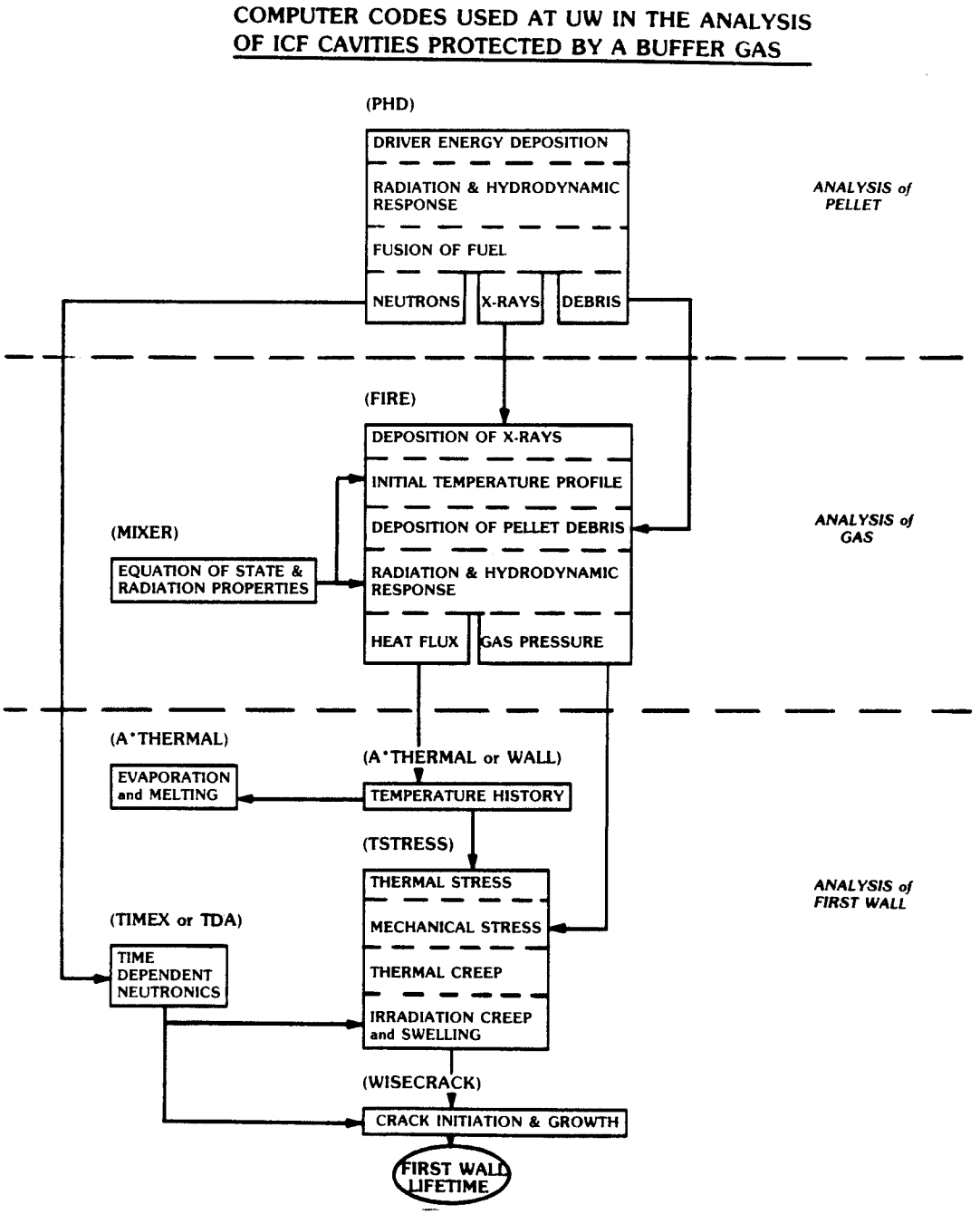

Fig. VI-1. A block diagram showing the relationships between computer codes used in ICF reactor design at the University of Wisconsin.

Some applications of the FIRE code are given in Section B. The parameter studies that were conducted show how the gas response varies with the ambient gas density, gas type, target yield, and Lagrangian mesh. In some instances, the results from the FIRE code are compared with the results from an analytic description of the gas response, and the discrepancies are discussed.

A. The FIRE Code and Its Input

The original verison of the FIRE code was written by Moses and Peterson.[1] In that version, the equations of radiation transport are solved numerically using a fully implicit finite difference scheme that guarantees unconditional stability. The equations are solved for a Lagrangian mesh, which eliminates mass and momentum transport across zone boundaries. Most of the programming in the original version has been retained in the version that was developed as part of this thesis. The programming details of the new version of the FIRE code are documented elsewhere,[80] and will not be considered here.

The ionization is provided as a function of temperature and density by the MIXER code.[35] The MIXER code uses either the Saha[49] or Coronal[81] equilibrium model to compute the ionization. The Saha model assumes collisional ionization is balanced by collisional recombination, and the Coronal model assumes collisional ionization is balanced by radiative recombination. The MIXER code automatically determines which model will be used at a given temperature and density. In general, the Saha model applies at lower

temperatures and greater densities than the Coronal model. Both of these models are consistent with the assumption of local thermodynamic equilibrium that was described in Chapter IV.

The MIXER code also provides the Planck and Rosseland mean free paths as a function of gas temperature, density, and radiation temperature. These mean free paths are arrived at by first computing the frequency dependent mean free path from the photo-ionization, inverse Bremsstrahlung, line absorption, and Thompson scattering cross sections. The frequency dependent mean free path is then integrated in the manner described in Chapter IV to arrive at the Planck and Rosseland mean free paths. Although there is very little experimental opacity data at the temperatures of interest to compare with the MIXER code calculations, these calculations can be compared to the calculations of other computer codes. Such a comparison will at least verify some consistency between computer codes. Figure VI-2 compares the equilibrium Planck and Rosseland mean free paths of argon from the MIXER code with those computed by a physics group at Los Alamos. The Planck mean free paths agree as well as can be expected for independently developed codes. However, the Rosseland mean free paths differ by orders of magnitude at temperatures below about 10 eV. This disagreement may be due to large increases in the line absorption cross section that occur over narrow frequency intervals. As seen by examining the definitions in Chapter IV, the integral that defines the Planck mean free path is insensitive to line absorption, whereas the integral that defines the Rosseland mean free

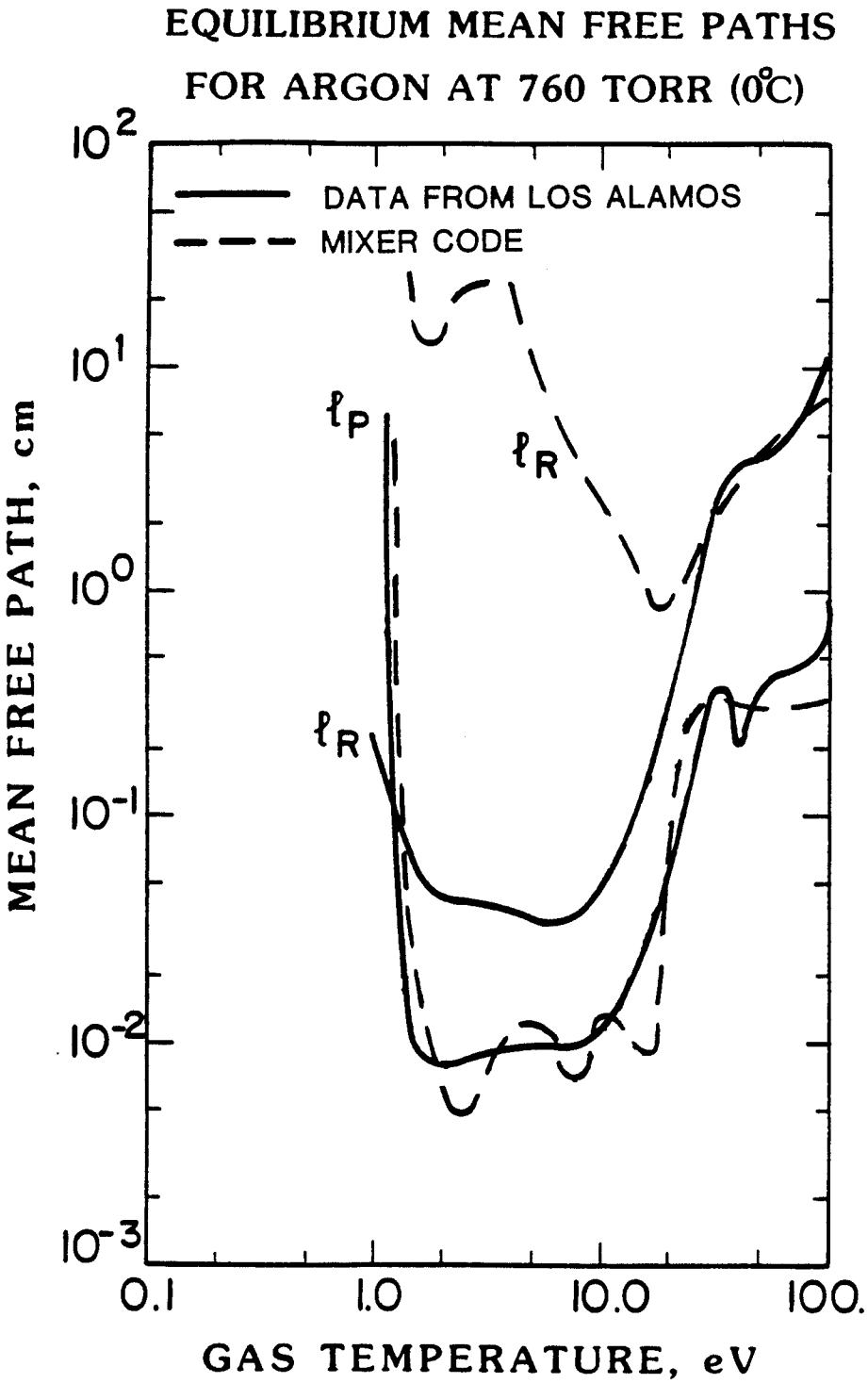

Fig. VI-2. The equilibrium Planck and Rosseland mean free paths of argon. The curves from Los Alamos were computed for the author by the Theoretical Physics Group, T-4.

path can be very sensitive to line absorption. Accepting this explanation for the discrepancy, then the Rosseland mean free path that was computed by the Los Alamos group is probably more accurate than the MIXER code calculations, because the large computers at Los Alamos are capable of integrating over the lines more carefully than the smaller computers for which the MIXER code was designed. Efforts to improve the MIXER results are currently underway by the authors of that code.

In order to compute the attenuation of target x-rays in the buffer gas, a library of x-ray attenuation coefficients must be provided to the FIRE code. A library based on the work of Biggs and Lighthill[82,83] and arranged for computer access by Adams and Biggs[84] is used in this thesis. The library includes the photoelectric absorption, incoherent scattering, and coherent scattering interactions.

B. Applications of the FIRE Code

Simulations of the buffer gas response in a 4.12 meter spherical cavity are presented in this section. In all of the examples that are discussed, fifteen percent of the target yield was assumed to be released in the kinetic energy of one gram of iron target debris. The initial energy spectrum of the iron ions was assumed to be monoenergetic, and other constitutents of the debris such as unburnt fuel and fusion by-products were ignored. Another 15% of the yield was assumed to appear as x-rays emitted by the target. The frequency spectrum of the x-rays was assumed to be that of a 0.3 keV blackbody,

and a pulse duration of 10^{-8} seconds was used. The remainder of the target yield consists of energetic neutrons, whose interaction with the cavity gas was ignored. A 100 MJ yield was assumed for all of the examples, except those in Section B.3, where the target yield was varied.

B.1. The Influence of the Ambient Gas Density on the Gas Response

In this subsection, the response of a buffer gas to a target explosion is described for gas densities varying over four orders of magnitude. The ambient gas densities used in these examples correspond to 50, 5, 0.5, and 0.05 torr at standard temperature (0°C). The equations of state used are for argon mixed with two volume percent sodium. This mixture was choosen because it might be plausible to ignite the target using beams of light ions that propagate through ionized channels in the gas.(85) The ionized channels are created by a laser, and the sodium helps to decrease the required laser energy.(86) The results of the FIRE code calculations show that for this range of densities, all of the kinetic energy of the debris is attenuated by the gas. The FIRE code results also indicate that virtually all of the x-ray energy is attenuated by the 50 and 5 torr gas, but only 11.7 MJ is deposited into the 0.5 torr gas, and only 4.9 MJ is deposited into the 0.05 torr gas. Of course, x-rays unattenuated by the gas are absorbed in the first few microns of first wall material.

Table VI-1 shows the pressure from shock reflection at the wall that was computed by the FIRE code for the four gas densities of

Table VI-1. A Comparison Between the Peak Pressure Computed at the Wall by the FIRE Code and an Analytic Estimate

Ambient Density, Torr*	Ambient Pressure, J/cm^3	Deposited Energy, MJ	Analytic Estimate		Fire Code
			Shock Pressure, J/cm^3	Reflected Pressure, J/cm^3	Reflected Pressure, J/cm^3
50	1.42×10^{-2}	30	0.10	0.40	0.38
5.0	1.42×10^{-2}	30	0.10	0.59	0.04
0.5	1.42×10^{-2}	26.7	0.09	0.55	0.01
0.05	1.42×10^{-2}	20	0.07	0.42	0.05

*At standard temperature.

interest. Also listed is an analytic estimate of the pressure at the shock front when the shock reaches the wall. Jones' expression for the pressure increase at a shock front of arbitrary strength (Equation (14)) was used for the analytic estimate. The pressure from shock reflection was then computed using Equation (15), and this result is also listed in Table VI-1. The ratio of specific heats for a monatomic, unionized gas was used in the analytic estimate of the reflected pressure. For the 50 torr gas, the FIRE results agree to within a few percent of the analytic estimate. But at lower gas densities the deposited energy becomes decoupled from hydrodynamic motion, so the analytic estimate overestimates the shock pressure. This is illustrated in Figure VI-3.a through VI-3.d. Figure VI-3.a shows how the thermal wave is coincident with the shock until 10^{-4} seconds after the burn, at which time the thermal wave falls behind the shock in a manner similar to Stage C of the atmosphere's response to a nuclear explosion. As explained in Section IV.B.3, a cooling wave is not expected when the deposited energy is only 30 MJ, and the results of the FIRE code bear this out. For an ambient gas density less than 50 torr, the deposited energy produces higher temperatures and hence a higher radiation emission rate. The propagation speed of the thermal wave increases as the emission rate increases, and if the gas density is low enough then the thermal wave will overtake the shock wave. This situation is shown in Figures VI-3.b through VI-3.d. If the thermal wave overtakes the shock wave, a portion of the deposited energy is decoupled from hydrodynamic motion, and the

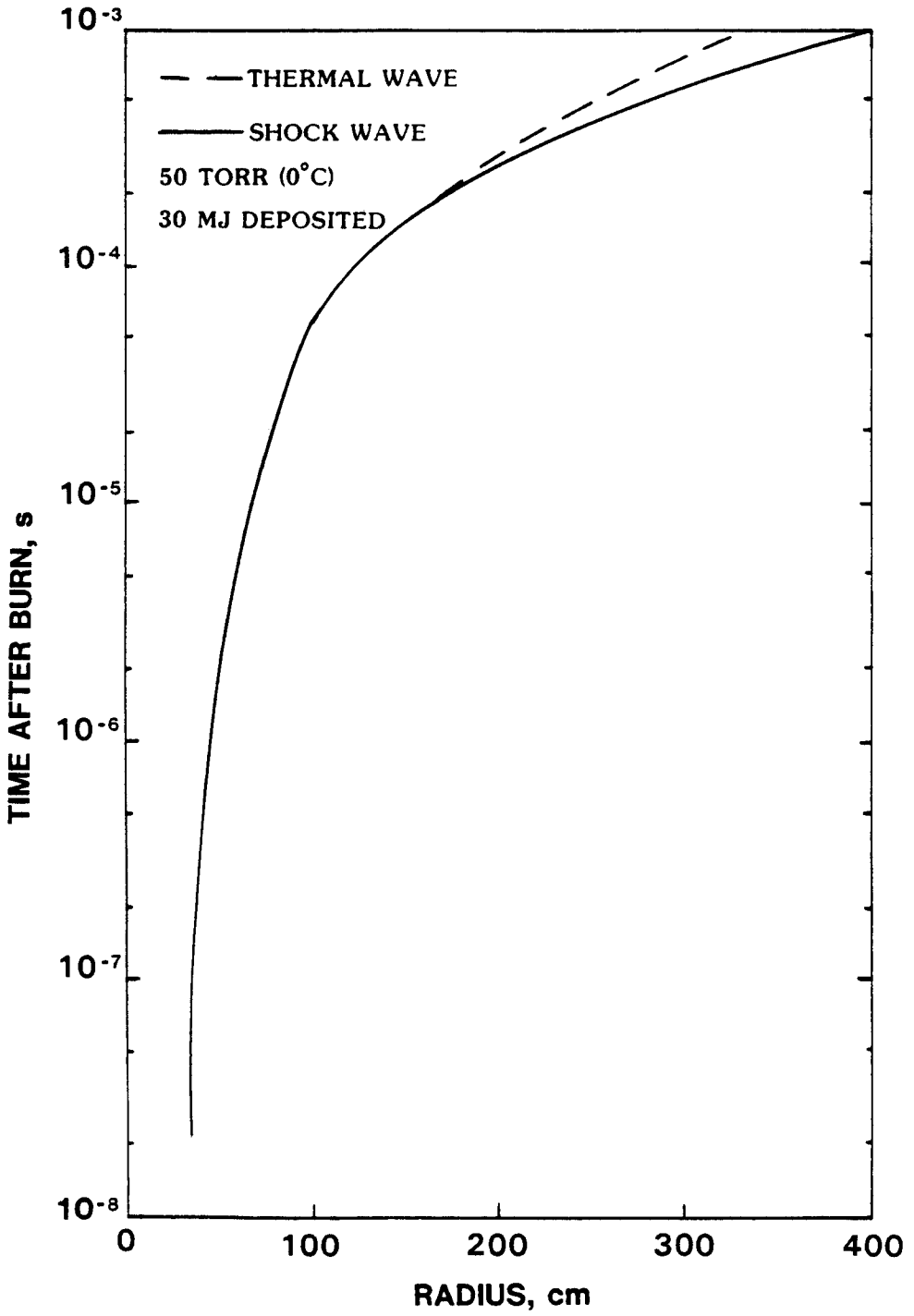

Fig. VI-3.a. The position of the thermal and shock wave as a function of time for a density corresponding to 50 torr (0°C).

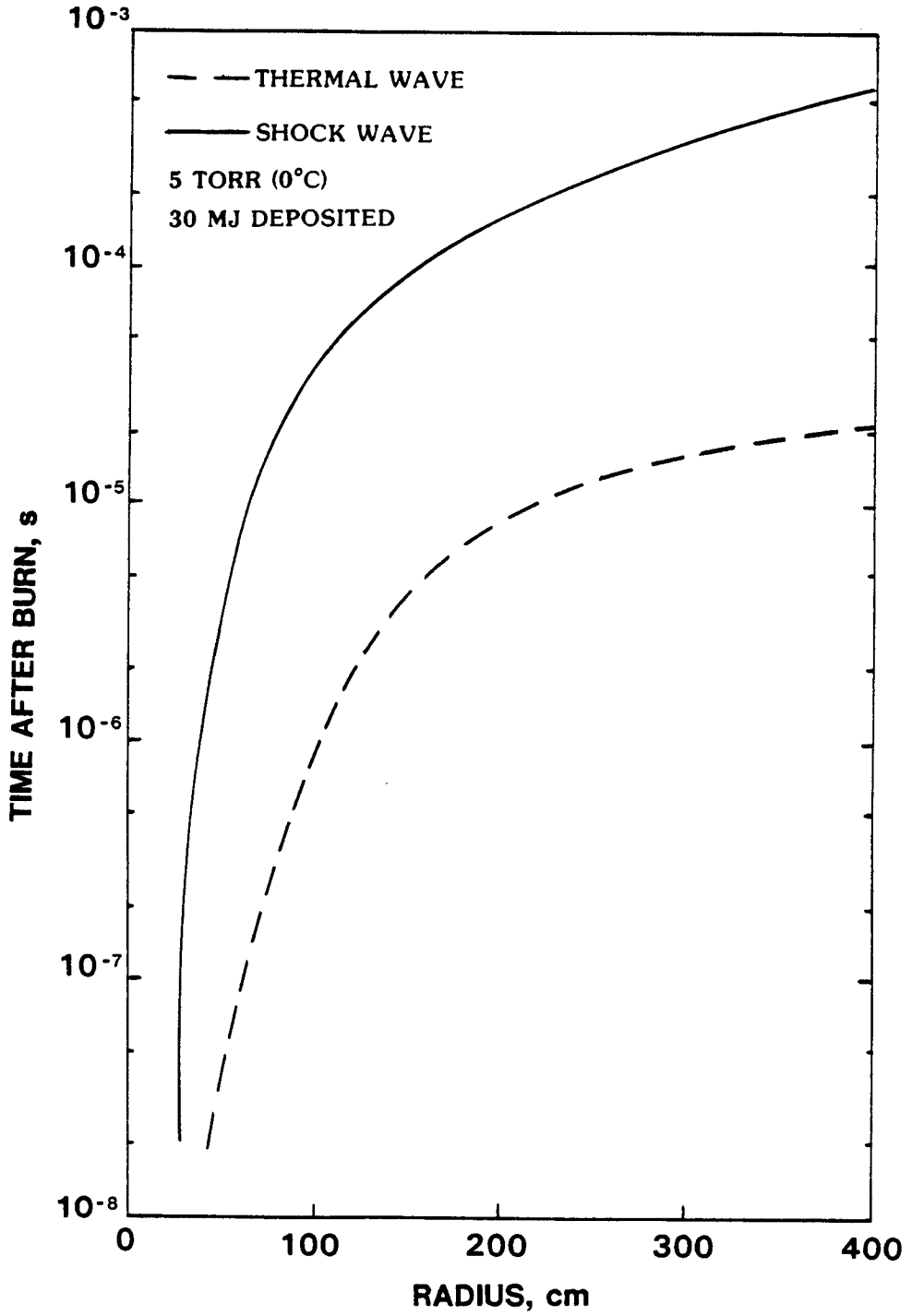

Fig. VI-3.b. The position of the thermal and shock wave as a function of time for a density corresponding to 5 torr (0°C).

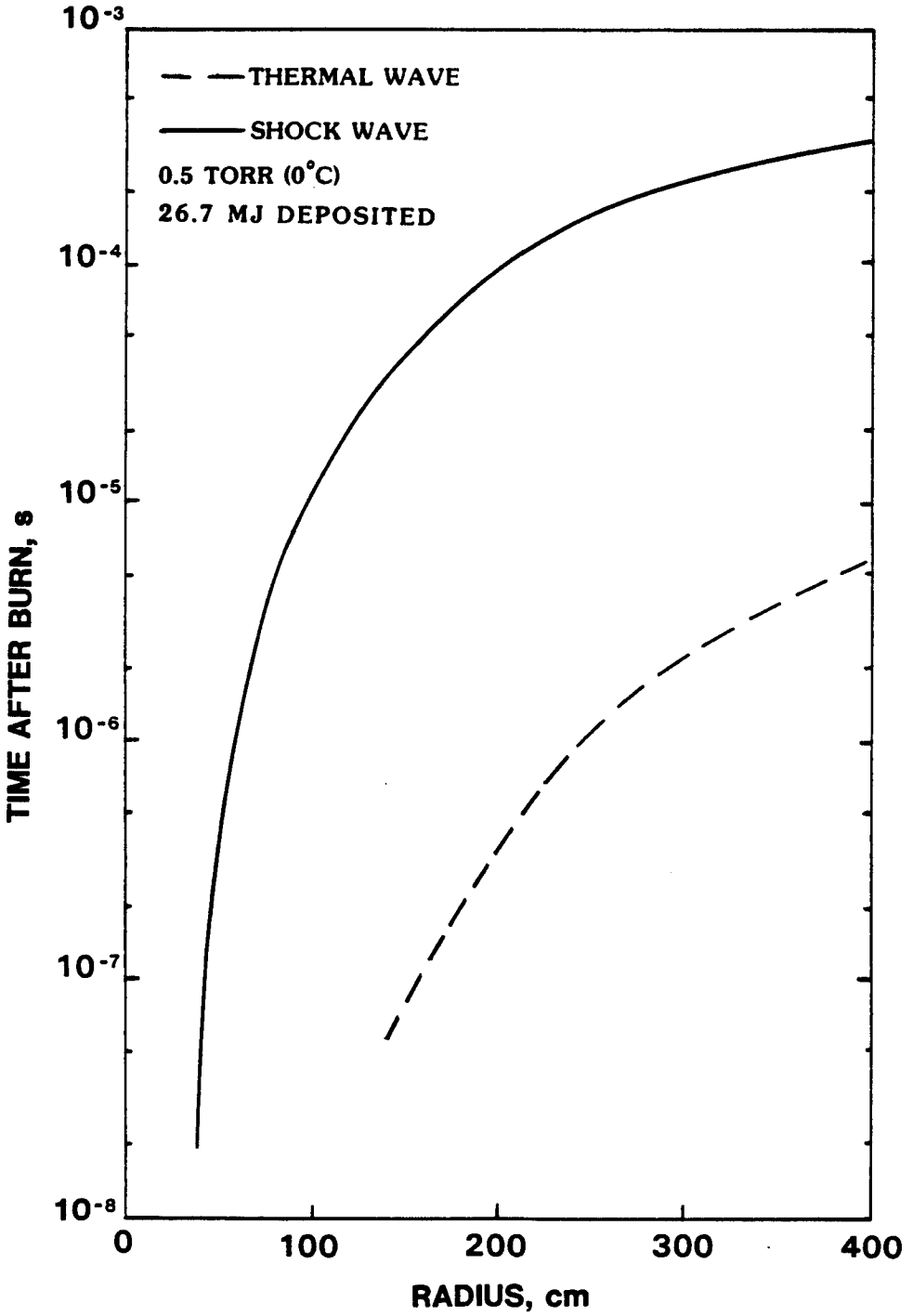

Fig. VI-3.c. The position of the thermal and shock wave as a function of time for a density corresponding to 0.5 torr (0°C).

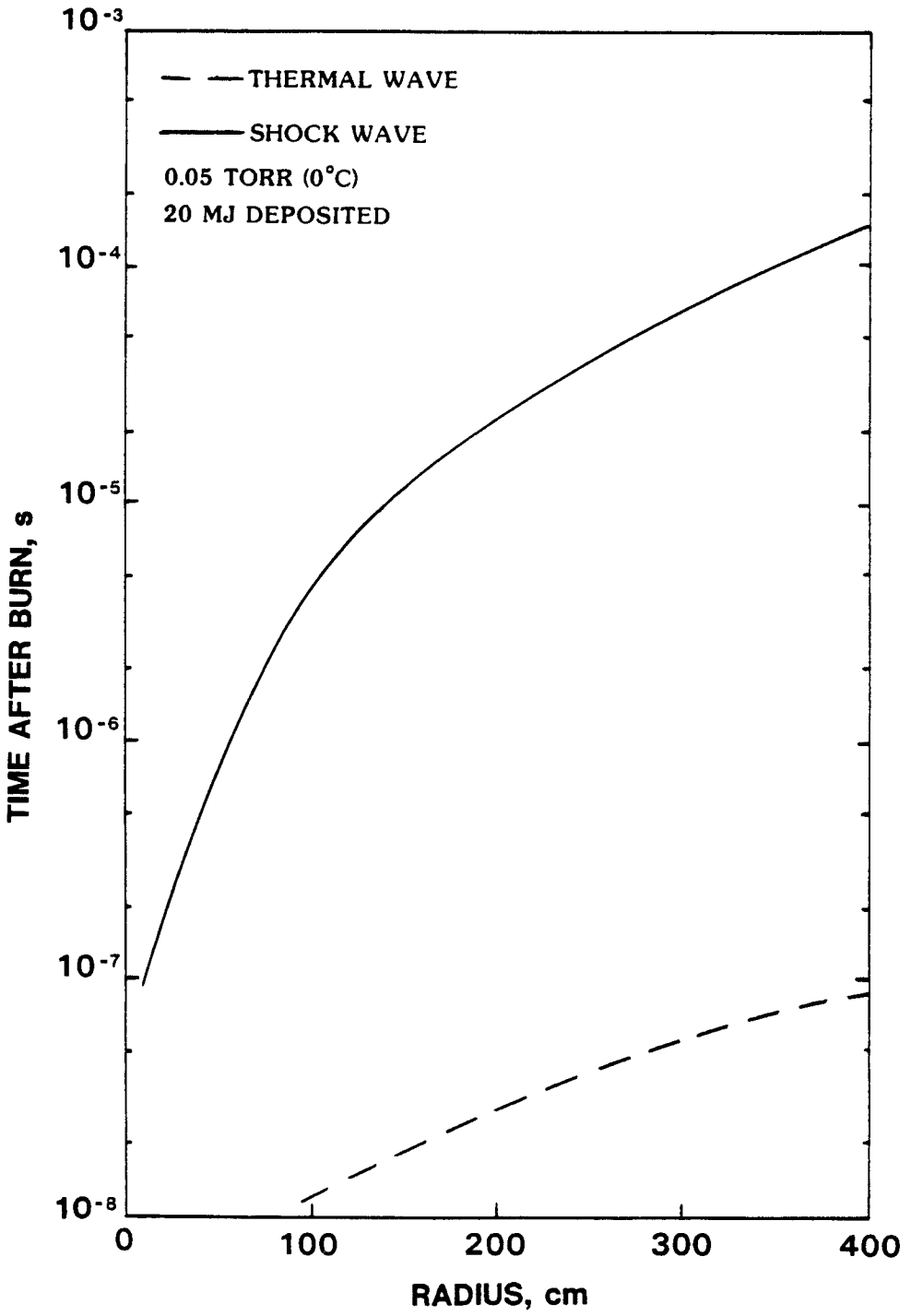

Fig. VI-3.d. The position of the thermal and shock wave as a function of time for a density corresponding to 0.05 torr (0°C).

pressure gradient driving the shock is reduced. The analytic estimates of the pressure rise at the shock front listed in Table VI-1 fail to account for this decoupling, so the pressure rise was overestimated.

Figures VI-4.a through VI-4.d show the deformation of the Lagrangian zones as a function of time. With an ambient density of 50 torr, the deformation is induced by adiabatic expansion behind the shock. For an ambient density of 5.0 torr or lower, the expansion is no longer adiabatic because a portion of the deposited energy is uncoupled from hydrodynamic motion. For ambient densities as low as 0.5 and 0.05 torr, the deformation is due mostly to the momentum of the target debris.

The energy absorbed by the first wall is comprised of low energy photons ($\approx$ 1 eV), and unattenuated target x-rays. The heat flux reaching the wall is strongly dependent upon the gas temperature, partly because of the strong temperature dependence of the Planck mean free path. Figure VI-5 shows how the equilibrium Planck mean free path varies with temperature for the four ambient densities being considered. The mean free path is not quite inversely proportional to density because the photon interaction cross sections are also slightly density dependent. Figure VI-6 illustrates the heat flux from unattenuated target x-rays and gas radiation as computed by the FIRE code. The increase in x-ray flux with a decrease in density is expected because the attenuation coefficient is proportional to the density. The increase in flux radiated from the gas

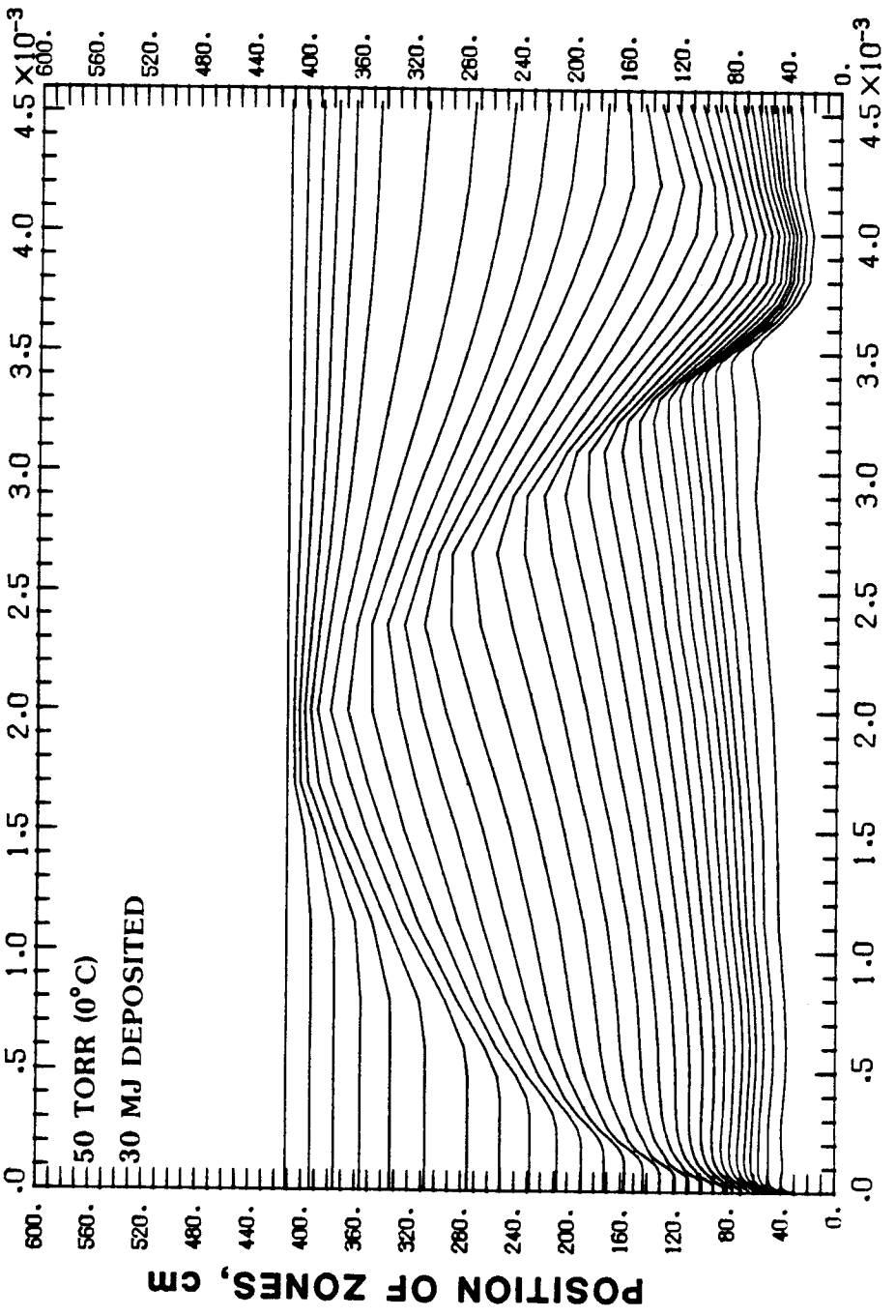

Fig. VI-4.a. The position of the Lagrangian zones as a function of time for a density corresponding to 50 torr (0°C).

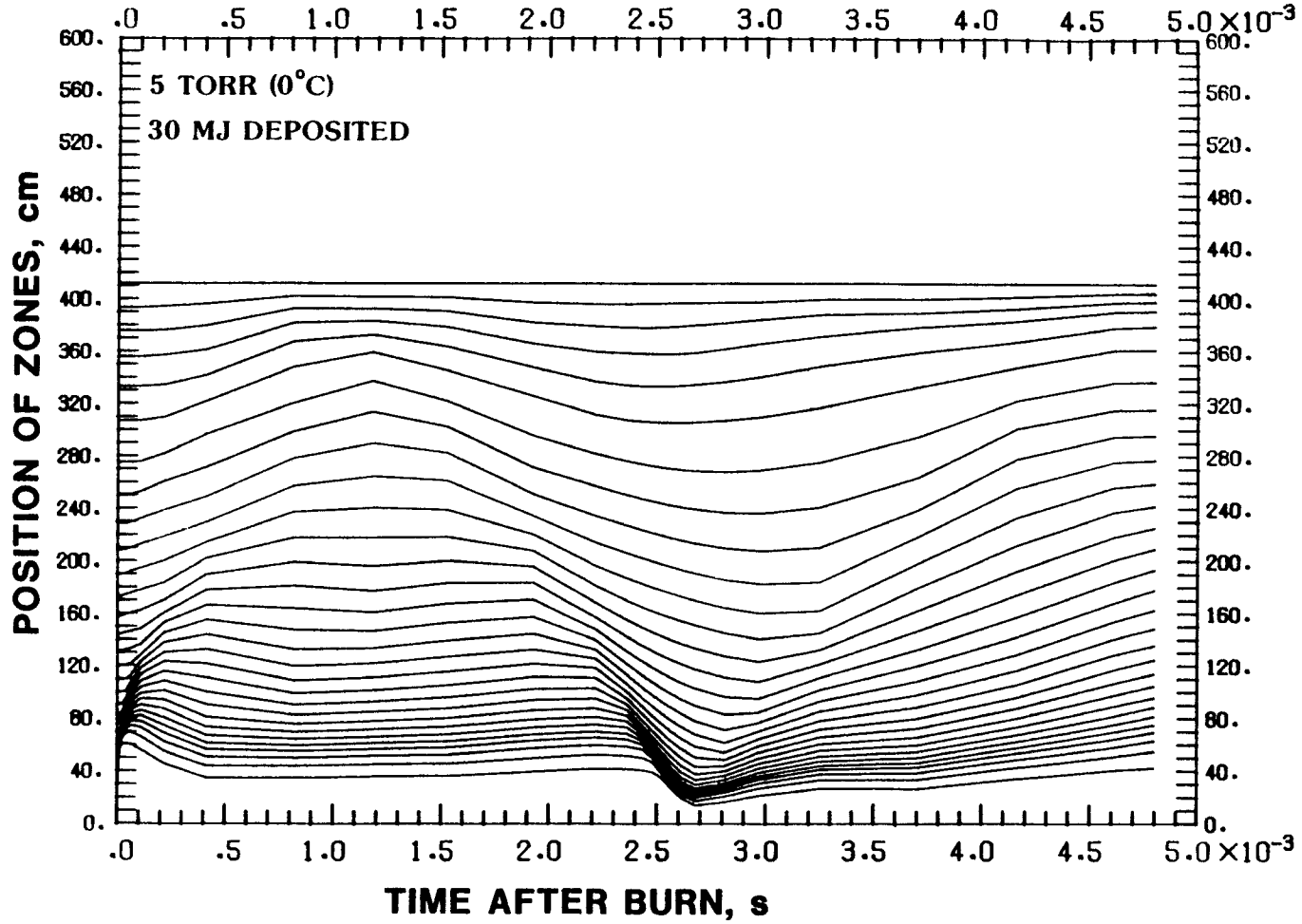

Fig. VI-4.b. The position of the Lagrangian zones as a function of time for a density corresponding to 5 torr (0°C).

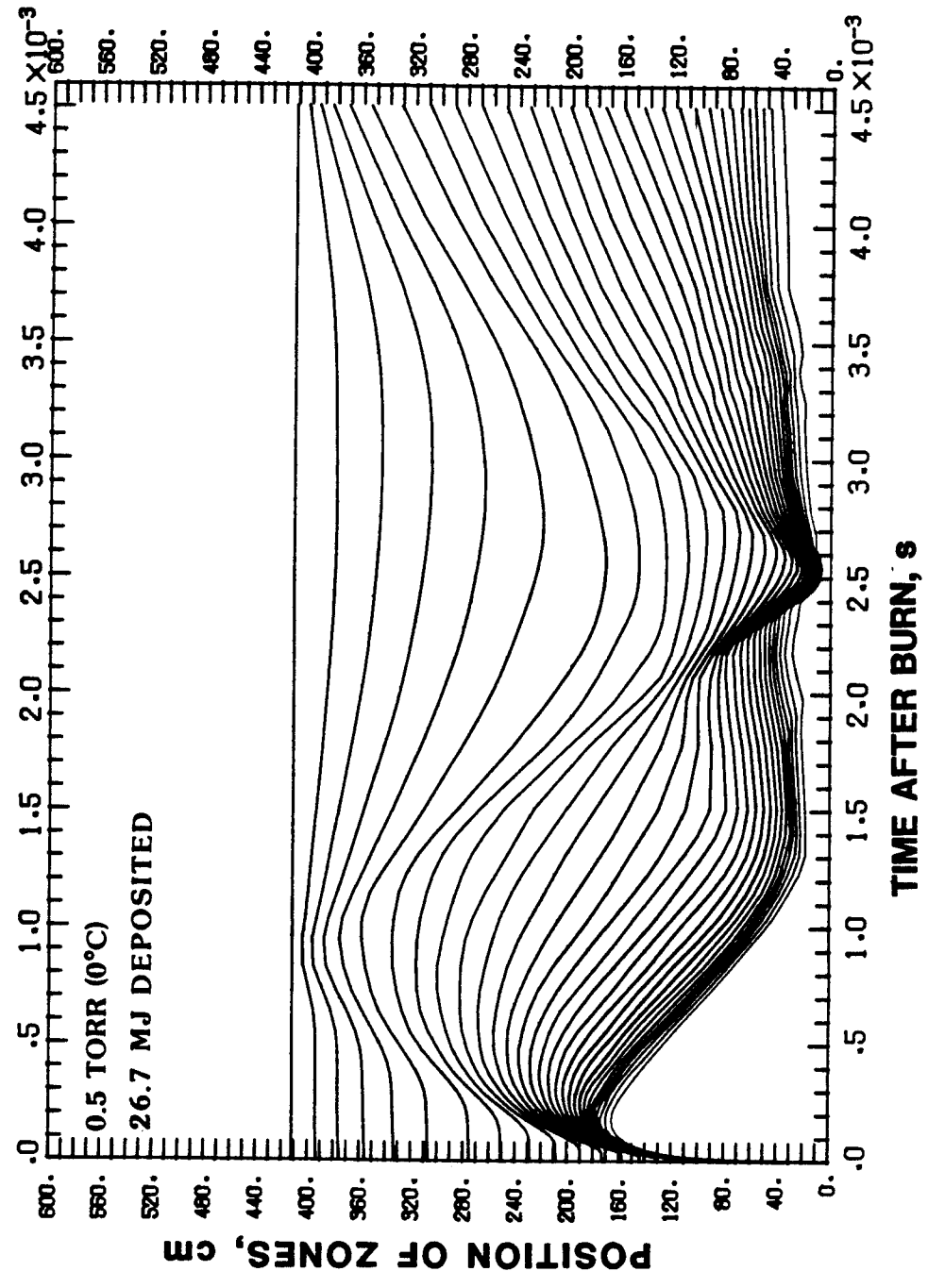

Fig. VI-4.c. The position of the Lagrangian zones as a function of time for a density corresponding to 0.5 torr (0°C).

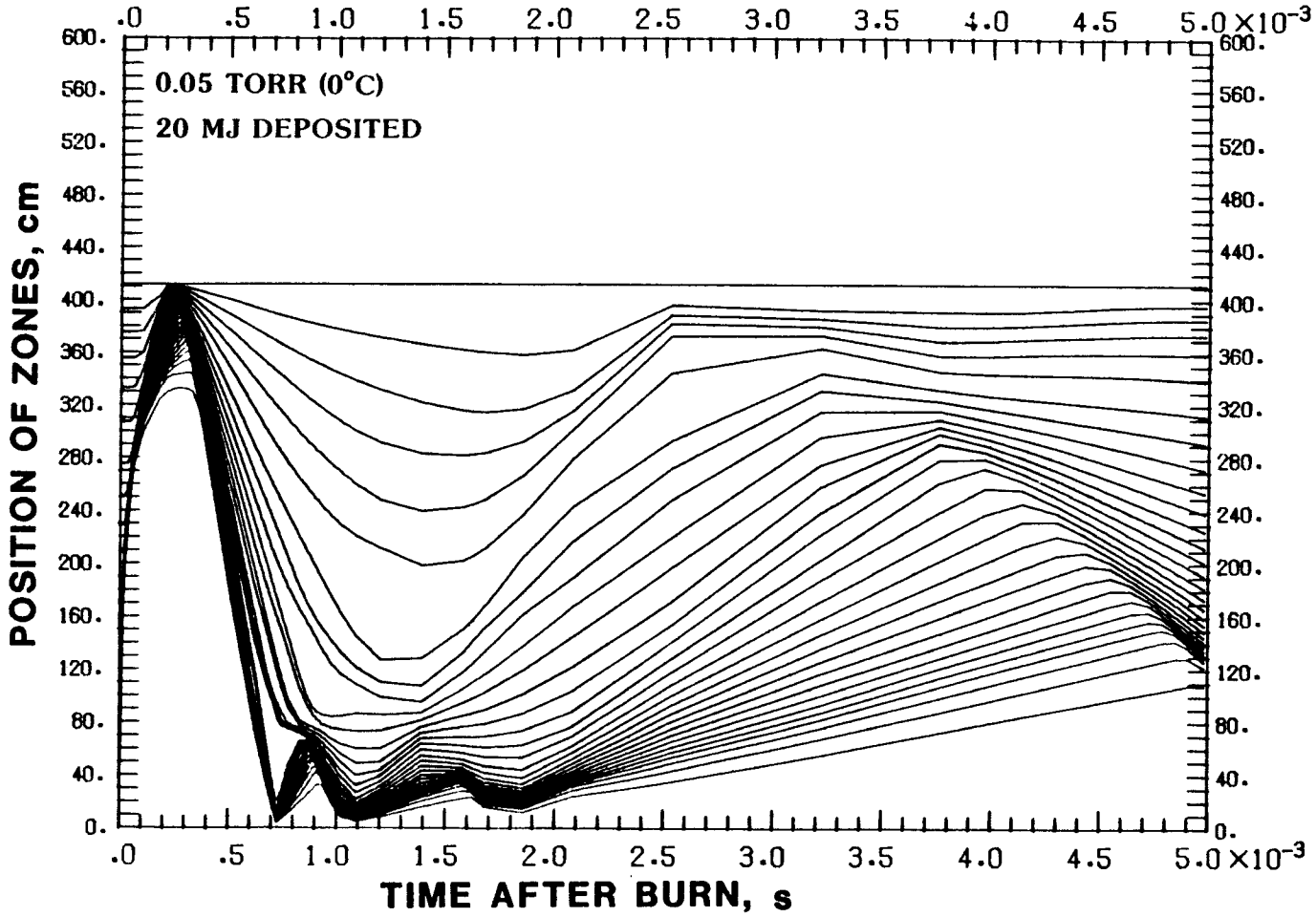

Fig. VI-4.d. The position of the Lagrangian zones as a function of time for a density corresponding to 0.05 torr (0°C).

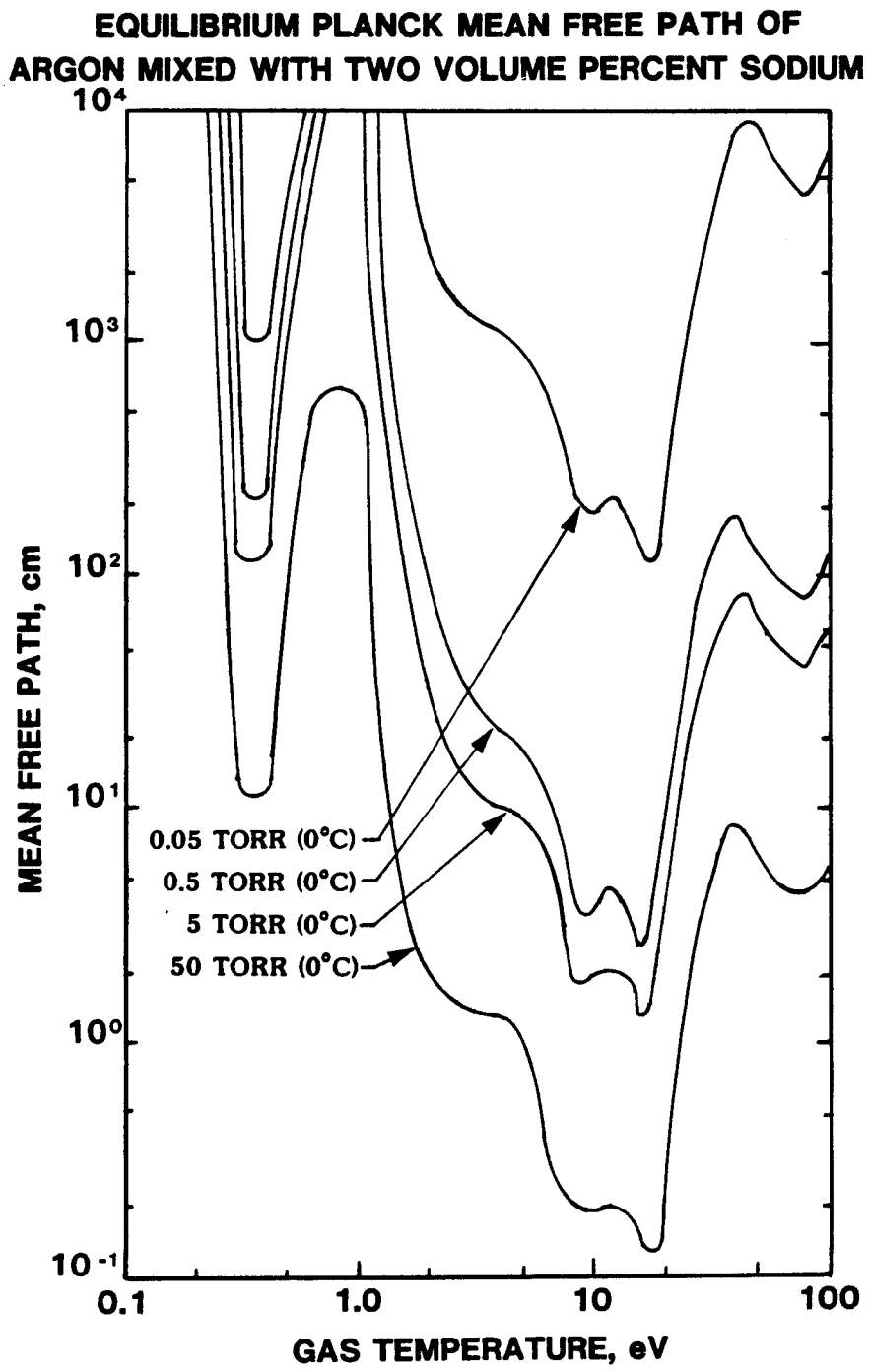

Fig. VI-5. The equilibrium Planck mean free path for argon mixed with two volume percent sodium.

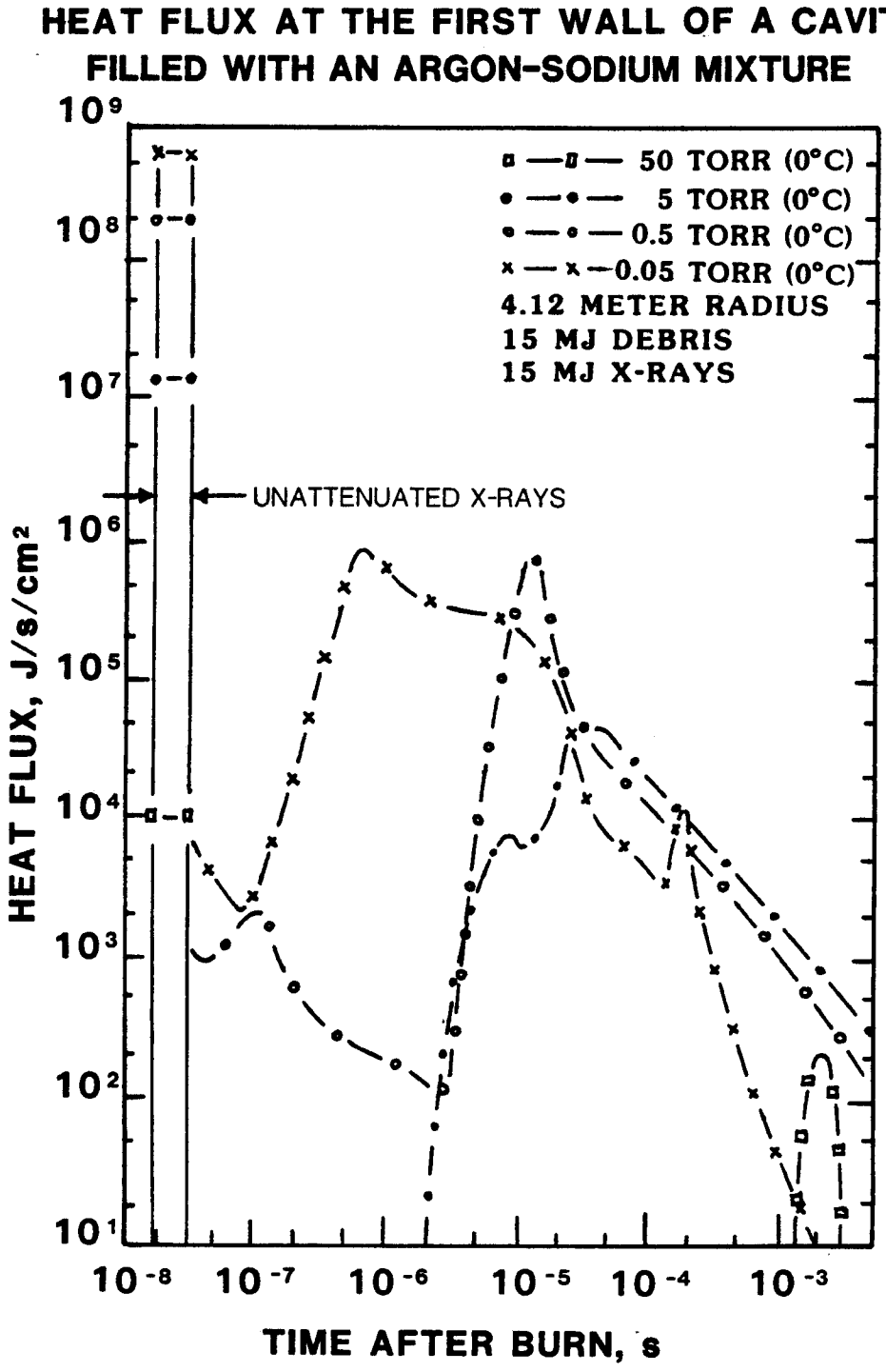

Fig. VI-6. The heat flux from unattenuated target x-rays and gas reradiation.

is also expected with a decrease in density because the average temperature of the gas increases as the density decreases. Table VI-2 lists the average energy fluence and energy flux from target x-rays and gas radiation.

The results of the FIRE code calculations that have been discussed here were used by Hassanein[87] to determine the minimum buffer gas density required to protect the first wall of a commercial reactor from erosion by evaporation. Figure VI-7 shows that for a power plant operating at 1000 MW thermal with a first wall designed to last over 30 full power years, over 1/3 of a torr is required to prevent evaporative erosion of a carbon first wall, and 1 torr is required to prevent evaporative erosion of a stainless steel first wall.

B.2. The Dependence of the Buffer Gas Response on the Gas Species

The FIRE code calculations that are presented in this subsection illustrate the response for four gases that are candidates for use in a light ion driven reactor; pure argon, argon with two volume percent sodium, pure xenon, and xenon with five volume percent cesium. A gas density corresponding to 50 torr at standard temperature was chosen for these examples. The results of the FIRE code calculations indicate that this density is high enough to attenuate all 30 MJ of the x-ray and debris energy.

Table VI-3 compares the peak pressure from shock reflection at the wall that was computed by the FIRE code with that computed by Equations (14) and (15). The ratio of specific heats for a mona-

Table VI-2. The Energy Fluence and Energy Flux from Gas Radiation and Unattenuated Target X-Rays

Ar (0.2% Na)	Unattenuated X-Rays		Gas Radiation	
Gas Density, Torr (0°C)	Energy Fluence, J/cm^2	Average Flux, W/cm^2	Energy Fluence, J/cm^2	Average Flux, W/cm^2
0.05	5.66	6.55×10^8	8.5	8.5×10^5
0.5	2.33	2.33×10^8	12	8.0×10^4
5.0	0.15	0.15×10^8	14	1.0×10^4
50.0	10^{-4}	1.0×10^4	14	2.0×10^2

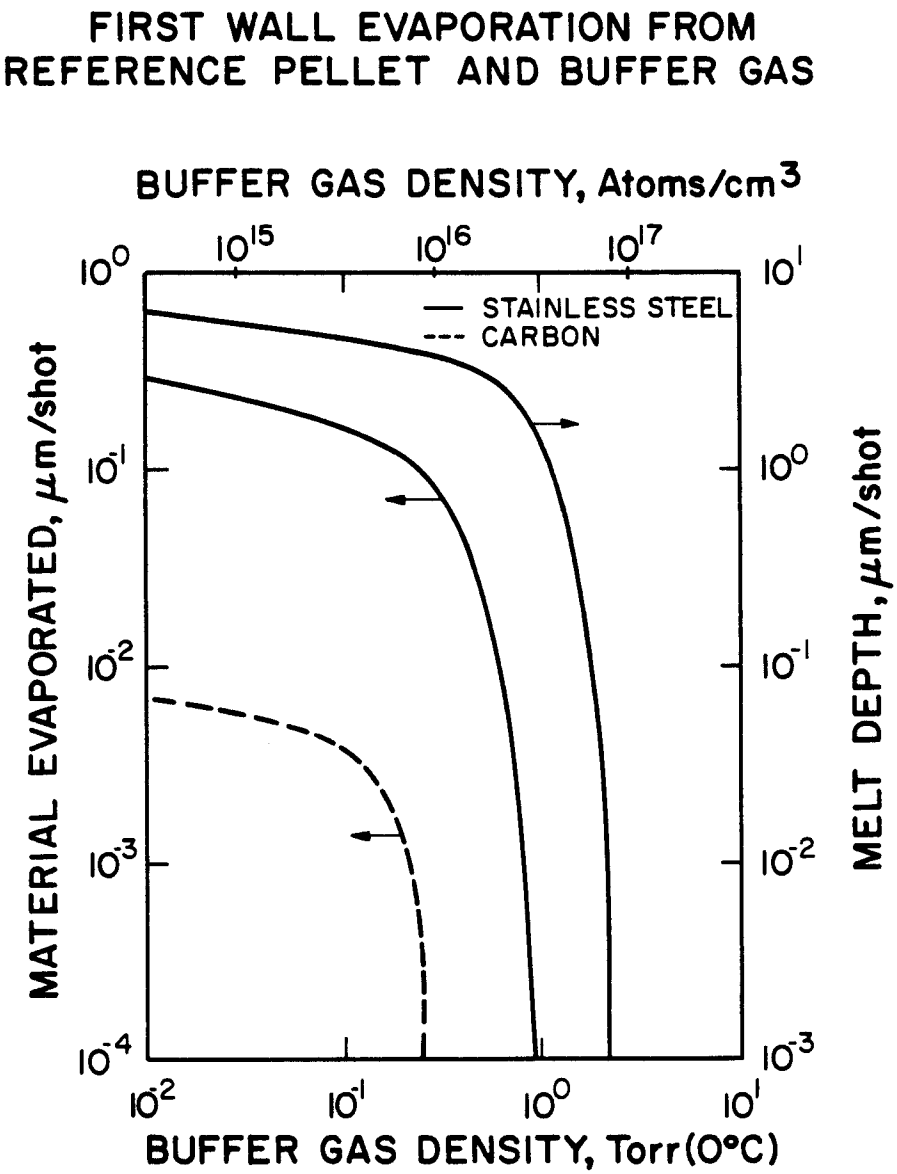

Fig. VI-7. First wall evaporation as a function of gas density for carbon and stainless steel first walls (Ref. 87).

Table VI-3. A Comparison Between the Peak Pressure Computed at the Wall by the FIRE Code and an Analytic Estimate

Buffer Gas	Ambient Pressure, J/cm^3	Deposited Energy, MJ	Analytic Estimate		FIRE Code
			Shock Pressure, J/cm^3	Reflected Pressure, J/cm^3	Reflected Pressure, J/cm^3
Pure Argon	1.44×10^{-2}	30 MJ	0.10	0.40	.35
Argon 2% Sodium	1.44×10^{-2}	30 MJ	0.10	0.40	.38
Pure Xenon	1.44×10^{-2}	30 MJ	0.10	0.40	.35
Xenon 5% Cesium	1.44×10^{-2}	30 MJ	0.10	0.40	.38

tomic, unionized gas was used in Equations (14) and (15). The relatively good agreement between the FIRE code estimate of the peak pressure and the estimate using Equations (14) and (15) is an indication that for these gases most of the deposited energy is coupled into hydrodynamic motion. However, the FIRE code results reveal how the coupling is slightly stronger for the gas mixtures than for the pure gases. The reason for this is that the gas mixtures are more opaque to thermal radiation than the pure gases.

Figure VI-8.a shows that the position of the thermal and shock waves in pure argon and the argon-sodium mixture are identical. Although the gas motion is the same, the strength of the shock and the character of radiation transport differs somewhat. With pure argon, some of the radiation emitted behind the thermal wave is transported ahead of the shock, and is thus decoupled from hydrodynamic motion. But when two volume percent sodium is added, virtually all of the radiation emitted behind the thermal wave is absorbed before it reaches the shock. Figure VI-8.b shows the position of the shock and thermal wave for pure xenon and xenon mixed with five volume percent cesium. Mixing cesium with a noble gas has the same effect on the opacity that mixing in sodium does. Comparing Figures VI-8.a and VI-8.b shows how it takes longer for the shock to traverse the xenon gases than it does to traverse the argon gases. This is expected because the shock speed is inversely proportional to the square root of the atomic number of the gas. The propagation

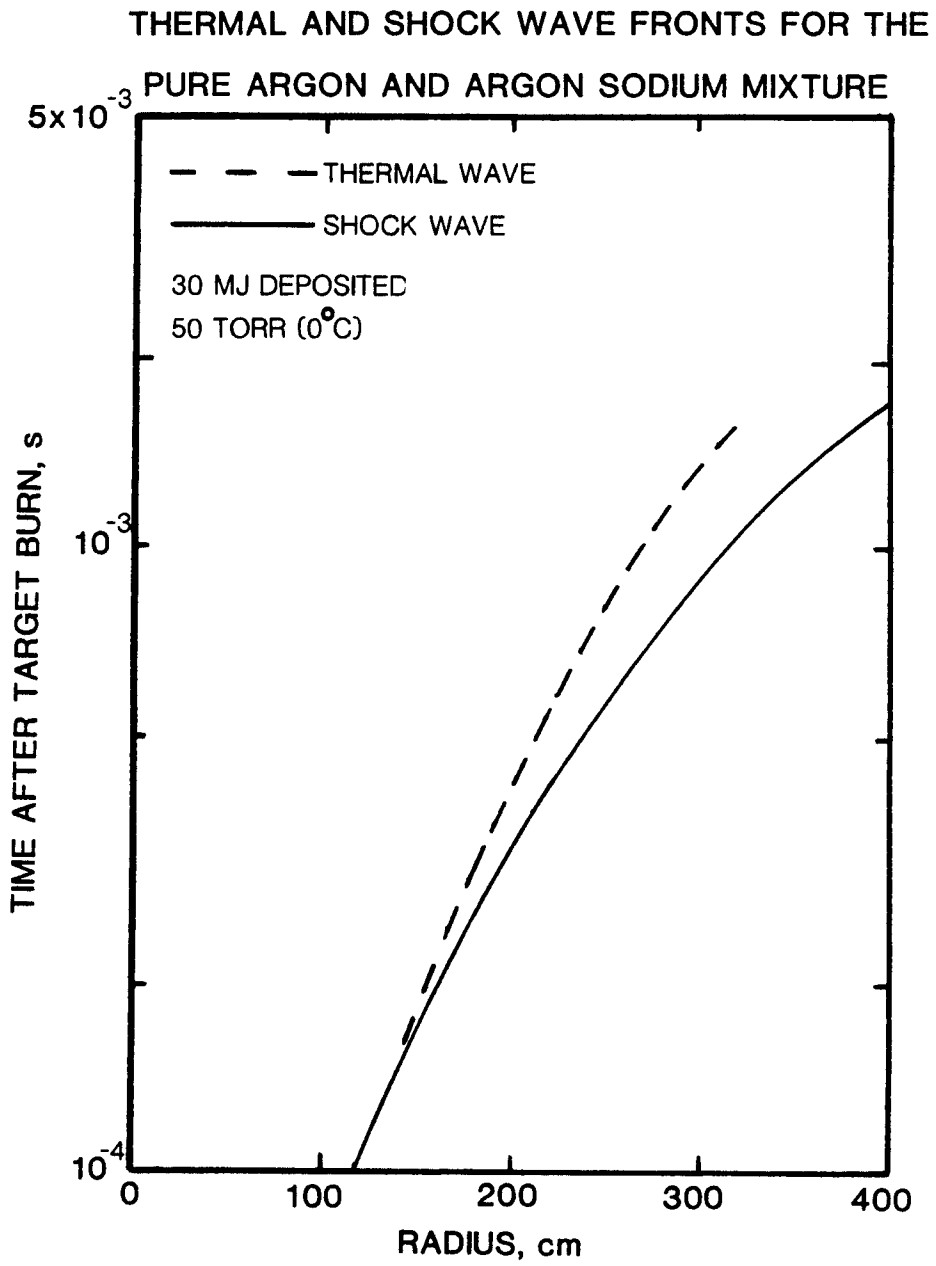

Fig. VI-8.a. The position of the thermal wave and the shock wave as a function of time for pure argon and argon mixed with two volume percent sodium.

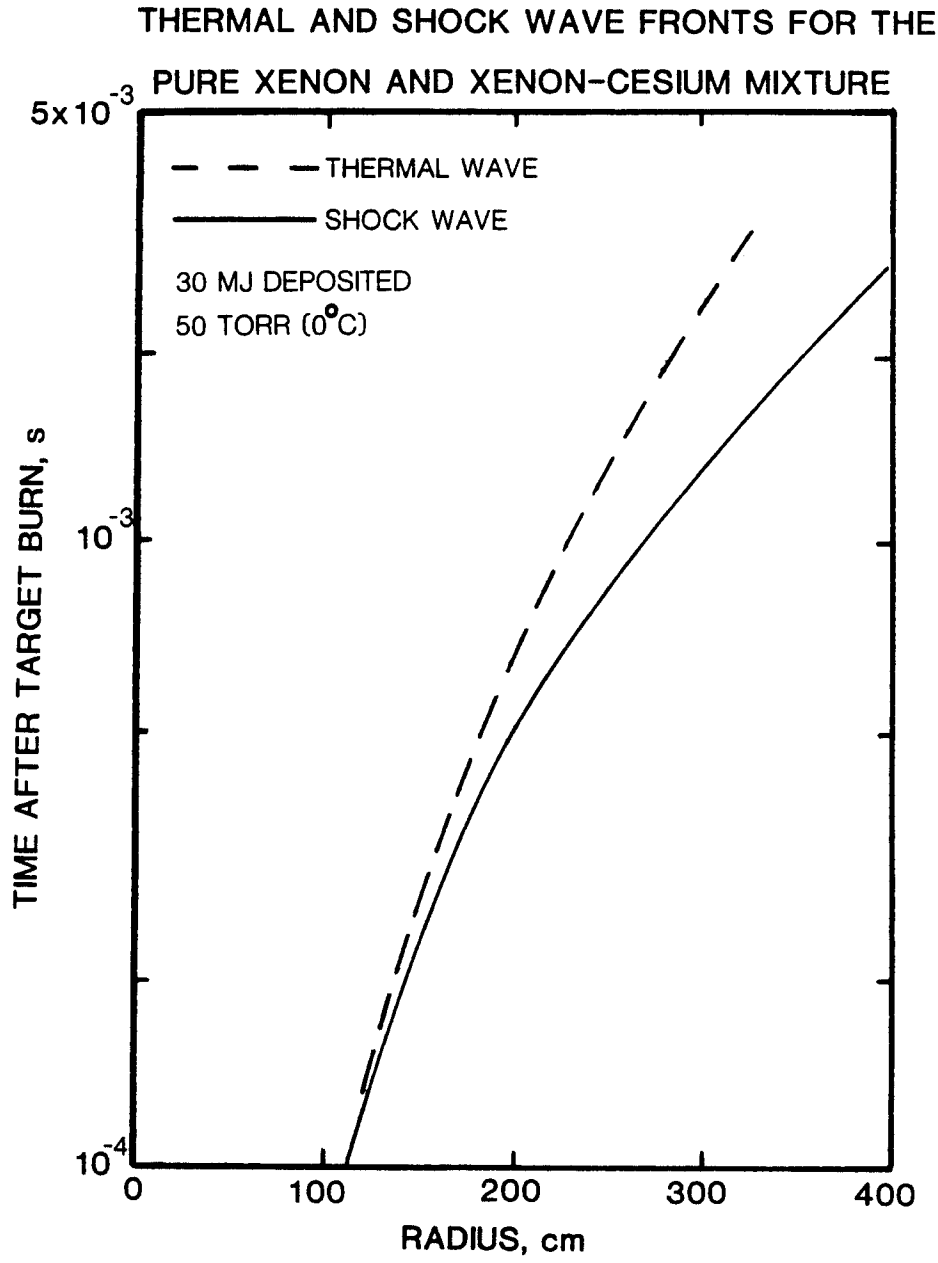

Fig. VI-8.b. The position of the thermal wave and shock wave as a function of time for pure xenon and xenon mixed with five volume percent cesium.

speed of the thermal wave is also faster in the argon gases, because the thermal wave speed is somewhat dependent upon gas motion.

Peterson[87] has investigated how mixing two volume percent sodium with pure argon affects the equilibrium Planck mean free path. The Planck mean free paths computed by MIXER are illustrated in Figure VI-9.a. At temperatures below about 1 eV, the equilibrium Planck mean free path is smaller for the argon-sodium mixture than for pure argon. Sodium has a similar effect on the nonequilibrium Planck mean free path, but it is difficult to illustrate this effect because the non-equilibrium mean free path is a function of both the gas temperature and the radiation temperature. Figure VI-9.b shows the results of MIXER code calculations for the equilibrium Planck mean free path of pure xenon and xenon mixed with cesium. The mean free path of the xenon-cesium mixture is less than that of pure xenon at temperatures below about 1 eV.

Figure VI-10.a shows the heat flux at the first wall as a function of time for pure argon and the argon-sodium mixture. With pure argon, the gas ahead of the shock is semi-transparent to radiation, so some radiation reaches the wall before the shock does. The oscillations in the heat flux occur because the radiation emission rate of the gas within the cavity oscillates as the shock oscillates back and forth. With the argon-sodium mixture, the heat flux at the wall does not begin to increase until the shock reaches the wall. As the shock is reflected, some of the internal energy is radiated to the wall. There are no oscillations in the heat flux when the argon-

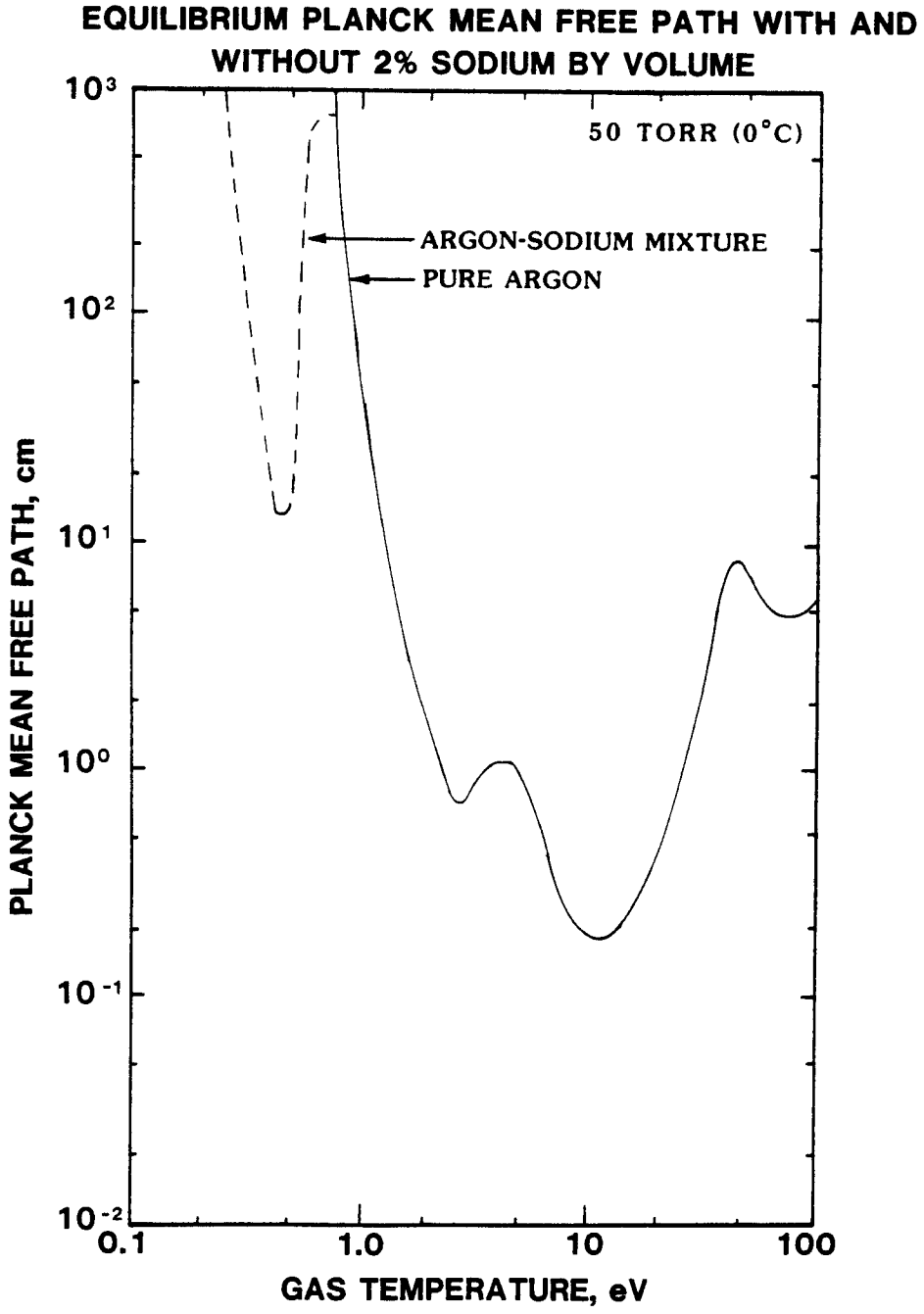

Fig. IV-9.a. The equilibrium Planck mean free path of argon with and without two volume percent sodium mixed in.

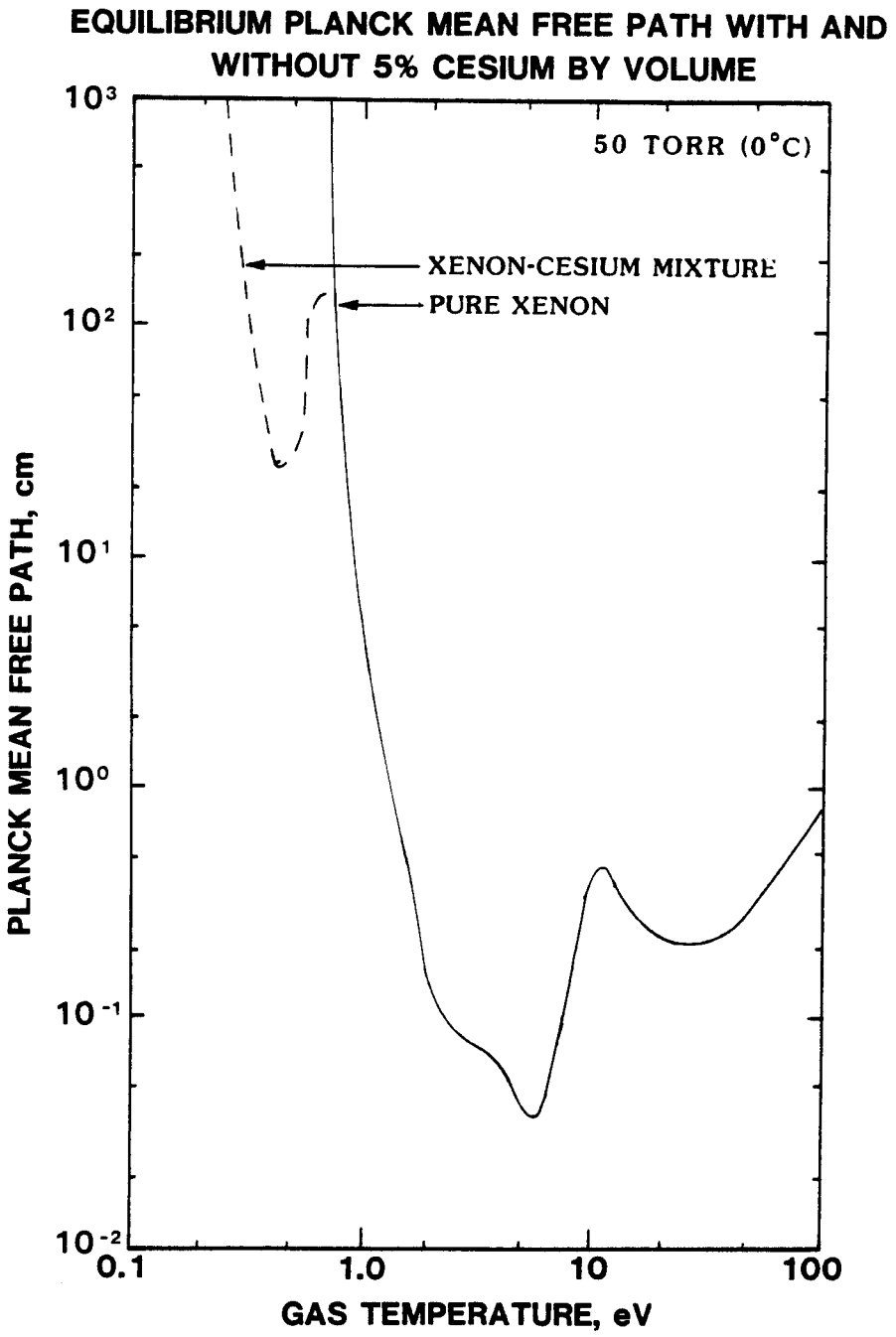

Fig. VI-9.b. The equilibrium Planck mean free path of xenon with and without five volume percent cesium mixed in.

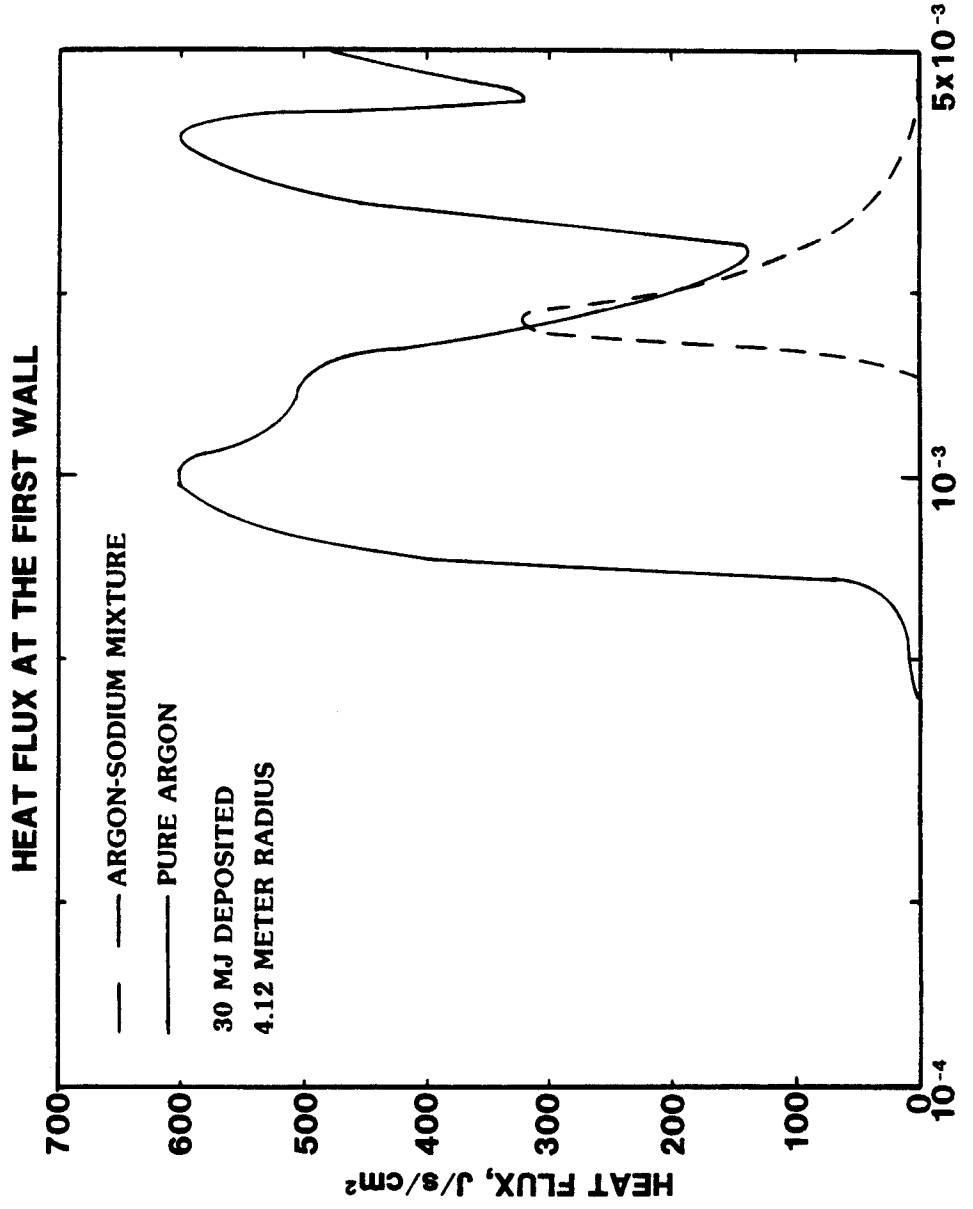

Fig. VI-10.a. The heat flux at the first wall from a pure argon buffer gas and from argon mixed with two volume percent sodium.

sodium mixture is used because the gas at the wall is opaque to oscillations in the radiation emission rate that occur deeper within the cavity. Figure VI-10.b shows similar curves for pure xenon and xenon mixed with five volume percent cesium. Mixing a small amount of cesium with the xenon buffer gas has the same effect on the heat flux at the wall as mixing a small amount of sodium with argon does.

B.3. The Dependence of the Buffer Gas Response on Target Yield

The pressure and heat flux at the wall are studied in this section as a function of target yield. As in previous examples, 15% of the target yield is assumed to be in 0.3 keV blackbody x-rays, and 15% in the kinetic energy of 1 gram of iron target debris. The opacity and equation of state of argon mixed with two volume percent sodium was used in these examples, and the ambient gas density corresponds to 50 torr at standard temperature. At this density, all of the x-ray and debris energy is attenuated by the gas.

The peak pressure during shock reflection that is computed by the FIRE code is compared to that computed by Equations (14) and (15) in Figure VI-11. The ratio of specific heats for an un-ionized, perfect gas was used in Equations (14) and (15). The analytic estimate predicts a larger peak pressure because those equations assume all of the deposited energy is coupled into hydrodynamic motion. But in fact, some of the deposited energy is converted into potential energy as the gas is ionized. Both the integration constant, B, that appears in Equation (14), and the ratio of specific heats, γ, are functions of the ionization. The values for an un-ionized gas are

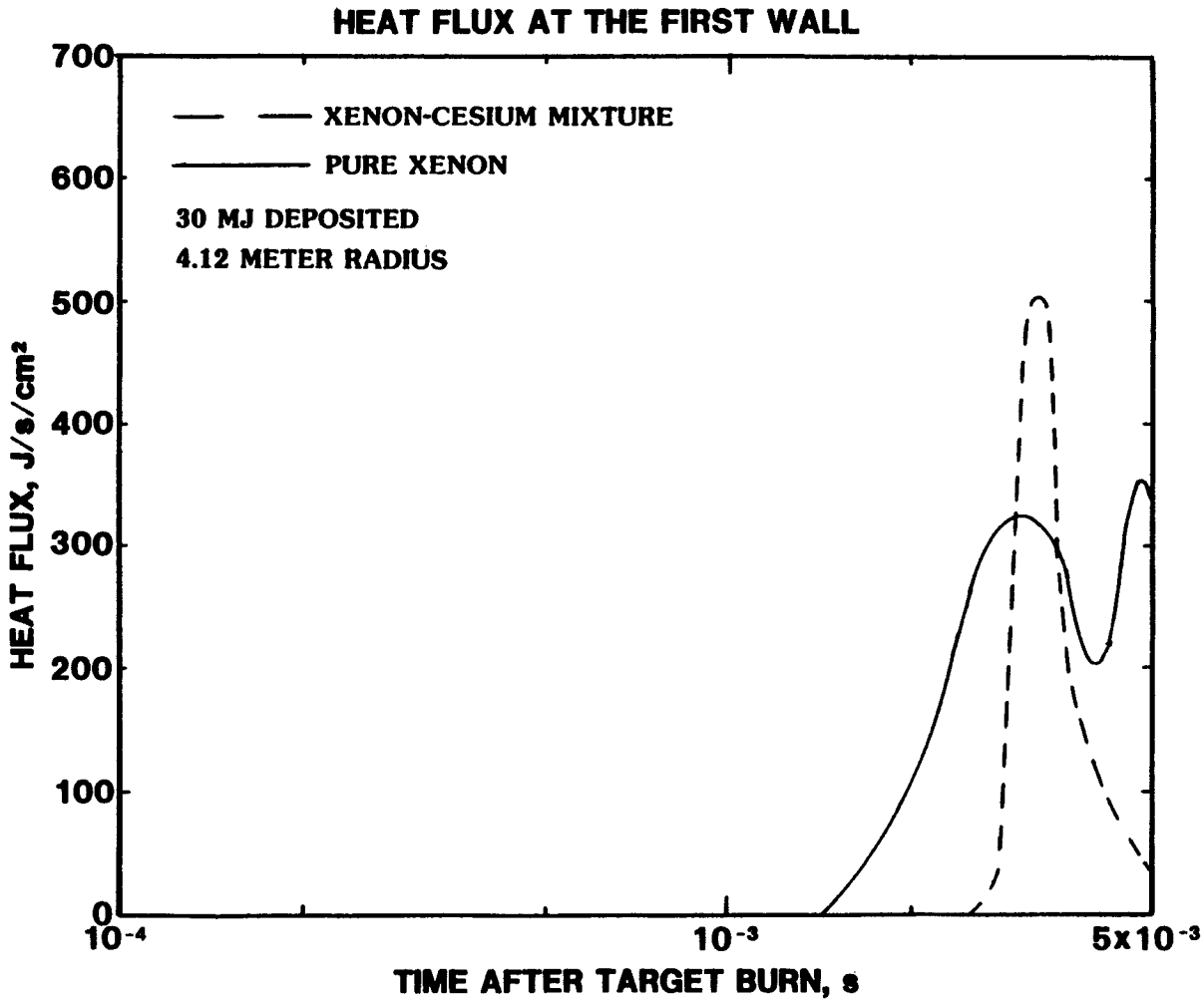

Fig. VI-10.b. The heat flux at the first wall from a pure xenon buffer gas and xenon mixed with five volume percent cesium.

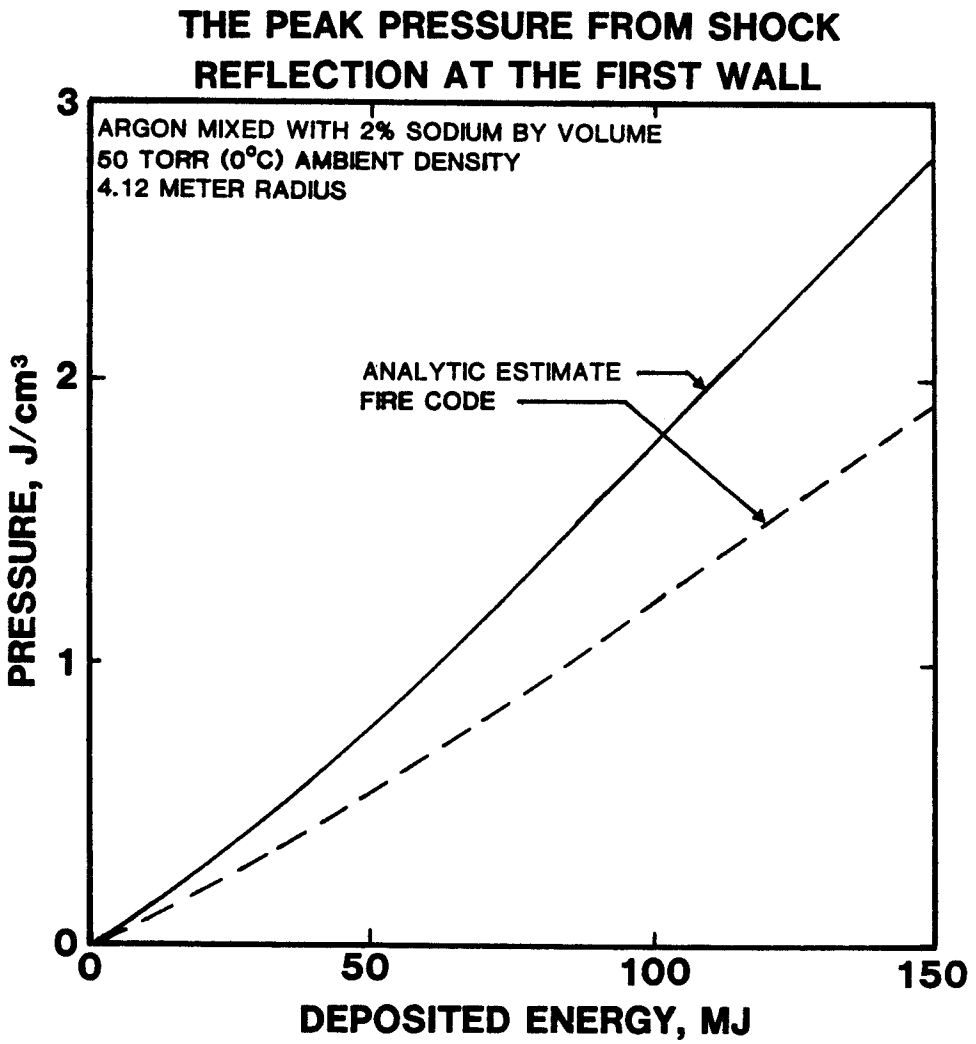

Fig. VI-11. The peak pressure at the first wall as computed by the FIRE code and Equations (14) and (15).

correct only if the point of interest is far enough from the point of explosion that the potential energy of the gas behind the shock is a small fraction of the total internal energy. The realistic equations of state used in the FIRE code calculations have accounted for the increase in potential energy.

Figure VI-12 shows the heat flux at the first wall for 30, 60, and 150 MJ deposited into the gas. In each case, the peak heat flux at the wall occurs during shock reflection. The magnitude of the peak heat flux increases rapidly with an increase in the kinetic energy of the shock. When 30 and 60 MJ are deposited, the layer between the wall and the thermal wave absorbs most of the emitted radiation. When 150 MJ is deposited, the absorbing layer is thinner, so more radiation reaches the wall after the shock is reflected. With even larger yields, the absorbing layer will disappear altogether, and the thermal wave will touch the wall.

B.4. The Influence of Zoning on the FIRE Code Results

The influence of zoning on the FIRE code results is studied in this section. The subroutine ZONER was used to subdivide the reactor cavity into 23, 45, and 90 Lagrangian zones. The equation of state and opacity for pure argon was used in these calculations, and the ambient density corresponds to 50 torr at standard temperature. The deposited energy is 30 MJ in these examples, and all other parameters are the same as in previous examples.

Table VI-4 shows how the peak pressure at the wall varies by less than 10% for the three Lagrangian meshes. The shock arrival

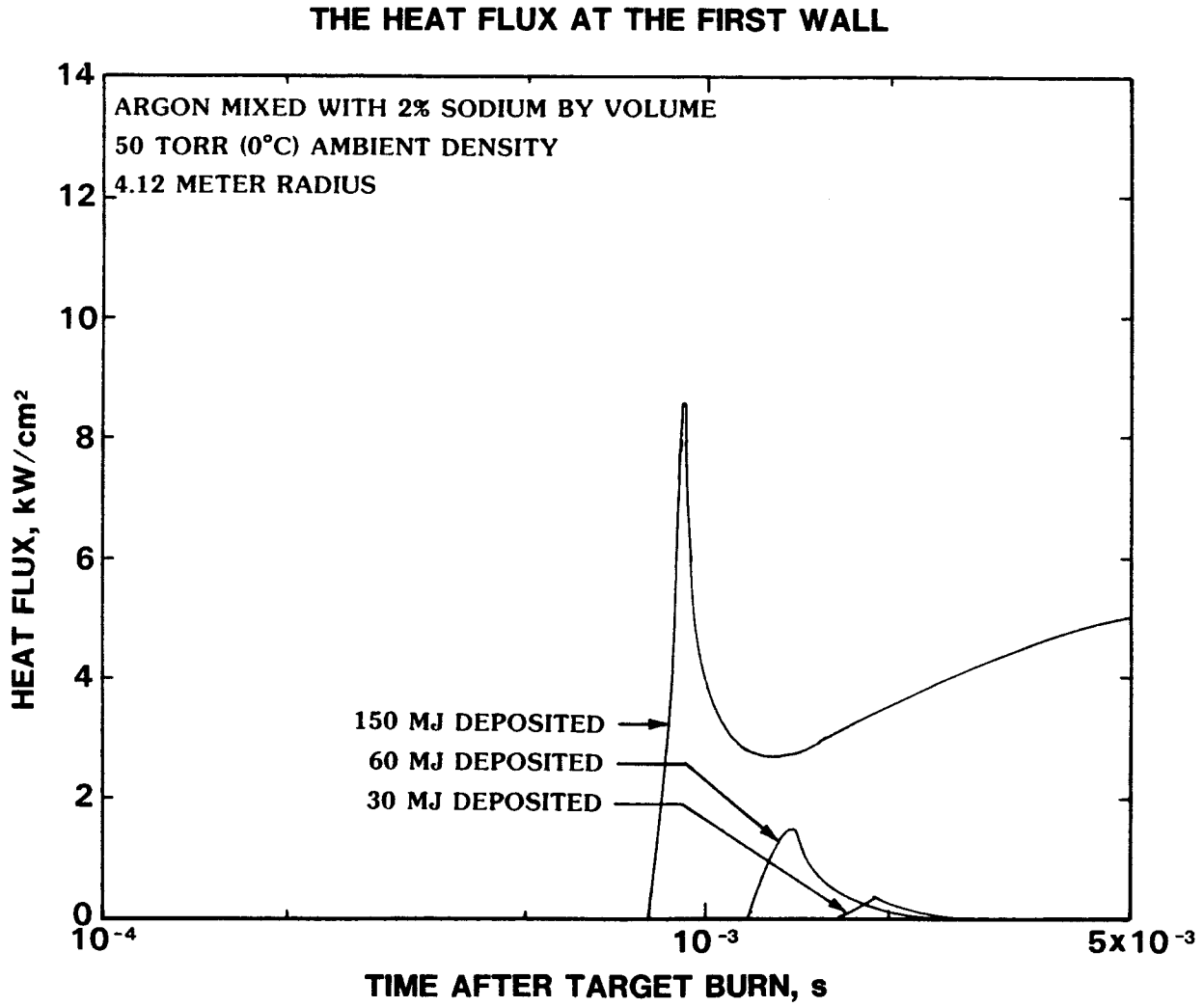

Fig. VI-12. The heat flux at the first wall as a function of time.

Table VI-4. The Peak Pressure at the Wall and the Arrival Time of the Shock Computed Using 23, 45, and 90 Zones

Number of Zones	Peak Pressure, J/cm^3	Arrival Time, s
23	.370	1.67
45	.356	1.65
90	.386	1.65

time is also shown. The calculation using 90 zones required ten times as much computer time as the calculation that used 23 zones, and four times as much computer times as the calculation that used 45 zones. Table VI-4 shows that the calculation of hydrodynamic motion is not very sensitive to the mesh used, so the increase in accuracy gained by using more zones is often not worth the increase in cost.

Figure VI-13 illustrates the heat flux at the first wall that was computed for each mesh. The computed heat flux can be sensitive to zoning because the emission rate is proportional to the fourth power of temperature. However, the improvement in accuracy that is gained by using 90 zones instead of 23 zones is probably not worth the increase in cost, because the equation of state and opacity data produced by MIXER is not that accurate.

When the subroutine ZONER sets up the Lagrangian mesh to be used in a calculation, the last few zones near the wall are arranged so that they each have equal mass. There has been some question as to whether or not this would give the correct peak pressure at the wall, because results from previous versions of the FIRE code have indicated that the computed pressure is sensitive to the thickness chosen for the last zone. The results in Table VI-5 show how the peak pressure computed at the wall is not sensitive to the thickness of the last zone when the current version of FIRE is used. Hence, the method used by the ZONER subroutine to set up the Lagrangian mesh is adequate.

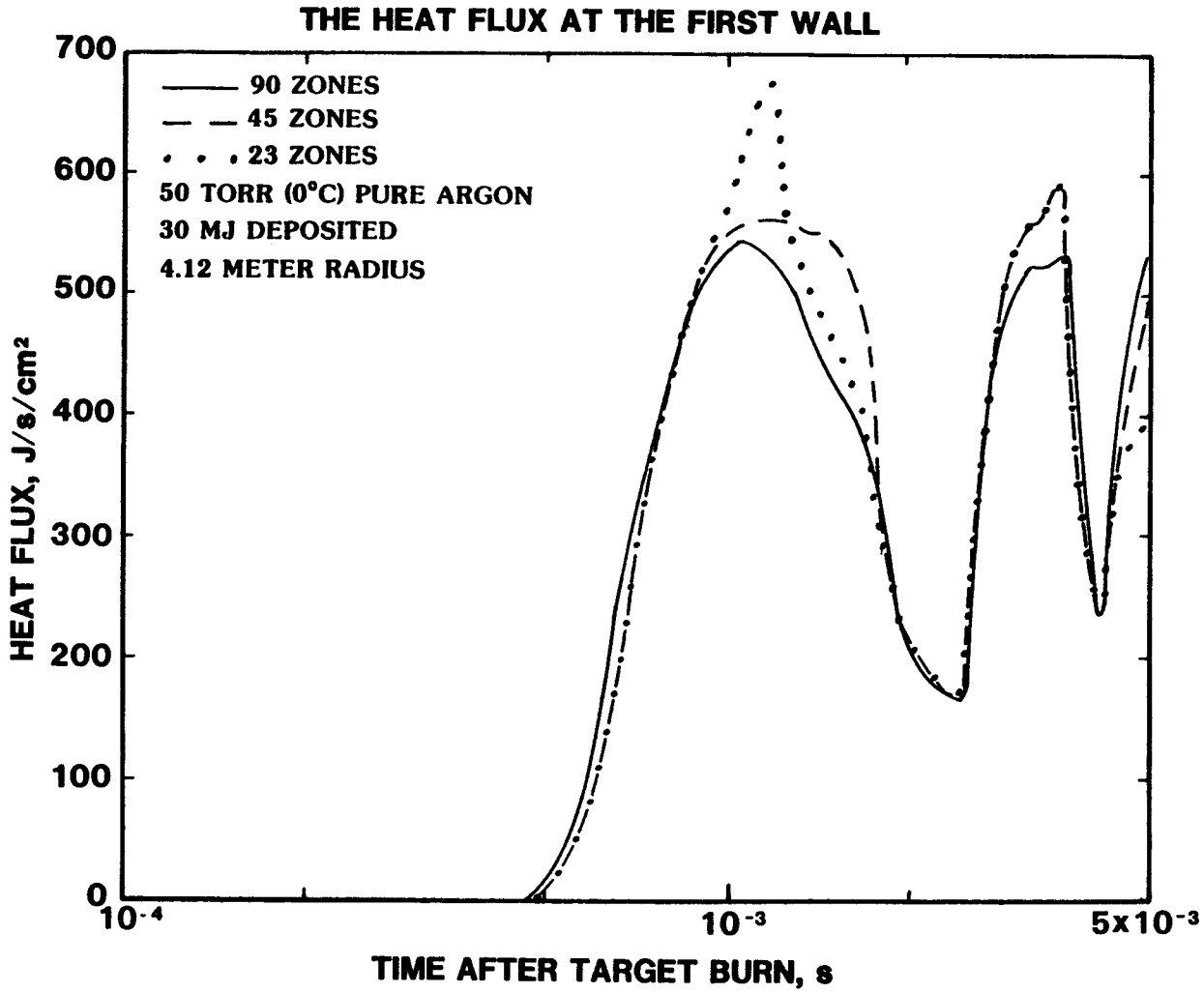

Fig. VI-13. The heat flux at the first wall as a function of time for the three Lagrangian meshes under study.

Table VI-5. Variations in the Peak Pressure Computed at the Wall with the Thickness of the Last Zone

$\frac{\text{Mass of last zone}}{\text{Mass of next to last zone}}$	Peak Pressure, J/cm^3
1/4	.344
1/2	.359
1	.355
2	.330

CHAPTER VII

SUMMARY AND CONCLUSIONS

A. Summary

The objective of this thesis has been twofold:

- to develop a better understanding of the phenomena that occur as an ICF cavity gas responds to a target explosion;
- improve the analytical and numerical models that are available for simulating the gas response.

In addressing these objectives, both the literature on the response of the atmosphere to a nuclear explosion as well as the analytical models that have been developed to describe the hydrodynamic motion of a shock wave were reviewed. These models are often not appropriate for describing the hydrodynamic response of an ICF cavity gas, either because the density of an ICF cavity gas is too low for the target explosion to be modeled as a point energy source, or because the deposited energy is not strongly coupled to hydrodynamic motion. In the case of a very low density gas, the hydrodynamic response is driven by the momentum of the debris. Conservation of energy and momentum were used in this thesis to develop a criterion for determining whether or not a debris driven shock wave will occur from a target explosion in a low density gas. Analytic models of the radiative and hydrodynamic response of a debris driven shock were also developed using global equations of mass, momentum, and energy conservation.

A detailed description of every point in the gas can be obtained by numerically solving the differential equations of radiation hydrodynamics. One of the unique aspects of the radiation transport model that is used in this thesis is that the spectral energy density is assumed to be given by a dilute Planckian function. Thus, the frequency spectrum is described by a radiation temperature, so the frequency variable can be integrated out of the radiation transport equations. This two temperature model of nonequilibrium radiation transport is applicable if either the opacity of the gas is frequency independent, or if the gas is comprised of only very opaque and very transparent regions. By ignoring hydrodynamic motion and implementing various other assumptions, the two temperature equations were used to analytically examine four stages of radiation transport that occur as a result of the temperature dependence of the opacity. While studying the diffusive stage, it was found that the tendency for a cooling wave to occur increases with an increase in the yield. For the first time, an analytic expression was derived that can be used to determine whether or not a cooling wave will be observed.

One of the goals of this work was to develop a model for computing the deposition of target x-rays in the gas that could be coupled to a radiation hydrodynamics code. After examining the magnitude of the secondary radiation emitted by the gas, it was determined that the point source model will usually be adequate for computing the x-ray deposition. The attenuation coefficient of the gas near the target was found to decrease significantly because of

ionization, so a model for computing the attenuation coefficient as a function of ionization was developed. The x-ray pulse is brief enough that the energy deposition can be assumed to be instantaneous for the radiation hydrodynamics calculation.

Another goal of this thesis was to develop a model for computing the interaction of target debris with the gas that could be used in a radiation hydrodynamics code. It was determined that the target ions would not follow straight line trajectories as they slow down because nuclear collisions are the dominant interactions. Hence, a time-dependent ion transport calculation is needed to rigorously compute the energy and momentum deposition rate. To avoid such complicated and costly calculations, an approximate approach was devised. The approximate approach uses the solution of a time-independent ion transport equation that describes the spatial profile as a function of energy for ions slowing down in a stationary medium. The solution is fit to analytic functions that are then used to estimate the average energy and momentum deposition rates as functions of time and space. By expressing the projected range in terms of atom layers traversed rather than distance, the analytic functions can be used to describe ions slowing down in a deforming medium, such as an ICF cavity gas.

In this thesis work the FIRE radiation hydrodynamics code has been modified to compute the radiation temperature in an improved way. Terms for computing the interactions of target x-rays and debris with the gas were also added to the equations solved by the code. These

modifications increase the ability of the code to realistically simulate the response of a cavity gas, especially if the gas density is low enough for nonequilibrium radiation transport to be important, or if the debris momentum affects the hydrodynamic motion.

B. Conclusions

B.1. The Results from Analytic Models

Using an analytic expression that was developed to determine whether a debris driven shock will form in a low density gas, it was found that if the debris spectrum consists of 1 gram of initially monoenergetic iron ions slowing down in argon at a density of 10^{15} atoms/cm^3:

- a debris driven shock will form if the initial kinetic energy of the debris is less than about 150 MJ;
- the debris will stream through the gas without forming a debris driven shock if the kinetic energy of the debris is greater than about 150 MJ.

These analytic predictions were verified using the version of the FIRE code that was developed as part of this thesis.

Using an analytic analysis of radiation transport at a thermal wave front, an expression was derived to determine the propagation speed of the thermal wave as a function of the deposited energy, gas density, and opacity. It was found that for an explosion in standard density air:

- a thermal diffusion wave will propagate outward if the yield is as small as a few hundred megajoules.

This analysis explains why a cooling wave is not observed in the FIRE code simulations of the cavity gas response.

B.2. The Results from FIRE Code Simulations

Four different parameter studies were conducted with the FIRE code. In each study it was assumed that 15% of the target yield was in the kinetic energy of one gram of iron target debris. The initial energy of the debris ions was assumed to be monoenergetic, and alpha particles and unburnt fuel were ignored. Another 15% of the yield was assumed to be in target x-rays. The spherical reactor cavity was assumed to be 4.12 meters in radius.

In the first parameter study, the gas response was studied as a function of gas density. Densities corresponding to 50, 5, 0.5, and 0.05 torr at standard temperature were considered. The equation of state and opacity data for argon mixed with 2% sodium was used, and a target yield of 100 MJ was used. It was found that:

- for densities less than 1.77×10^{18} atoms/cm^3 (50 torr at 0°C) the deposited energy becomes decoupled from hydrodynamic motion;
- for densities less than 1.77×10^{16} atoms/cm^3 (0.5 torr at 0°C), most of the hydrodynamic motion is induced by the momentum of the target debris.

The calculations from this parameter study were used to determine the minimum gas density required to protect a carbon or stainless steel first wall from evaporative erosion. It was found that for a power plant operating at 1000 MW thermal, a first wall about 4 meters from the target will be protected from evaporation if:

- more than about 10^{16} atoms/cm^3 (1/3 torr at 0°C) is used to protect a carbon first wall;
- more than about 3.5×10^{16} atoms/cm^3 (1 torr at 0°C) is used to protect a stainless steel first wall.

In the second parameter study the buffer gas response was studied for four different gases: pure argon, argon mixed with two volume percent sodium, pure xenon, and xenon mixed with five volume percent cesium. The gas density used in these examples corresponds to 50 torr at standard temperature, and a target yield of 100 MJ was assumed. It was found that:

- the deposited energy is more strongly coupled to hydrodynamic motion for the gas mixtures than for the pure gases;
- for the pure gases the radiation flux at the wall increases before the shock arrives, and then fluctuates as the emission rate of the gas within the cavity fluctuates;
- for the gas mixtures, the radiation flux at the wall increases as the kinetic energy of the shock is converted to internal energy during shock reflection, and is independent of the emission rate of gas away from the first wall.

In the third parameter study the gas response was studied for target yields ranging from 100 to 1000 MJ. The opacity and equation of state of argon mixed with two volume percent sodium was used, and the ambient gas density corresponds to 50 torr at standard temperature (0°C). The results showed that:

- the fraction of the deposited energy that goes into ionizing the gas and is thus decoupled from hydrodynamic motion increases as the deposited energy increases;
- the magnitude of the heat flux absorbed by the wall during shock reflection increases rapidly with an increase in the kinetic energy of the shock;
- the thermal wave will touch the first wall of a cavity 4.12 meters in radius when the deposited energy becomes greater than about 150 MJ.

The influence that the Lagrangian mesh has on the result of a calculation was examined in the final parameter study. The equation of state and opacity data of pure argon was used, and the gas density corresponds to 50 torr at standard temperature. A target yield of 100 MJ was assumed. It was found that:

- when the number of Lagrangian zones was increased from 23 to 90, the cost of the calculation increased by an order of magnitude, whereas the results changed by only a few percent;
- the pressure computed at the wall is not very sensitive to the thickness of the last zone, contrary to what has been observed with previous versions of the FIRE code.

C. Recommendations for Further Study

Although the development of the FIRE code was the primary purpose of this thesis, this work was only a part of a larger effort to analyze the thermal and mechanical response of an ICF first wall in a comprehensive, systematic fashion. The various codes that have

been part of the effort were shown in Figure VI-1, and have yet to be integrated into a unified package for determining the lifetime of an ICF cavity first wall.

In addition, there are still a few improvements that can be made to the FIRE code. Probably the most important of these is a better method of estimating the isotropy of the radiation flux. In some instances, a better estimate of the isotropy will decrease the flux by as much as a factor of four. Another area that was not addressed in this thesis was the reduction in the radiation flux absorbed by the wall that can be obtained when the surface reflectance is non-zero. This area is somewhat intractable because of the difficulty in predicting the surface finish. Finally, the results of the FIRE code should be compared to the results of a multifrequency code so that the applicability of the two temperature model of nonequilibrium radiation transport can be tested.

REFERENCES

1. G.A. Moses and R.R. Peterson, "FIRE - A Computer Code to Simulate the Cavity Gas Response to Inertial Confinement Target Explosions," University of Wisconsin Fusion Engineering Program Report UWFDM-336 (January 1980).

2. M.K. Matzen and R.L. Morse, "Structure and Observable Characteristics of Laser Driven Ablation," Physics of Fluids 22, (April 1979).

3. G.S. Fraley, "Implosion Characteristics of Deuterium-Tritium Pellets Surrounded by High Density Shells," Los Alamos National Lab., LA-6378-MS, September 1976.

4. J.A. Blink, P.E. Walker, and H.W. Meldner, "Energy Partition and Neutron Spectra from Laser Fusion Reactor Targets," Transactions of the ANS Winter Meeting 70, San Francisco (1977).

5. D.B. Henderson, "Pulse Unfocusing Within Laser Fusion Reactors," Nuclear Engineering and Design 30, (1974).

6. B. Badger et al., "HIBALL - A Heavy Ion Beam Fusion Reactor Design Study," University of Wisconsin Fusion Engineering Program Report UWFDM-450 (September 1981).

7. J. Hovingh, "Materials Considerations for Inertially Confined Fusion Reactors," Lawrence Livermore Lab., UCRL-81208, June 1978.

8. T.G. Frank, I.O. Bohachevsky, and L.A. Booth, "Heat Transfer Problems Associated with Laser Fusion," AIChE Symposium 73(168).

9. T.O Hunter and G.L. Kulcinski, "Surface Damage and Thermal Effects from Transient Thermonuclear Radiation in Inertial Confinement Fusion Reactors," University of Wisconsin Fusion Engineering Program Report UWFDM-233 (April 1978).

10. T.J. McCarville, A.M. Hassanein, and G.L. Kulcinski, "The Response of Stainless Steel to Pellet Debris in a Laser Fusion Reactor," University of Wisconsin Fusion Engineering Program Report UWFDM-282 (November 1978).

11. T.O. Hunter and G.L. Kulcinski, "A Computer Code for Transient Radiation Damage Analysis," University of Wisconsin Fusion Engineering Program Report UWFDM-247 (April 1978).

12. A.M. Hassanein and G.L. Kulcinski, "Numerical Methods for Calculating the Temperature Increase in ICF First Walls," University of Wisconsin Fusion Engineering Program Report UWFDM-397 (Nov. 1980).

13. A.M. Hassanein and G.L. Kulcinski, "A*THERMAL Computer Code Description," University of Wisconsin Fusion Engineering Program Report UWFDM-461 (December 1981).

14. R. Behrisch, "First Wall Erosion in Fusion Reactors, Nucl. Fusion 12, (1972).

15. M. Born and E. Wolf, Principles of Optics, Pergamon Press, 5th Ed., 1975.

16. L.E. Levine, "Two-Dimensional, Unsteady, Self-Similar Flows in Gas Dynamics," ZAMM 52 (1972).

17. J.A. Dalessandro, "First Wall Thermal Stress Analysis for Suddenly Applied Heat Fluxes," Proc. 3rd ANS Topical Mtg. on The Tech. of Controlled Nuclear Fusion, GA-A14931, (1978).

18. B. Badger et al., "SOLASE-H: A Laser Fusion Hybrid Study," University of Wisconsin Fusion Engineering Program Report UWFDM-270 (May 1979).

19. T.O. Hunter and G.L. Kulcinski, "Transient Energy Deposition, Temperatures, and Displacement Rates," University of Wisconsin Fusion Engineering Program Report UWFDM-217 (Oct. 1977).

20. S.G. Varnado and G.A. Carlson, "Considerations in the Design of Electron Beam Induced Fusion Reactor Systems," Nucl. Tech. 29, (June 1976).

21. J. Hovingh, "Ion-Beam Reactor First Wall Design," Appendix 1.3, ERDA Summer Study of Heavy Ions for Inertial Fusion, USERDA Report LBL-5543, Dec. 1976.

22. S. Chow and I.O. Bohachevsky, "MHD Deceleration of Fusion Reaction Products," Los Alamos National Laboratory, LA-7778-MS, April 1979.

23. J.J. Devaney, "Magnetically Protected First Wall for a Laser Induced Thermonuclear Reactor," Los Alamos National Laboratory, LA-5699-MS, 1974.

24. M.J. Lubin and R.A. Axeford, "Fusion by Laser," Scientific American 224, (June 1971).

25. A.P. Fraas et al., "Analytical and Experimental Investigation of the Blascon Energy Conversion System for Laser Fusion Reactors," ASME 72-WA/Ener-1, presented at the ASME Meeting, New York, Nov. 1972.

26. J.K. Baird and V.V. Anderson, "Combination First Wall and Parabolic Lithium Mirror for a Laser-Driven Pellet Fusion Reactor," 6th Symposium on Engineering Problems of Fusion Reactors, 75CH-1097-NPS, 1975.

27. L.A. Booth, "Central Station Power Generation by Laser Driven Fusion," Los Alamos National Lab., LA-4858-MS, Feb. 1972.

28. "Laser Fusion Power Reactor Systems," Westinghouse Electric Corp., WFPS-TME-070, December 1977.

29. J. Hovingh et al., "The Preliminary Design of a Suppressed Ablation Laser-Induced Fusion Reactor," ANS 1st Topical meeting of Controlled Nuclear Fusion, San Diego, 1974.

30. J. Maniscalco et al., "Civilian Application of Laser Fusion," Lawrence Livermore Lab., UCRL-52349, 1977.

31. Laser Program Annual Report, Lawrence Livermore Lab., UCRL-50021-78, Vol. 3, 1978.

32. ERDA Summer Study of Heavy Ion Inertial Fusion, Final Report, LBL-5543, Lawrence-Berkeley Laboratories, December 1976, p. 93.

33. Particle-Beam Fusion Progress Report, July 1980 through December 1981, SAND81-0683, Sandia Laboratory, Albuquerque, NM, October 1981.

34. R.W. Conn et al., "SOLASE: A Conceptual Laser Fusion Reactor Design," University of Wisconsin Fusion Engineering Program Report UWFDM-220 (December 1977).

35. R.R. Peterson and G.A. Moses, "MIXER - A Multi-Species Optical Data and Equation of State Computer Code," University of Wisconsin Fusion Engineering Program Report UWFDM-372 (Sept. 1980).

36. S. Glasstone, ed., "Effects of Nuclear Weapons," Department of Defense and Atomic Energy Commission, U.S. Government Printing Office, 1962.

37. H.A. Bethe et al., "Blast Wave," Los Alamos National Laboratory, LA-2000, March 1958.

38. H.A. Bethe, "Theory of the Fireball," Los Alamos National Laboratory, LA-3064, June 1964.

39. Ia. B. Zel'dovich, A.S. Kompaneets, Iu. P. Raizer, "Radiation Cooling of Air; I. General Description of the Phenomenon and the Weak Cooling Wave," Soviet Physics JETP 34(5), (Nov. 1978).

40. Ia. B. Zel'dovich, A.S. Kompaneets, Iu. P. Raizer, "Cooling of Air by Radiation; II. Strong Cooling Wave," Soviet Physics JETP 34(6), (Dec. 1958).

41. Iu. P. Raizer, "Glow of Air During a Strong Explosion, and the Minimum Brightness of a Fireball," Soviet Physics JETP 34(2), (August 1958).

42. G. Taylor, "The Formation of a Blast Wave by a Very Intense Explosion; I. Theoretical Discussion," Proc. R. Soc. A201(159), (March 1950).

43. A. Sakurai, "On the Propagation and Structure of the Blast Wave I," J. Phys. Japan 8(662), (1953).

44. D.L. Jones, "The Energy Parameter B for Strong Blast Waves," NBS Technical Note 155, NBS Boulder Laboratories, July 1962.

45. L.I. Sedov, Similarity and Dimensional Methods in Mechanics, (English translation), Academic Press, 1959.

46. G.G. Chernyi, "The Problem of a Point Explosion," MOA TIL/T.4871, Ministry of Aviation, Great Britian, 1959.

47. D.A. Freiwald and R.A. Axeford, "Approximate Spherical Blast Theory Including Source Mass," Journal of Applied Physics 46(3), (March 1975).

48. D.L. Jones, "Intermediate Strength Blast Wave," Physics of Fluids 11(8), (Aug. 1968).

49. Y.B. Zel'dovich and Y.P. Raizer, Physics of Shock Waves and High Temperature Hydrodynamic Phenomena, ed. W.D. Hayes and P.F. Probstein, Academic Press, 1967.

50. G.C. Pomraning, The Equations of Radiation Hydrodynamics, Pergamon Press, 1973.

51. A. Eddington, The Internal Constitution of the Stars, Cambridge University Press, 1926.

52. G.C. Pomraning, "An Extension of the Eddington Approximation," J. Quant. Spectrosc. Radiat. Transfer 9, (1968).

53. G.N. Minerbo, "Maximum Entropy Eddington Factors," J. Quant. Spectrosc. Radiat. Transfer 20, (1977).

54. R.F. Probstein, "Radiation Slip," AIAA Journal, Technical Notes and Comments 1(5), (1963).

55. R.G. Deissler, "Diffusion Approximation for Thermal Radiation in Gases with Jump Boundary Condition," Transactions of the ASME, May 1964.

56. D.S. Kershaw, "Flux Limiting Nature's Own Way - A New Method for Numerical Solution of the Transport Equation," Lawrence Livermore Lab., UCRL-78378, July 1976.

57. S.L. Thompson and H.S. Lawson, "Improvements in the CHART-D Radiation Hydrodynamics Code II, A Revised Program," Sandia Lab., SC-RR-710713, June 1970.

58. G.I. Barenblatt, "On Some Unsteady Motions of a Liquid and a Gas in a Porous Medium," Prikl. Mat. i Mekh. 16, (1952).

59. R.R. Peterson and G.A. Moses, "Blast Wave Calculations in Argon Cavity Gas for Light Ion Beam Fusion Reactors," University of Wisconsin Fusion Engineering Program Report UWFDM-315 (Oct. 1979).

60. D. Halliday and R. Resnick, Physics, 2nd Edition, John Wiley & Sons, 1966.

61. J. von Neumann and R.D. Richtmyer, "A Method for the Numerical Calculation of Hydrodynamic Shocks," Journal of Appl. Phys. 21, (March 1950).

62. R.E. Kidder and W.S. Barnes, "WAZER, A One-Dimensional, Two Temperature Hydrodynamic Code," Lawrence Radiation Laboratory, UCRL-50583, Livermore, CA, January 31, 1969.

63. L. Spitzer, Physics of Fully Ionized Gases, Second Edition, Interscience Publishers, New York, 1962.

64. R.J. Cole, Jr., "A Program for Rapid Calculation of X-Ray Deposition," SC-RR-69-855, Sandia Lab., Albuquerque, NM, July 1970.

65. G.A. Moses, R.R. Peterson, M. Sawan, and W. Vogelsang, "High Gain Target Spectra and Energy Partitioning for Ion Beam Fusion Reactor Design Studies," University of Wisconsin Fusion Engineering Program Report UWFDM-396 (1980).

66. T.O. Hunter and G.L. Kulcinski, "Description of the Response of Materials to Pulsed Thermonuclear Radiation, Part III," University of Wisconsin Fusion Engineering Program Report UWFDM-232 (April 1978).

67. E.H.S. Burhop, The Auger Effect and Other Radiationless Transitions, Cambridge, University Press, 1952.

68. P. Sigmund, "Energy Loss of Charged Particles in Solids," Proc. of NATO Advanced Study Institute on Radiation Damage Processes in Materials, Corsica, France, 1973.

69. N. Bohr, "The Penetration of Atomic Particles Through Matter," Mat. Fys. Medd. Dan. Vid. Selsk. 16(8), (1948).

70. J. Lindhard, "Thomas-Fermi Approach and Similarity in Atomic Collisions," NAS-NRC Publ. 1133, 1, (1964).

71. M.M.R. Williams, "The Role of the Boltzmann Transport Equation in Radiation Damage Calculations," Progress in Nuclear Energy 3, (1978).

72. J.B. Sanders, "On the Application of Boltzmann Transport Equations to Ion Bombardment of Solids," 5th International Conference on Atomic Collisions in Solids, Gatlinburg, TN, 1973.

73. J. Lindhard, M. Scharff, H.E. Schiott, "Range Concepts on Heavy Ion Ranges," Mat. Fys. Medd. Dan. Vid. Selsk. 33(14), (1963).

74. P. Mazur, J.B. Sanders, "On the Derivation of the Range Equation for Energetic Particles in Amorphous Materials," Physica 44, (1969).

75. D.K. Brice, "Spatial Distribution of Ions Incident on a Solid Target as a Function of Instantaneous Energy," Radiation Effects 11, (1971).

76. D.K. Brice, "Ion Implantation Range and Energy Deposition Codes COREL, RASE4, DAMG2," Sandia Lab., SAND-75-0622, Albuquerque, NM, 1977.

77. O.S. Oen, M.T. Robinson, "Slowing-Down Time of Energetic Ions in Solids," Jour. of Appl. Phys. 46(12), (1975).

78. J. Lindhard, V. Nielsen, M. Scharff, "Approximation Method in Classical Scattering by Screened Coulomb Fields," Mat. Fys. Medd. Dan. Vid. Selsk. 36(10), (1968).

79. M. Abramouritz and I.A. Stegon, eds., Handbook of Mathematical Functions, U.S. Dept. of Commerce, AMS 55, June 1964.

80. T.J. McCarville, R.R. Peterson, G.A. Moses, "Improvements in the FIRE Code for Simulating the Response of a Cavity Gas to ICF Target Explosions," University of Wisconsin Fusion Engineering Program Report UWFDM-407 (1981).

81. D. Mosher, "The Coronal Equilibrium of High Atomic Number Plasmas," Naval Research Laboratory Memorandum Report 2563, (March 1973).

82. F. Biggs and R. Lighthill, "Analytical Approximations for X-Ray Cross Sections II," Sandia Lab., SC-PR-71-0507, Albuquerque, NM, (Dec. 1971).

83. F. Biggs and R. Lighthill, "Analytical Approximations for Total and Energy Absorption Cross Sections for Photon-Atom Scattering," Sandia Lab., SC-PR-72-0685, Albuquerque, NM, Dec. 1972.

84. K.G. Adams and F. Biggs, "Efficient Computer Access to Sandia Photon Cross Sections," Sandia Lab., SC-RR-72-0683, Albuquerque, NM, (Dec. 1973).

85. G. Yonas, "Fusion Power with Particle Beams," Scientific American, (Nov. 1978) 239.

86. R.R. Peterson, G.W. Cooper, and G.A. Moses, "Cavity Gas Analysis for Light Ion-Beam Fusion Reactors," Nuclear Tech./Fusion 1, (July 1981).

87. A.M. Hassanein, T.J. McCarville, and G.L. Kulcinski, "First Wall Evaporation in Inertial Confinement Fusion Reactors Utilizing Gas Protection," presented at the Second Topical Meeting on Fusion Reactor Materials, Seattle, (August 1981).

88. T.J. McCarville, G.L. Kulcinski, and G.A. Moses, "An Analytical Model for the Motion and Radiative Response of a Low Density Inertial Confinement Fusion Buffer Gas," University of Wisconsin Fusion Engineering Program Report UWFDM-405 (Jan. 1981).

89. T.J. McCarville, G.A. Moses, and G.L. Kucinski, "A Model for Depositing Inertial Confinement Fusion X-Rays and Pellet Debris into a Cavity Gas," University of Wisconsin Fusion Engineering Program Report UWFDM-406 (April 1981).

90. L.D. Landau and E.M. Lifshitz, Fluid Mechanics, Pergamon Press, Oxford, 1959, p. 365.

APPENDIX A

THE PRESSURE EXERTED BY A REFLECTED SHOCK WAVE

In the text by Zel´dovich and Raizer,[49] the Hugoniot relations for a reflecting shock (see the notation in Chapter III, Section B of this thesis) are shown to be:

$$\frac{\rho_o}{\rho_1} = \frac{(\gamma + 1)P_o + (\gamma - 1)P_1}{(\gamma - 1)P_o + \gamma + 1)P_1}, \tag{A1}$$

$$\frac{\rho_1}{\rho_w} = \frac{(\gamma + 1)P_1 + (\gamma - 1)P_w}{(\gamma - 1)P_1 + (\gamma + 1)P_w}, \tag{A2}$$

and $$(P_1 - P_o)(\frac{1}{\rho_o} - \frac{1}{\rho_1}) = (P_w - P_1)(\frac{1}{\rho_1} - \frac{1}{\rho_w}). \tag{A3}$$

The above equations can be combined to eliminate the densities, leaving

$$(P_w - P_1)^2[(\gamma + 1)P_o + (\gamma - 1)P_1] =$$

$$(P_1 - P_o)^2[(\gamma + 1)P_w + (\gamma - 1)P_1]. \tag{A4}$$

After some straightforward algebraic manipulations, Equation (A4) can be written as:

$$P_w^2 - P_w \frac{(3\gamma - 1)P_1^2 + (\gamma + 1)P_o^2}{(\gamma - 1)P_1 + (\gamma + 1)P_o}$$

$$- P_oP_1 \frac{(3\gamma - 1)P_1 - (\gamma - 1)P_o}{(\gamma - 1)P_1 + (\gamma + 1)P_o} = 0. \tag{A5}$$

Equation (A5) is a quadratic equation for the pressure of a shock wave

reflecting from a wall. To show that Equation (15) is indeed a root, Equation (A5) can be factored by writing it as:

$$P_w^2 - P_w\left[\frac{(\gamma - 1)P_1P_o + (\gamma + 1)P_o^2 + (3\gamma - 1)P_1^2 - (\gamma - 1)P_oP_1}{(\gamma - 1)P_1 + (\gamma + 1)P_o}\right]$$

$$- P_oP_1\,\frac{(3\gamma - 1)P_1 - (\gamma - 1)P_o}{(\gamma - 1)P_1 + (\gamma + 1)P_o} = 0, \tag{A6}$$

and then

$$P_w^2 - P_w\left[P_o + P_1\,\frac{(3\gamma - 1)P_1 - (\gamma - 1)P_o}{(\gamma - 1)P_1 + (\gamma + 1)P_o}\right]$$

$$P_oP_1\,\frac{(3\gamma - 1)P_1 - (\gamma - 1)P_o}{(\gamma - 1)P_1 + (\gamma + 1)P_o} = 0. \tag{A7}$$

Equation (A7) is easily factored into

$$(P_w - P_o)\left[P_w - P_1\,\frac{(3\gamma - 1)P_1 - (\gamma - 1)P_o}{(\gamma - 1)P_1 + (\gamma + 1)P_o}\right] = 0. \tag{A8}$$

The root $P_w = P_o$ is the trivial case for no shock. The other root shows that Equation (15) is the correct expression for the pressure from a reflecting shock.